Model-Based Analysis of Aging-Induced Emission Progression of Gas Turbines
-
Modellbasierte Analyse alterungsinduzierter Emissionsprogression von Gasturbinen

Von der Fakultät für Maschinenwesen der Rheinisch-Westfälischen Technischen Hochschule Aachen zur Erlangung des akademischen Grades eines Doktors der Ingenieurwissenschaften genehmigte Dissertation

vorgelegt von
Moritz Lipperheide

Berichter: Prof. Dr.-Ing. habil. Manfred Christian Wirsum
Prof. Dr.-Ing. Christian Oliver Paschereit

Tag der mündlichen Prüfung: 11. September 2019

Abstract

State-of-the-art gas turbine technology is technically capable of providing the flexible power generation as required in today's electricity markets. Still, the economic and ecological pressure on gas turbine power generation demands cost reductions while maintaining the technical standard. Digitalization has a high potential for cost-effective optimization of gas turbine operation, using the existing large amount of available data for an Asset Performance Management approach.
Aiming towards the objective of a digitally-supported 'Gas Turbine 4.0', this research presents a model-based approach to utilize legally required Nitrogen Oxide (NOx) and Carbon Monoxide (CO) emission measurements as a precious source of information on combustion performance. Semi-empirical emission models were derived from kinetics and then adapted to the investigated three engines from the GT24/GT26 fleet. The developed gas turbine model covers component aging for the combustor and turbine outlet temperature measurements. By the combined use of the emission data and models, engine and aging models, observed emission progression in long-term operation could be linked to aging mechanisms. Artificial Neural Networks as a prominent representative of artificial intelligence were used as a benchmark for the modeling approach.
Beside the model's very-own monitoring purpose, the method also offers a number of application possibilities for Asset Performance Management, such as Virtual Commissioning or an adaption of the maintenance strategy. Extending the findings to a large part of the GT24/GT26 fleet further allowed relating operation regime and the observed aging progress.

Kurzfassung

Die moderne Gasturbinentechnologie ist technisch in der Lage, die komplexen Aufgaben eines hochflexiblen Betriebs zur Kompensation der Residuallasten, die durch die fluktuierende Einspeisung erneuerbarer Energien entstehen, zu meistern. Dennoch sieht sie sich in der gegenwärtigen Strommarktsituation einem starken ökonomischen und ökologischen Druck ausgesetzt, der Einsparungen im Betrieb bei gleichzeitiger Sicherung der Leistungsfähigkeit fordert. Ein hohes Potenzial für kostengünstige Verbesserungen bietet die Digitalisierung des Gasturbinenbetriebs auf Basis der ohnehin umfangreich verfügbaren Betriebsdaten in einem Asset Performance Management Ansatz.
Auf dem Weg zur Vision einer digital unterstützten 'Gasturbine 4.0' präsentiert diese Arbeit einen modellbasierten Ansatz zur Verwendung der gesetzlich vorgeschriebenen

Stickoxid (NOx) und Kohlenmonoxid (CO) Messungen als wertvolle Informationsquelle über die Verbrennungcharakteristik. Semi-empirische Emissionsmodelle wurden aus der Kinetik der Schadstoffbildung hergeleitet und anschließend auf den Anwendungsfall der GT24/GT26 Gasturbine adaptiert. Mittels eines entwickelten Gasturbinenmodells, das Komponentenalterung der Brennkammer und der Turbinenaustrittstemperaturmessung umfasst, konnten die beobachtete Emissionsprogression im Langzeitbetrieb mit den entsprechenden Alterungsphänomenen in Zusammenhang gebracht werden. Künstliche neuronale Netze als ein prominenter Vertreter der künstlichen Intelligenz wurden als Vergleichsmaßstab herangezogen.
Neben dem modelleigenen Zweck der Betriebsüberwachung, bietet die Methode mehrere Anwendungsmöglichkeiten im Asset Performance Management, wie zum Beispiel virtuelle Inbetriebnahme oder eine Anpassung der Instandhaltungsstrategie. Die Erweiterung der gefundenen Erkenntnisse auf die gesamt verfügbare GT24/GT26 Flotte erlaubte weiterhin, den Alterungsfortschritt mit der Fahrweise in Relation zu setzen.

Key words

NOx emissions, CO emissions, combustion modeling, process analysis, gas turbine, sequential combustion, asset performance management, gas turbine aging, sensor drift

Danksagung

Die vorliegende Arbeit wurde während meiner Zeit am Lehrstuhl und Institut für Kraftwerkstechnik, Dampf- und Gasturbinen der RWTH Aachen verfasst. Ich möchte dem Institutsleiter, Herrn Prof. Dr.-Ing. habil. Manfred Wirsum, für die Betreuung meiner Arbeit und seine Unterstützung bei ihrer Durchführung danken. Ein Dank gilt ebenfalls Prof. Dr.-Ing. Christian Oliver Paschereit für die Übernahme des Koreferats und Univ.-Prof. Dr.-Ing. Reinhold Kneer für die Übernahme des Vorsitzes der Prüfungskommission.
Die in der Dissertation vorgestellten Untersuchungen wurden in Kooperation mit GE Power im Rahmen des Verbundvorhabens Cooreflex-turbo der AG Turbo durchgeführt und mit Mitteln des Bundesministeriums für Wirtschaft und Energie (BMWi) aufgrund eines Beschlusses des Deutschen Bundestages unter dem Förderkennzeichen 03ET7040H gefördert. Für die finanzielle und für die darüberhinausgehende ideelle Unterstützung der AG Turbo durch die Mitglieder im Arbeitskreis 'Verbrennung' und den Industriepartner GE Power möchte ich mich an dieser Stelle herzlich bedanken. In besonderer Weise bin ich bei GE Power Dr. Martin Gassner, Dr.-Ing. Stefano Bernero und Dr. Jochen Schabacker zu Dank verpflichtet, die mir durch ihre aušordentliche Unterstützung sehr viel mehr als nur die Vertreter eines Industriepartners auf dem Weg zu dieser Dissertation waren.
Ich möchte mich auch ganz herzlich bei Katharina Bleich und Maria Magee für das Lektorat, bei Dr. Cornelia und Ulrich Lipperheide für einen wissenschaftlich-fachfremden Blick auf das Thema und bei Thomas Bexten, Dr.-Ing. Daniel Kroniger und Dr.-Ing. Martin Habermehl für die fachmännische Unterstützung, Anregung und wissenschaftlichen Austausch während der Promotion bedanken.

Contents

List of Figures

Nomenclature

Latin letters

A_{com}	Cross-sectional area of SEV combustor
ANN	Artificial Neural Network
APM	Asset Performance Management
$b_{[\ ]}$	CO correlation parameter
$c_{\_}$	Concentration
C_{2+}	Long-chain hydrocarbons
$CEMS$	Continous Emission Monitoring System
$c_{\_}NOx$	NOx concentration
d	Number of hot/cold spots
ΔCO	Difference between peak and equilibrium value
Δp	Pressure drop across EV combustor
ΔT	Temperature difference between turbine outlets
e	ANN error
E_{a}	Activation energy
EV	EnVironmental burner
f	Component mappings
g	Index of cold/hot/average burner groups
H	(Relative) humidity
h	Specific enthalpy
HPT	High pressure turbine
i	Index of thermocouple
in	ANN input
k	Reaction rate constant
LPT	Low pressure turbine

$\dot{m}$ ..... Mass flow rate
n ..... Number of data points
net ..... ANN net input
OPC ..... OPerational Concept
out ..... ANN output
p ..... Pressure
$SEVon/off$ ..... SEV operation switched on/off
SEV ..... Sequential EnVironmental burner
T ..... Temperature
t ..... Operation time
u, p, s, v ..... ANN layers
$\dot{V}$ ..... Volumetric flow rate
v ..... Velocity
$VIGV$ ..... Variable Inlet Guide Vane
w ..... ANN weights
x ..... Mole fraction
X_{CO} ..... Aging parameter for cold streaks
X_{NOx} ..... Aging split parameter
z_{com} ..... Characteristic length of combustor

Greek letters

α ..... Pressure exponent EV
β ..... Exponential factor EV
ϵ ..... Measurement uncertainty
η ..... ANN learning rate
γ ..... Pressure exponent SEV
κ ..... Model parameter ignition delay
λ ..... Air-to-fuel equivalence ratio
ν ..... Polytropic efficiency
o ..... ANN target
ϕ ..... On/off parameter for SEV
π ..... Pressure ratio

ψ ..... Model parameter oxidation time
ρ ..... Density
σ ..... Standard deviation
τ ..... Characteristic combustion time
Θ ..... ANN thresholds
θ ..... Kinetic model parameter
υ ..... Model parameter ignition delay
χ ..... Model parameter oxidation time
ξ ..... Model parameter ignition delay
ζ ..... Discharge coefficient

Indices

$[\,]_{0}$ ..... Initial state
$[\,]_{\mathrm{amb}}$ ..... Ambient
$[\,]_{\mathrm{com}}$ ..... Commissioning
$[\,]_{\mathrm{comp}}$ ..... Compressor
$[\,]_{\mathrm{corr}}$ ..... Corrected
$[\,]_{\mathrm{cox}}$ ..... Complete oxidation
$[\,]_{\mathrm{e}}$ ..... Emission
$[\,]_{\mathrm{equil}}$ ..... Equilibrium
$[\,]_{\mathrm{fix}}$ ..... Fixed
$[\,]_{\mathrm{hg}}$ ..... Hot gas
$[\,]_{\mathrm{HPT}}$ ..... High Pressure Turbine
$[\,]_{\mathrm{ign}}$ ..... Ignition (delay)
$[\,]_{\mathrm{in}}$ ..... Inlet
$[\,]_{\mathrm{LPT}}$ ..... Low Pressure Turbine
$[\,]_{\mathrm{m}}$ ..... Measured
$[\,]_{\mathrm{p}}$ ..... Predicted
$[\,]_{\mathrm{pf}}$ ..... Postflame
$[\,]_{\mathrm{post}}$ ..... Downstream of flame zone
$[\,]_{\mathrm{pre}}$ ..... Upstream of flame zone
$[\,]_{\mathrm{predict}}$ ..... Predicted

$[\,]_{\text{red}}$ ..... Reduced
$[\,]_{\text{ref}}$ ..... Reference
$[\,]_{\text{res}}$ ..... Residence
$[\,]_{\text{sat}}$ ..... Saturation

1. Introduction

The world's electricity demand (Fig. 1.1) is expected to increase in the next decades as a consequence of the desire for a higher standard of living [1].

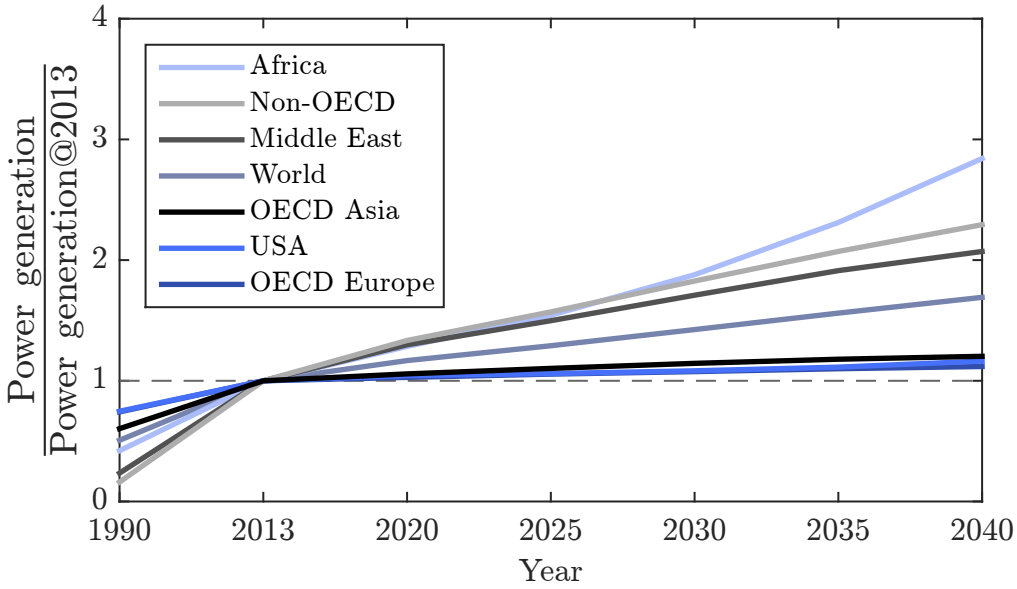

Figure 1.1.: Power generation per year for different world regions. Data and definitions taken from World Energy Outlook 2015 [1] for the 'new policies scenario'.

While developing countries try to establish a reliable electricity supply, electricity is going to substitute other forms of energy in developed countries due to emission regulations (transport) or convenience (residential use). Even though a reduction of energy use by an improved efficiency may help to lower the overall energy consumption in the 'first world', rebound effects, such as a more extensive use, often compensate the energy savings. Likewise, renewable power generation is not expected to entirely provide electricity with the expected reliability and 24/7 availability. Thus, new fossil fuel based power plants, whose majority will be natural gas fired, are predicted to be built worldwide, showing a remarkable net growth (Fig. 1.2)[1]. Among the natural gas-fired energy conversion technologies, gas turbines are expected to provide a large

part of the net growth as they offer the possibility to meet tomorrow's energy demand at different scales and operation scenarios.

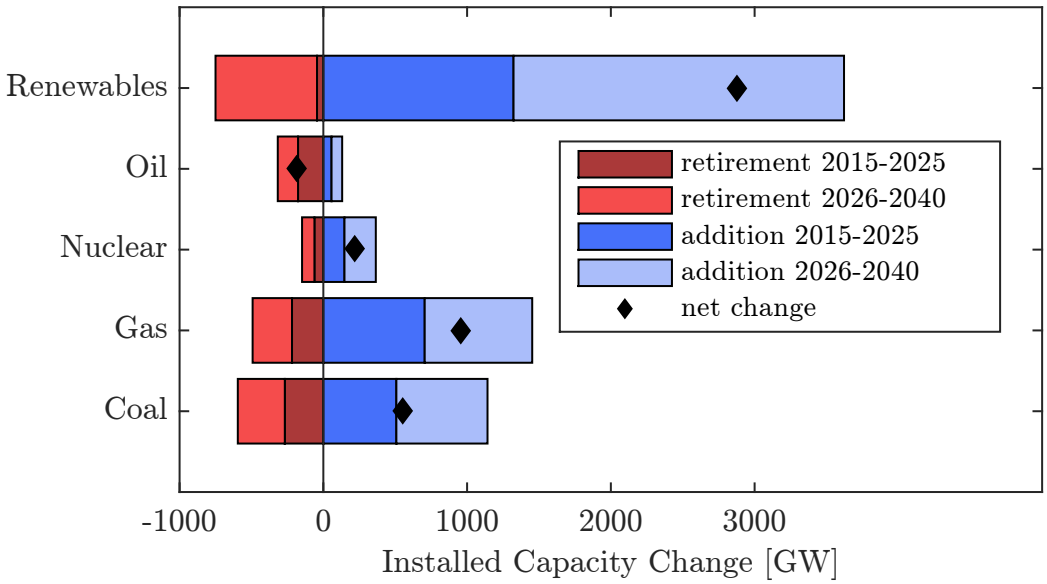

Figure 1.2.: Addition and retirements of power plant capacity by fuel. Data and definitions taken from World Energy Outlook 2015 [1] for the new policies scenario.

1.1. Gas Turbine Operation for Power Generation

After a technical introduction to gas turbine thermodynamics, requirements on gas turbines for different global electricity markets are outlined.

1.1.1. Gas Turbine

The gas turbine (see Fig. 1.3) is an internal combustion engine which generates mechanical power or thrust (when used for aircrafts) by the conversion of fuel-bound chemical energy in a continuous combustion process. Generally, the gas turbine process includes three steps: compression, combustion and expansion. During combustion, the energy of the fuel in either a gaseous ('(natural) gas') or liquid state ('oil') heats a previously compressed working fluid (the 'gas'), which flows through the machine. Exiting the combustor, the gas then releases its energy to a turning rotor by an expansion process in the turbine. Part of the mechanical energy of the rotor is used to drive the previous necessary compression process. The remaining surplus power in the fluid can then further be expanded in order to transfer more energy to the rotor for a mechanical drive or

for power generation. Alternatively, the excess energy in the fluid can be used to accelerate the gas in a nozzle to generate thrust for aircraft engines. As the gas temperature at turbine inlet usually exceeds the allowable material temperature of the gas turbine parts, those components are actively cooled by secondary air, which bypasses the combustor to provide high pressure flow at comparably cool compressor outlet conditions.

Gas turbines operate continuously, in contrast to positive displacement engines: Turbomachines add or extract energy between the working fluid in an open volume by transferring kinetic energy to or from the fluid during pressurizing (compression) or depressurizing (expansion). In contrast, displacement engines, i.e. piston engines, need to change the actual size of a closed volume for compression or expansion processes. The continuous mode of operation results in a compact design of a gas turbine even for high power outputs and thus high power densities compared to other thermal engines.

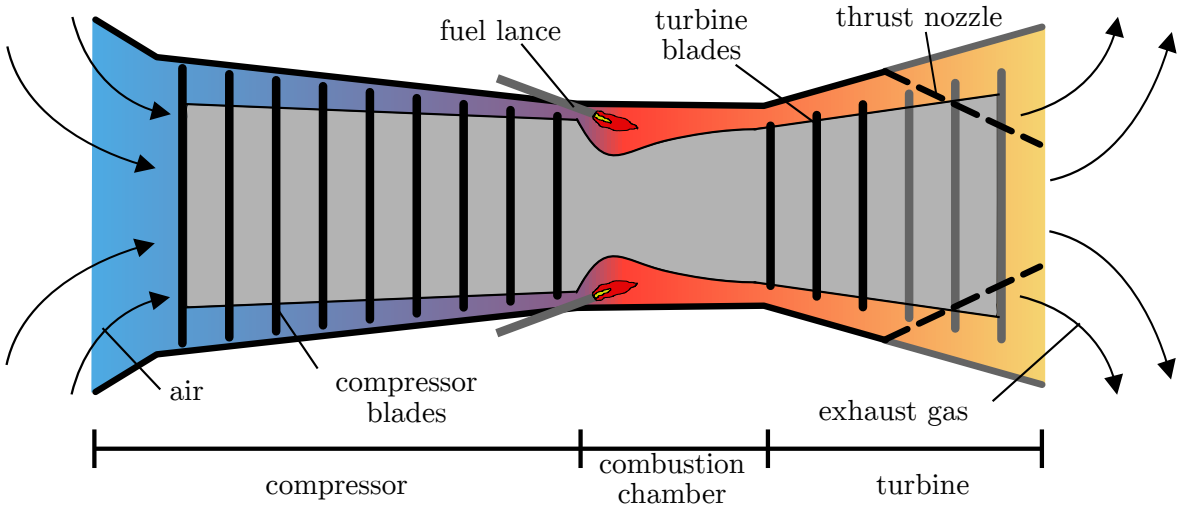

Figure 1.3.: Gas turbine scheme

The above described gas turbine process corresponds to a thermodynamic cycle (Fig. 1.4a), whose ideal reference is the 'Brayton Cycle'. In the case of the actual gas turbine process, the gas is compressed polytropically from state 1, the compressor inlet, to state 2, which is the compressor outlet/combustor inlet. During compression, energy has to be transferred to the fluid by the rotation of the rotor. At the same time, the temperature rises with pressure by the characteristics of the working fluid 'gas'. Heat is then added at constant pressure in the combustor, so that the highest temperature is reached at state 3, the combustor outlet/turbine inlet. The fluid is polytropically expanded in the turbine from state 3 to state 4 and thereby transfers its enthalpy ($\equiv$ Temperature for (ideal) gas) to mechanical work. Since more power can be taken out

during expansion than has to be added during compression, denoted by the vertical distance between state 1-2 and state 3-4, the net power of the gas turbine is positive.

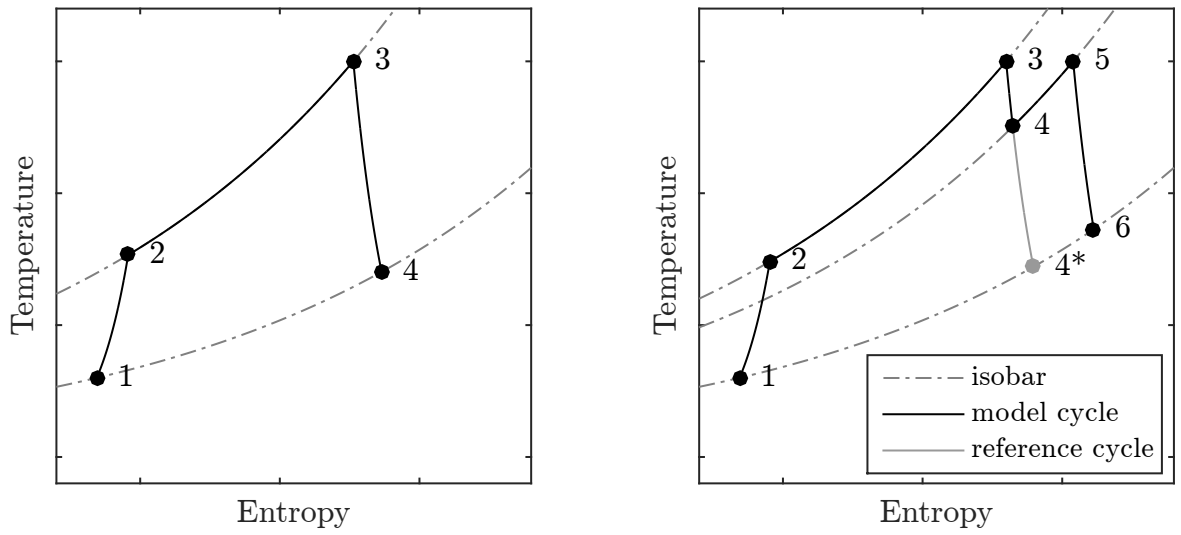

(a) Open gas turbine cycle **(b)** Open gas turbine cycle with reheat

Figure 1.4.: Real gas turbine process as a thermodynamic cycle with losses in expansion and compression

From a thermodynamic point of view, this open gas turbine cycle leaves some room for improvement [2]. A 'carnotization' of the gas turbine cycle, i.e. a heat addition in the combustion chamber at higher average temperatures, is justified by a theoretical gain in cycle efficiency and an increased power density. A technical approach to this is the sequential combustion (Fig. 1.4b), where a high pressure turbine only partially expands the fluid from the first combustor, before it is reheated in a second combustion chamber and finally expanded in the low pressure turbine to ambient pressure.
This reheat concept [3] was realized by ABB in the 1990's and further developed by Alstom. After Alstom's withdrawal from gas turbine industry in 2016, the technology was split between US-American General Electric (GE) and Italian Ansaldo Energia.
The exhaust gas at turbine outlet still contains sensible heat regardless of the reheat concept. This waste heat can further drive a steam cycle, adding complexity to the power plant but increasing the overall efficiency to the 60+ % range for the modern H-class, hence making these combined cycles the most efficient fossil fuel-based power plants at large scale.

1.1.2. Worldwide Gas Turbine Use

The gas turbine offers many advantages in power generation, which are for example the outstanding cycle efficiency in a combined process with a steam turbine and the steady operation, enabling high power densities with a clean and fuel-flexible combustion. Thus, different application scenarios for gas turbine use exist, depending on the regional demands and the availability of fuel, i.e. natural gas in most cases. Emerging economies with a remarkable economical growth utilize the gas turbine as a reliable and quickly available large-scale power generation [4].
Especially when there are proper natural gas or oil resources available, power generation by gas turbine can also be affordable, as for example in the Middle East with its growing population.
The availability of domestic natural gas fields has also been the reason for a recent boom in the US gas industry, where new gas turbine installation fueled with unconventional gas replaced coal power plants and reduced the traditional US-American dependency on energy imports [5]. Even though the exploration of shale gas increases the total operating costs, US gas turbines are outperforming coal power generation in the electricity market.
Moreover, gas turbines also adapt well to changing external conditions such as fuel variation or flexible load demands, caused by a high share of renewables in regional electricity grid, as for example in Southern California. High solar power generation deforms the classical daily load demand with a peak load at midday to a duck-shaped profile with demand for conventional power in the early mornings and evenings [6]. Even though the number of profitable operation hours decreases, gas turbines can provide this required flexible behavior and remain either in parking positions during midday or even perform a complete shut-down for a few hours.
The high power density for the single cycle design in combination with acceptable (noise) emissions also make gas turbines the favoured solution in densely populated areas [7, 8], such as Japan [9], a country, which is searching for alternatives to its nuclear power industry. Comparable to this application case, combined heat and power processes can deliver district heating at the same time, yielding a positive business case, as was recently proven by the local energy supplier in Dusseldorf, Germany, for a combined cycle plant with district heating [10].
While these local solutions like in Dusseldorf can be profitable, the general gas turbine use in the European, especially the German market, is predominated by other effects: Solar and Wind Power at ‘zero’ fuel costs and subsidized by the state in many ways,

challenge the traditional use case for gas turbines as peak load providers during midday or even as base load suppliers. At the same time, the penetration of intermittent renewable power generation into the electricity market unbalances electricity grids that currently require stabilization by conventional power plants, comparable to the above described case in Southern California, which however benefits from a much more predictable solar irradiation.

Gas turbine combined cycles are technically capable to efficiently balance the grid by frequency response, flexible part load operation, and fast start-up procedures [11]. Still, gas turbines compete in that field with existing coal power plants in Germany, which are also able to deliver residual compensation in the given branched electricity grid. Furthermore, coal power plants consume regional resources of inexpensive lignite instead of imported natural gas, shifting the economical advantage to coal. The changing market position of European gas turbines is thus determined by a decreasing number of yearly operating hours and an ever rising number of engine starts, as displayed in Fig. 1.5 [12].

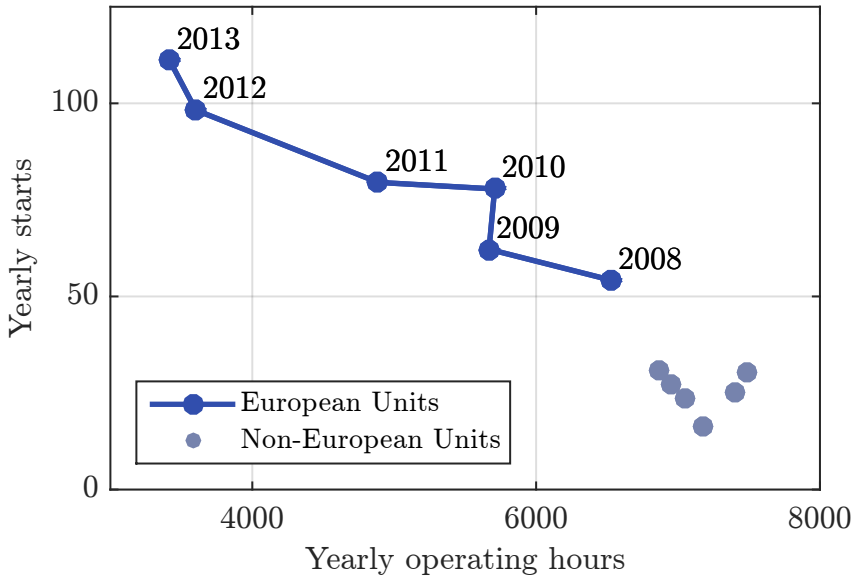

Figure 1.5.: Yearly average starts of European and Non-European gas turbine units of former Alstom type GT24/GT26 show different operation regime. Figure reproduced from [12].

1.1.3. Ecological Aspects of Emission Behavior

NOx and CO emissions even occur during the combustion of 'clean natural gas' without fuel-bound pollutants such as sulfur. Special focus is thus given to NOx and CO emissions in this work, because of the following reasons: First, NOx and CO emissions have

a toxic and possibly hazardous nature to the environment and their emission is thus restricted by emission laws. Second, NOx and CO emissions also allow for an investigation of combustion behavior, since they are closely related to combustion chamber parameters, as will be explained in the following.
Legislative limits for NOx and CO emissions define the available temperature range for gas turbine combustor of a given technology (see Sec. 3.1.1). As the kinetic formation mechanisms for both pollutants (NOx and CO) favor opposite temperature conditions, a characteristic 'bathtub' curve (Fig. 1.6) is obtained (further details on kinetics is given in Sec. 3.3.2.1 and 3.3.3.1). In other words, NOx formation is promoted by high temperatures, while CO is formed under low temperature conditions, when slow reaction rates of CO oxidation inhibit a full conversion of CO to CO_2 in the combustion chamber.

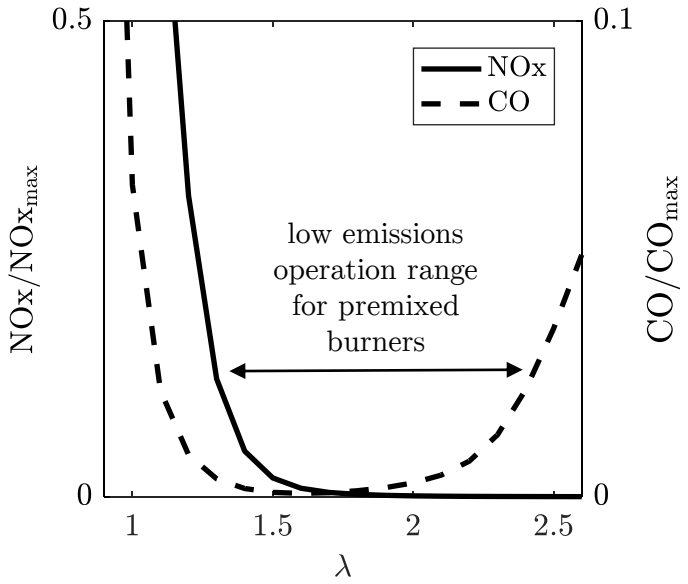

Figure 1.6.: Simulated NOx and CO emissions vs. air-to-fuel equivalence ratio.
Emissions were calculated by a simple Cantera network model (using the Gri30 mechanism), consisting of a perfectly stirred reactor to model ignition (by addition of H-radicals), followed by a plug flow reactor. Fuel and air inlet temperature 600 K, pressure 15 bar and constant plug flow residence time.

Towards fuel-rich, thus towards hot conditions, CO emissions also rise. In this case, there is less excess of air, so that incomplete oxidation of carbon occurs. This formation is however not relevant in conventional gas turbine technology at lean combustion without air recirculation, because O_2 is always abundant.
NOx itself can irritate the humans' respiratory system, increasing the susceptibilty to respiratory infections and aggravate asthma [13]. Additionally, ground level ozone as a

harmful air pollutant causing all kinds of respiratory disorders [14], is mainly formed by the reaction of NOx with volatile organic compounds in the presence of sunlight. In the stratosphere, NOx pollution has the opposite effect on ozone and destroys the earth-protecting ozone layer. NOx emission can also form acid rain with environmental damage like forest dieback.
The colorless and practically odorless CO occurs naturally in low quantities. Concentrations as low as 35-50 ppm are considered tolerable for humans [15]. Longer exposure to high concentrations, however unlikely in gas turbine operation, can though lead to death, since red blood cells are hindered to sustain the humans oxygen supply when carbon monoxide is absorbed by the lungs. Dangerously, the symptoms of that poisoning like headache or fatigue are often misinterpreted, so that poisoning can continue unperceivedly until death [16].
Due to their hazardous nature, NOx and CO emissions are limited by environmental protection laws. NOx emission limits have become more strict ever since their first legislation in the 1970's in the US, resulting in a stagnation of NOx emission per capita for these regions, while the worldwide, and especially the Chinese emissions are still increasing (see Fig. 1.7).

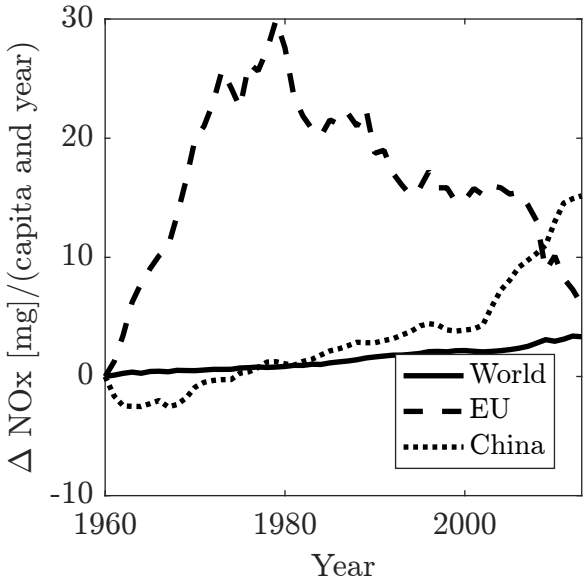

Figure 1.7.: Increase in NOx Emissions per year and capita since 1960 for selected regions [17]

Specific legislative emission limits for gas turbines are often site- and load-specific, but reference-binding limits are defined on national or confederational level: Nowadays limits

for new heavy-duty gas turbine installations in Germany, defined by the 13. BImSchV [18], are at 25 parts per million (ppm)[1], also in accordance with European limits [19], recently upgraded by establishing the best available techniques conclusions [20]. China also applied European standards in the recent revision of their emission legislation [21] for gas turbines.
The United States limit gas turbine NOx emission more strictly to 15 ppm by federal law [22]. Some US states prescribe even lower limits and require site-specific NOx single-digit gas turbine operation, with for example 9 ppm limit in some parts of California [23, 24]. Lieuwen and Yang [25] even report NOx emission limits down to 2 ppm as proposal for the US. Japan's NOx limits are in line with US standards, some regional limits are also in the single-digits [24].
CO limits in the European Union are at least 50 ppm with some countries reducing that number down to 25 ppm, however, only valid in the range of >70% load [26]. The US do not apply CO regulations at the present time [25]. There are nonetheless site-specific limits from 10-40 ppm, which are usually not reached during high or base load operation. Still, part load and flexible operation is expected to be included in CO emission regulations, as recently announced by the European Union for medium combustion plants [27].

1.1.4. Economical Aspects of Emission Behavior

Flexible operation, as demanded in some parts of the world (see Sec. 1.1.2), with daily on-off cycles and more frequent, wider load changes, increase the thermo-mechanical stress on the gas turbine components. That in return may affect performance deterioration due to premature engine aging.
At the same time, cost competitiveness of electricity production demands higher efficiency and thus higher firing temperatures. Accordingly, an increase of flame temperatures reduces the margins to the strict legal NOx emission limits for a specific combustion technology, which may already miss its full NOx reduction potential by premature aging.
Beside the ongoing effort to achieve high efficiencies, current market conditions also require the ability to operate in 'parking position' at low load during times of low electricity prices. Due to the common reduction of firing temperatures with decreasing load, present and future carbon monoxide (CO) emission regulations limit the achievable engine turndown [28]. Aging-induced CO emissions may thus further restrict the market

[1]Emissions limits (in ppm) given in this section are referenced to 15% O_2 and dry conditions

access of a gas turbine, as the CO margin of a given combustion technology to the strict legal limits would be reduced during low-load.

1.2. Motivation and Structure of Thesis

High shares of renewable power generation and existing fossil power plant capacities in developed electricity markets create market pressure on the gas turbine, finding itself in a vicious circle of the simultaneous urge for high efficiency, challenging load conditions and a decreasing on-market time: Lucrative base load operation hours for gas turbines vanish, load and demand profiles reduce profitable gas turbine operation to flexible operation.
While costly component development for efficiency and lifetime improvements are postponed in times of uncertain paybacks, gas turbine service concepts come into spotlight: The share of maintenance costs on total costs generally increases with less operation time, additionally flexible operation requires more maintenance for highly loaded components. Advanced service concepts and health management in the framework of Asset Performance Management (APM) may counteract this techno-economic pressure, as advanced service concepts promise a cost reduction potential [29] in gas turbine operation by employing innovative digital concepts for diagnostics and maintenance.
NOx and CO emissions provide a perfect choice as subjects to these advanced service concepts, as they are constantly monitored. Furthermore, emission limits restrict operation modes and thus profitability and further indicate otherwise inaccessible combustion parameters such as hot gas temperatures. Therefore, their in-depth analysis with regard to aging phenomena, as presented in this work, may contribute to the success of possible future APM concepts.
In the next chapter, such APM approaches, as already integrated in other than the gas turbine industry, are presented as an integrative framework for innovative service concepts. As APM can rely on physically based models and a phenomenological description, literature on gas turbine aging is summarized and existing model approaches for combined aging and emission modeling are presented (Chapter 2). Chapter 3 introduces the chosen method for the investigation of aging-induced emission progression of the GT24/GT26 gas turbine with sequential combustion. Based on the theoretical background of NOx and CO emission formation, semi-empirical emission models are derived. Gas turbine data from commercial operation is processed and enriched by a specifically developed engine model before serving as input to the emission prediction.

The incorporation of aging models into the engine models is assessed for the identification and quantification of aging phenomena with regard to emission progression. Chapter 4 presents the validation of the models for particular engines and evaluates the aging behavior for the engine type by a fleet investigation. A comparison between the physically-based approach and purely statistical models, which is moreover conducted in the framework of this thesis, offers a fundamental benchmark scenario for the evaluation of model approaches in the age of 'big data'. Chapter 5 concludes the findings and sets the results in the framework of APM by giving outlooks to possible industrial applications in gas turbine service.

2. Review on Asset Performance Management and Long-term Emission Modeling

The literature review is divided into three parts. The first section explains applications of APM in various industries as recently reported in the ever-growing field of the 'Internet of Things'. Since APM may require detailed phenomenological knowledge and subsequent modeling, literature on aging in gas turbines and emission modeling is then presented in the following sections.

2.1. Asset Performance Management

Several digital approaches are possible to help improve or regain profitability in technical equipment. Business optimization requires for example detailed market analysis and tries to combine technical processes and the market environment, i.e. planning on-market time according to maximum achievable profit. Since this approach requires market models beside the technical information, it is not further pursued in this work. Another available option for profit maximization in the framework of engine operation is a more technically based APM, as generally defined by the ISO standards [30].
For the energy industry, assets can be understood as the actual physical equipment, including engines, tools and facilities. Performance has a broader definition, covering all types of intended asset function such as power generation, efficiency, reliability and emission compliance. The management component describes the process of controlling the targeted steps in this framework [31].

Álvarez Tejedor et al. [32] structure an asset management system into necessary steps for its application in gas turbines. Fig. 2.1 illustrates the integrative concept of an APM and may help to understand its particular tasks at different levels: Among other imaginable purposes of APM, basic implementations such as constant monitoring and diag-

nostics of physical assets, online re-adjustments and evaluation of the fleet performance are being used to exploit cost reduction potential within an APM. In these examples, asset control values from long-term operation often serve as inputs and indicators for data processing in the APM.

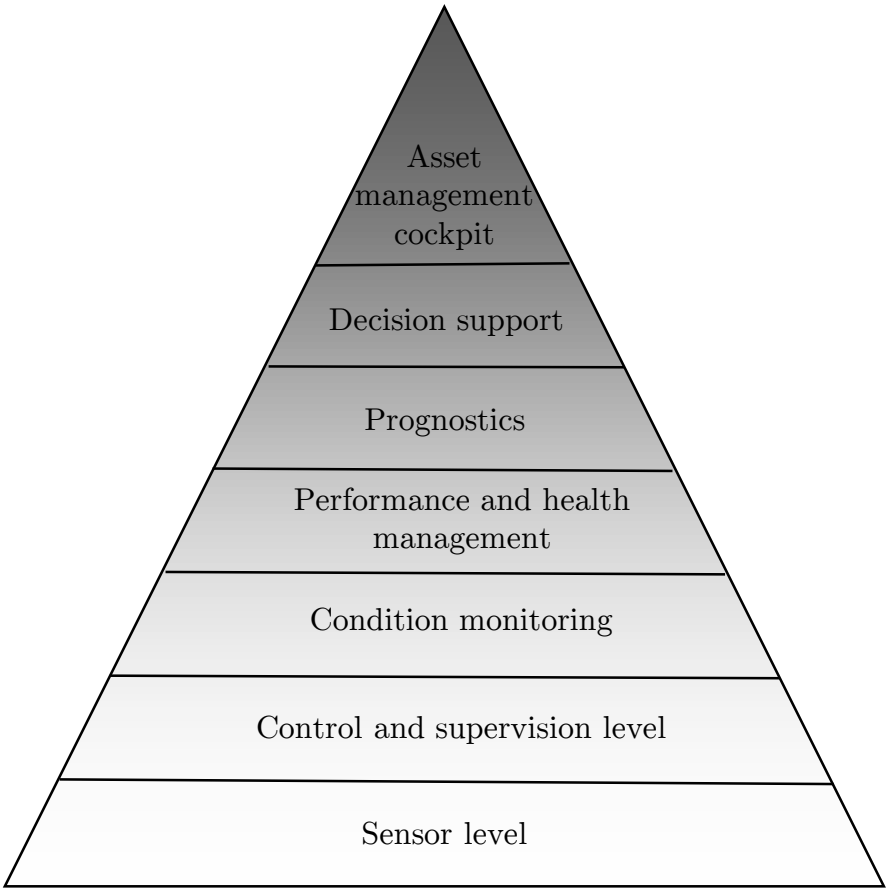

Figure 2.1.: Scheme with particular tasks of Asset Performance Management (APM) in power generation. Figure reproduced from Álvarez Tejedor et al. [32]

Originating from very specific and narrow applications related to condition-based monitoring, new opportunities enabled by the digitalization of physical assets in the 'internet of things' and the evolving 'big data' tools, brought APM into the spotlight in many industrial sectors:
The upstream oil and the shipping industry are predestined for APM by their remotely located assets and the economical and ecological pressure. Operators in the oil and gas industry are already investing in their digital infrastructure, whose top areas of focus are big data analytics and the 'internet of things' [33] to be implemented in a short-time horizon of <2 years. Upstream operating costs are then estimated to decrease by 3-5% and unplanned downtime is forecasted to be reduced [34].

Cost reduction estimations for the shipping industry were taken out of an in-fleet analysis of vessel of the same type, revealing cost reduction potential of 20+% between the market average and best in class liners [35]. The reported road to achieve performance benefits by an APM relies on the development of a digital ship, which is equipped with sensors and monitoring equipment. Data tools in combination with the measurement is then able to process and evaluate voyage (speed, weather, trim,...) and engine (turbocharger, loads, exhaust,...) performance [36]. Similar goals, i.e. fuel savings by optimizing the airplane routes, have already been introduced in the aviation industry by Qantas [37] and Southwest [38] with the help of GE's cloud-based system for APM (GE Predix).
In the framework of this system, GE focuses on the development of 'digital twins' of physical assets [39] for various industries and the application to APM [40] on one single cloud-based platform. This GE Predix [41] as a competitor to Siemens Mindsphere environment [42] has already been successfully implemented in the power industry [43], where great optimization potential is expected by the deployment of 'digital twins' [44]. Among other things, future focus in the area of digitalization of power-generation-assets lies in the life cycle management, thus incorporating time-dependent models for aging and performance degradation in power generation systems [45]. The implementation of APM shows potential for cost reduction, as already successfully proven in other industries. APM as a successor and integrator of simple known diagnostics and monitoring systems to wider applications may utilize physically-based modeling in the creation of these 'digital twins'. Especially in engine health management, low dimensional physical modeling is an affordable and powerful way to either progressively adapt for aging or to train data-driven methods for different aging scenarios [46], which could also be applied to gas turbines.
Thus, detailed investigation of gas turbine aging and emission phenomena and its modeling is required in the context of this work and performed in the following sections.

2.2. Gas Turbine Aging

Gas turbines in operation are exposed to extreme conditions with high pressure, high temperature, elevated flow velocity with quick expansion and high rotor speeds. Even with the use of advanced materials for the highly loaded parts, the engine's performance (including power output, emissions, ...) is likely to change over its lifetime by aging.
At the same time, the increasing number of engine starts (see Fig. 1.5) leads to higher operational costs, because inspection intervals are shortened according to elapsed equiva-

lent operating hours: Typically, 'equivalent operating hours' do not only consider actual operating hours of the engine but also account for the impact associated to, for example, load shedding[1], trips[2] and start-ups [47]. In this case, lifetime consumption of critical gas turbine parts is expected to be higher than during normal operation due to thermal stresses associated with these transient events. Once a threshold of equivalent operating hours ($\approx$ 30.000+ [2]) is reached, a complete inspection of the gas turbine and a replacement of highly loaded hot gas parts is required. Responding to this increased market pressure on operation and maintenance costs, engine upgrades are often developed in order to enable an extension of this inspection cycle duration [48], which also underlines the economic importance of aging monitoring, diagnostics and, above all, its prevention. Relevant failure modes for the hot gas parts are for example high and low cycle fatigue, creep, erosion and corrosion, as reported by Immarigeon et al. [49] for aeroengines.
Also for GT24/GT26 engines, analysis of field experience from inspections hints to increased wear phenomena and drift of operation points as a consequence of more cyclic operation [12].

Degradation is classified into recoverable, permanent and unrecouverable degradation. Component degradation and its effect on gas turbine performanc belong to the latter, according to Meher-Homji et al. [50]. Unrecoverable degradation can only be repaired by a major overhaul, i.e. a costly replacement of the hot gas parts. Other non-recoverable degradation as stated by Meher-Homji et al. [50] is, for example, flow path damage, surface erosion and corrosion, leading to airfoil profile losses, tip and seal clearance increase and drift of control/calibration instrumentation. The effect of bad[3] instrumentation was also described by Gulen et al. [51], who highlight the impact of aging on the gas turbine control system by deviated turbine outlet temperature measurements. False turbine outlet temperature measurements were identified as the root cause for unexpected power output changes.
In contrast, recoverable deterioration includes, according to the definition by Meher-Homji et al. [50], compressor and turbine fouling, while the latter is less prominent in natural gas applications. Among others, Schneider et al. [52] and Therkorn [53] also identified compressor and inlet filter fouling as a main aging process and described actions for their recovery during gas turbine operation, such as online compressor washing. While profile and endwall losses in the turbosets are non-recoverable, as stated in [50], modern active control clearance systems give the possibility to react on aging induced

[1] fast load changes
[2] uncontrolled shutdown

tip clearance changes [54].
In addition, permanent aging is defined by Meher-Homji et al. [50] as the remaining deterioration, even after a major inspection, which affects the unchanged parts, as for example a distorted casing.
Most studies like the ones mentioned above, describe aging phenomena with relation to changes in gas turbine power output, as for example Li and Nilkitsaranont [55]. Only few notable exceptions in literature investigated deviations in the combustion process and related emission progression, despite its importance for gas turbine operation (Sec. 1.1.3). Rudolf et al. [56] described the effect of a seal damage in the combustor of the GT24/GT26 gas turbine, leading to a lack of air in the primary zone and resulting in higher flame temperatures and an increase in NOx emissions. Increasing NOx emissions were also reported by Syed et al. [57], caused by a nozzle degradation in an aeroderivate gas turbine. The nozzle degradation deteriorates the jet angle of fuel and water injection for NOx reduction. The suboptimal interaction between heat release and water injection then cuts the NOx reduction potential, yielding higher NOx emissions.

2.3. Emission Modeling

Since ambient conditions, fuel composition or load regimes vary during long-term operation, aging detection requires a comparison of the actual engine behavior with a suitable reference model, incorporating these external factors and degradation. However, not all emission modeling approaches are suitable for long-term prediction. Common modeling approaches are presented in the following, before their respective suitability to long-term NOx and CO prediction in literature is evaluated.

2.3.1. General Approaches

Different modeling approaches for emission prediction exist, such as rigorous approaches (reactor network modeling, CFD), semi-empirical modeling or empirical/data-driven methods, depending on the exact purpose and available computational power and/or data.
Rigorous models such as reactor networks [28, 58] and CFD simulations [59, 60, 61], are able to predict spatially resolved emission formation and thus allow for detailed investigation of combustor design and operation aspects. The accuracy and success of these methods are highly dependent on the existence and quality of boundary conditions,

such as oxidant and fuel composition and flows, temperatures, pressure and detailed geometry [62].
While CFD simulations need exact component geometry and are computationally expensive, the reactor network approach is usually faster to process, as only simple geometry information is needed. Still, the reactor network approach employs very accurate chemistry. However, this approach also requires additional parameter identification and estimations of parameters such as residence times in different reactors, heat loss factors or degree of unmixedness [63].
Data-driven statistical modeling can be a powerful and fast approach for data analysis of large data sets. For instance, Turgut [64] quantified the influence of ambient temperature on CO emissions for different aircraft engines with empirical models. Similar investigations were previously done by Hung [65].
Artificial Neural Networks as a special application of statistical models are also able to predict pollutant emissions when adequate training data is available [66]. Still, useful information about the governing physical phenomena is not explicitly incorporated in purely statistical models, which inhibits, for example, their extrapolation capacity [67].
Nevertheless, empirical models are commercially available as a replacement for Continuous Emission Monitoring Systems (CEMS), which utilize instrumental gas component analyzers in contrast. Bainier et al. [68] recently reported their progress on the development of such a Predictive Emission Monitoring System (PEMS) for CO, which however requires re-calibration every quarter of a year. The commercially available PEMS are also able to model NOx emissions during commercial operation with input data from the process control system only [69, 70], and are in some cases certified for gas turbine emission monitoring as a very cost-effective alternative to the CEMS. Beside being based on purely empirical models, PEMS can also utilize theoretical models, deploying thermodynamic and combustion physics. While advanced empirical methods with sufficient training data allow for reliable emission monitoring, a major issue for theoretical models is their low performance in long-term prediction caused by gas turbine aging effects, as reported by Swanson [69].
Semi-empirical prediction can be understood as a combination of both, physical and statistical modeling. It can deal with a less complete description of the combustion chamber than purely reactor models or CFD by nature, as (statistical) parameter identification is part of the model set-up. Semi-empirical models thus maintain the underlying physical concepts and component information while keeping the advantage of low computational effort and adaptation to engine-specific behavior, which makes this approach in partic-

ular suitable for long-term modeling.

2.3.2. Long-term Modeling

Semi-empirical long-term modeling with aging incorporation has been applied in only a few cases for emission prediction. So far, some research has been conducted for NOx and CO, as presented in the following.

Lukachko and Waitz [71] carried out scenario calculations for aircraft engines with pseudo-data to study the impact of turbine and compressor efficiency degradation on NOx emissions, which were calculated with correlations available in literature. Bakken and Skogly [72] proposed to replace the stack emission measurement with a NOx correlation in order to assess off-shore gas turbine emissions at low cost. Accordingly, input parameters to the presented NOx correlation were obtained by simulation tools and could also be adapted for aging by adjusting compressor and turbine efficiencies as well as pressure losses in the intake filter.
However, the combination of NOx emission measurements and their theoretical model-based prediction can also serve as additional monitoring parameter for possibly aged hot gas path components, as similarly reported for performance monitoring [73]: Syed et al. [57] reported that, with a data-reconciliation-like approach derived from a network of chemical reactors, deterioration of fuel nozzle characteristics could successfully be detected by an increase in NOx emissions. Recently, combustion chamber aging induced emissions of a GT26 engine were also investigated in a data reconciliation analysis by Rudolf et al. [56, 74]. The data reconciliation technique thereby ensures physical consistency of the (uncertain) measurement data to determine accurate combustor boundary conditions. A model representing aging of the combustion chamber was developed and tested for a limited number of base load operation points only.

CO emission data were less frequently used for long-term scenario calculations and monitoring than NOx emission data. To the author's best knowledge, modeled aging effects regarding to CO emissions have not yet been published. However, other long-term influences beside aging were investigated. Recently, Therkorn et al. [75] assessed burner switch-off concepts for the auto-ignited sequential combustor in the GT24/GT26 gas turbine and successfully modeled its influence on CO emissions with a semi-empirical model. Enriching this approach with accurate kinetics in a simple reactor model, Güthe

et al. [28] demonstrated the capability to capture the effect of fuel reactivity (i.e. hydrocarbon and hydrogen content) at lab and engine scale.

2.4. Statement of Objective

While different applications of APM in a variety of industries already exist and gas turbine emissions as well as gas turbine aging have already been separately studied in the past, their combination has not been systematically investigated. This work aims thus at creating semi-empirical NOx and CO emission models with aging incorporation for online emission monitoring, diagnosis, and operational support in gas turbine maintenance, in order to validate the novel approach of an emission-augmented Asset Performance Management. Therefore, appropriate gas turbine emission models to be developed in this work should be able to provide unique features, such as modeling of aging effects in long-term operation, identification of root causes for emission progression, and extrapolation capability from the originally mapped envelope during engine commissioning to long-term operation.

In order to develop a physically meaningful model with a potentially broad application, general theoretical examinations must be derived from kinetics and supplemented by simulations of a generic and simplified reactor models. Findings from this general analysis provide inputs to the final semi-empirical NOx and CO model, which is identified and validated on three engines from GE's gas turbine fleet of the engine type GT24/GT26. Underlying aging characteristics are investigated in a fleet analysis with respect to operation regime of the engines to generalize the approach. Finally, the purpose of combined aging and emission modeling in APM shall be shown exemplary by future application concepts.

3. Emission Modeling of a Heavy-Duty Gas Turbine in Long-term Operation

The following chapter presents the investigated F-class GT24/GT26 gas turbine, the available data sets and the methods used in this work. Methods used range from semi-empirical emission modeling for NOx and CO, approaches for aging detection to advanced statistical methods employing statistical modeling and data-driven artificial networks. These presented methods have the common goal to create redundancy in models and measurements for the reliable analysis of aging induced emission progression. Large parts of this work have been pre-published in Lipperheide et al. [76, 77, 78, 79, 80, 81, 82, 83].

3.1. GT24/GT26 Heavy Duty Gas Turbine

The investigated F-class GT24/GT26[1] gas turbine is a heavy duty gas turbine of the F-class, delivering $\approx$ 500 MW in a 1-1[2] combined cycle configuration. The sequential design with two combustors, followed by a turbine each (high pressure and low pressure), and state-of-the-art variable inlet guide vanes (VIGV) for increased part load efficiency is displayed in Fig. 3.1.

[1] The different notation of GT24 and GT26 refers to the same engine type, which is however used in different markets, i.e. the 'American' 60 Hertz market with a down-scaled version GT24 and the GT26 for the 'European' 50 Hertz market. 60 Hertz turbines must generally be scaled down in order to balance the effect of higher engine speeds, which would increase the mean tangential velocity for a given geometry. At 60 Hertz, the diameter of the gas turbine (and accordingly the entire geometry) is thus reduced to keep the aerodynamic design and the velocity ratios of the 50 Hertz compressor.

[2] In a 1-1 combined cycle configuration, the exhaust gas of one gas turbine is used in one steam turbine

3.1.1. Sequential Combustion

The general architecture of the GT24/GT26 reheat concept (Fig. 3.1) with sequential combustion technology imposes high complexity on the conducted research: The existence of a first high pressure turbine followed by a second combustor and turbine generally augments the possibilities of engine control by splitting the overall fuel flow to the respective combustion chambers.

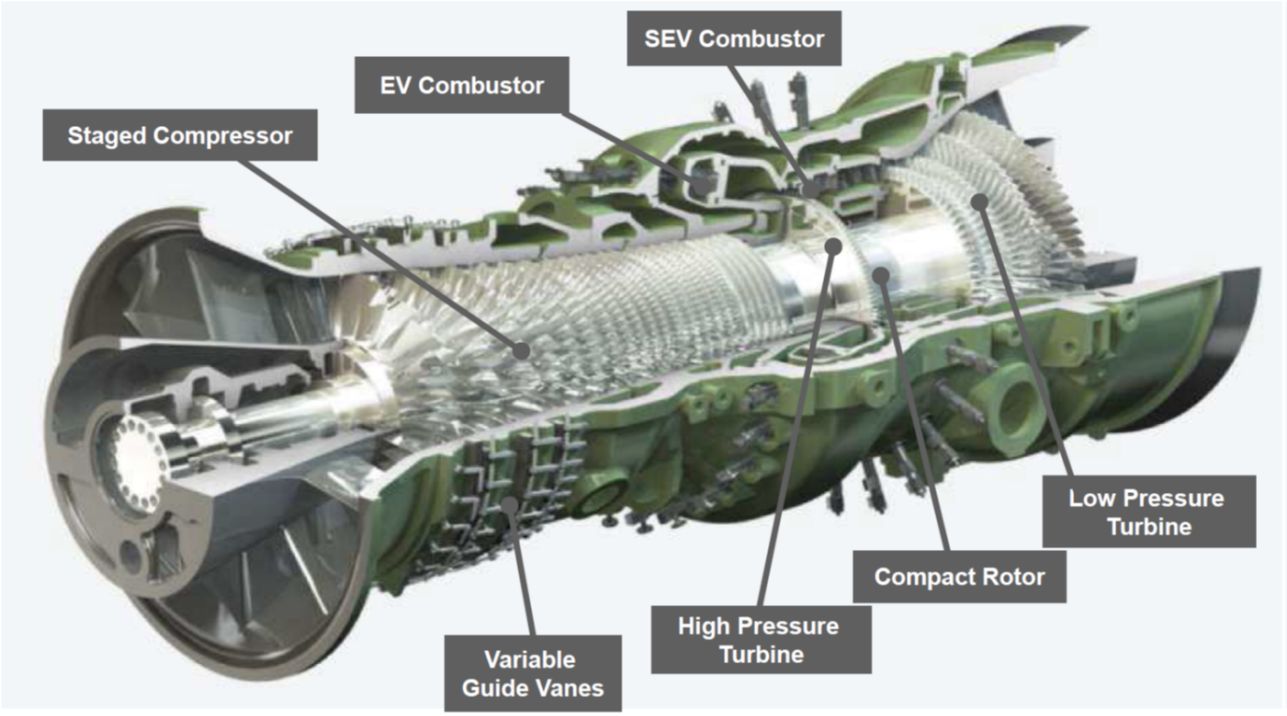

Figure 3.1.: GT24/GT26 with sequential architecture.
Figure reprinted from Lipperheide et al. [76, 80].

This also explains why separate NOx models for each combustor are necessary. The method, as presented throughout this chapter, accounts for the complexity by modeling the independent combustion processes in the EnVironmental Burner (EV) (Fig. 3.2) and Sequential EnVironmental Burner (SEV), as shown in Fig. 3.4. A more detailed model for the EV combustor was implemented on top of this program structure to model the flame zone temperature and aging effects, as explained in Sec. 3.3. In this particular architecture, only the second, auto-ignited SEV combustor, is relevant for CO emission as CO potentially occurring from the first (i.e. EV) combustor is fully oxidized in the SEV. In return, the exact inlet composition of the oxidant, which is the exhaust gas from the EV combustion chamber plus cooling air, remains imprecise and its calculation may add undesired inaccuracy to the method. The uncertainty in this gas composition

further demonstrates the superiority of the semi-empirical approach, which does not have to rely on exact gas parameters but on more global measurements.

Both combustors feature a lean premixed combustion and an annular setup, i.e. a circumferential burner placement with one open annular combustion chamber. However, the two installed combustors differ in their flame stabilization approach: vortex-stabilization (EV) and stabilization by auto-ignition (SEV).

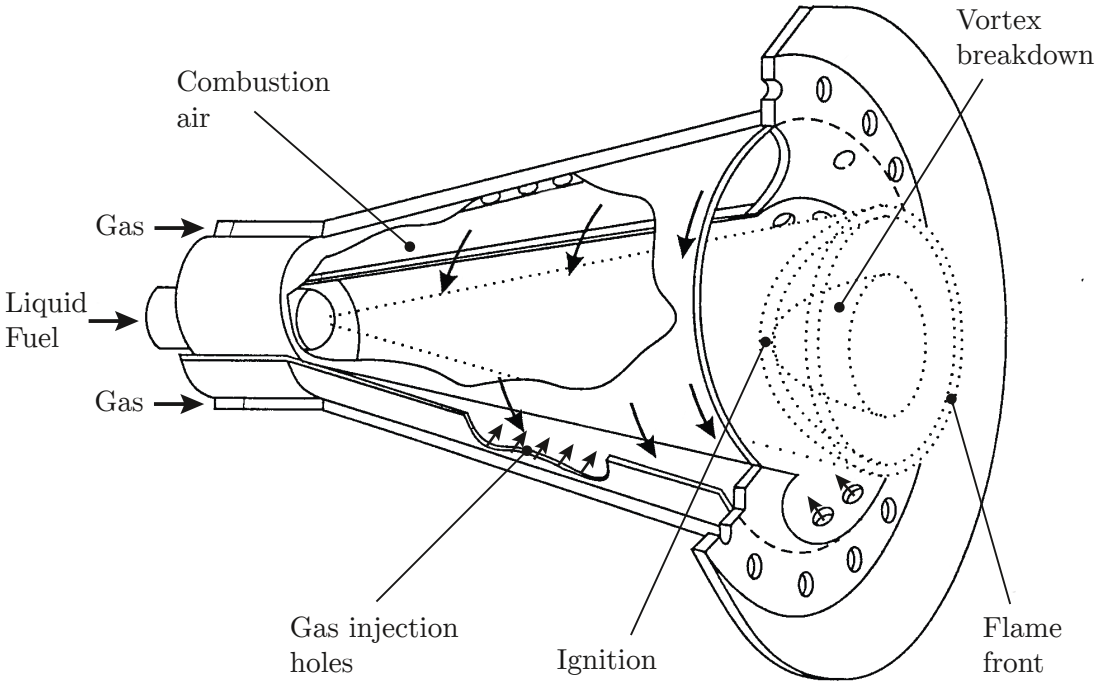

Figure 3.2.: Schematic drawing of EV burner as in the original patent by Döbbeling et al. [84].
The fuel lance, which is located in the middle of the half cones, was later introduced to the concept by Zajadatz et al. [85]

The vortex-stabilized EV combustor (Fig. 3.2) consists of two half cone shells, which are displaced against each other, opening two tangential slots. In the premixed mode of natural gas (which is subject to this research), fuel is injected along the tangential slots, enabling a good mixture in the generated swirl. At the outlet of the burner to the combustor, the swirling flow induces a vortex breakdown. The formed inner recirculation zone acts as a flame-stabilizing mechanism, igniting the fuel-air mixture and creating a stable and curved flame front [86]. An evolution of the described burner features a staged operation mode, where a rich zone is created by additional fuel injection ('stage 1') through a fuel lance (see Fig. 3.3) in the middle of the cone [87].

Figure 3.3.: EV burner evolution from original patent as displayed in Eroglu et al. [87]. The fuel lance is located in the middle of the half cones and was later introduced to the concept by Zajadatz et al. [85]

A high 'stage 1' ratio, i.e. a greater amount of fuel is injected through a lance, is required for stabilization at very low flame temperatures/load (i.e. ignition) [85]. When nominal temperature levels are approached, the 'stage 1' ratio is ramped back. At investigated load levels, the 'stage 1' ratio is usually kept constant and is thus no subject to further investigation.
The SEV combustor (Fig. 3.4), which is located downstream of the high pressure turbine, features a different ignition and thus stabilization technique. SEV burner inlet temperatures are close to the high pressure turbine outlet conditions and therefore significantly higher than average burner inlet (=compressor outlet) temperatures.

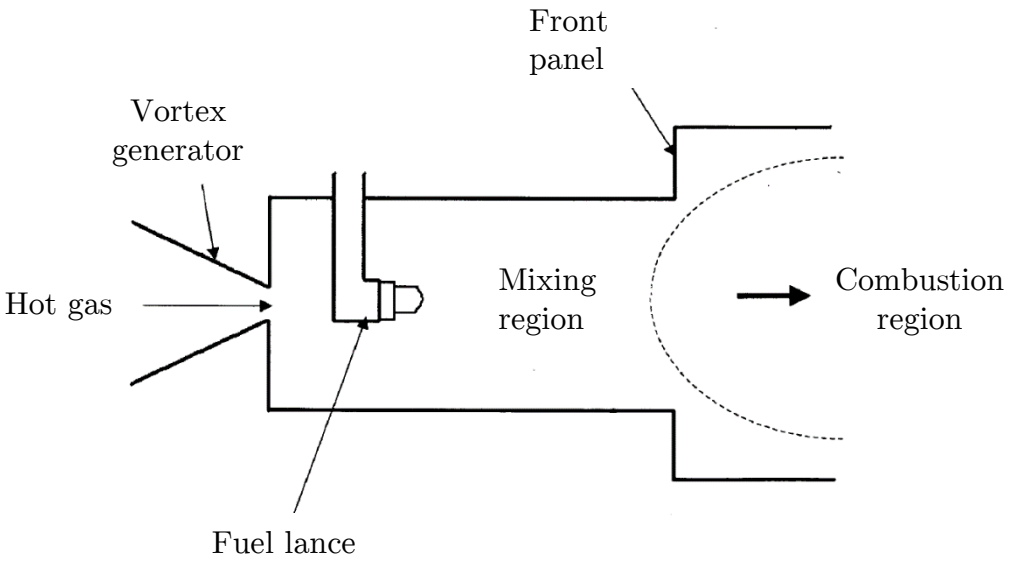

Figure 3.4.: Schematic drawing of SEV burner from Poyyapakkam et al. [88]

The high temperature range enables an auto-ignition of the mixture after injection of fuel to the hot exhaust gas from the EV. This auto-ignition effect also allows for a simple

combustor architecture [86]. A key factor for successful operation is the adjustment of the ignition delay, enabling a good mixing on the one hand, and ensuring the desired flame stabilization by self-ignition on the other hand. Mixing itself is enhanced by vortex generators upstream of the fuel injection [89]. Since fuel is surrounded by a relatively cold carrier air shield at injection, it is prevented from igniting spontaneously in the mixing zone but is auto-ignited after the sudden expansion at the front panel, where a stabilizing recirculation zone is formed at the wall region.

3.1.2. Combustor Operation

The sequential architecture leads to a special characteristic, which is crucial for the gas turbine control: Since the total fuel flow ($\sim$power) is split between two combustors, the standard control parameters VIGV and turbine outlet temperatures allow many possible combinations. Generally, the fuel split by engine control is achieved by a schedule-based control concept, based on turbine outlet temperature measurements or based on simple algebraically calculated inlet temperatures. Depending on the total load ($\approx$ VIGV), either the outlet or the simulated inlet temperature is a leading control parameter for one combustor and is adjusted within its respective material and thermodynamic limits (schematically shown in Fig. 3.5). Thus a range of possible temperature settings allow for myriad combinations for a given total fuel flow without impacting the overall power significantly.

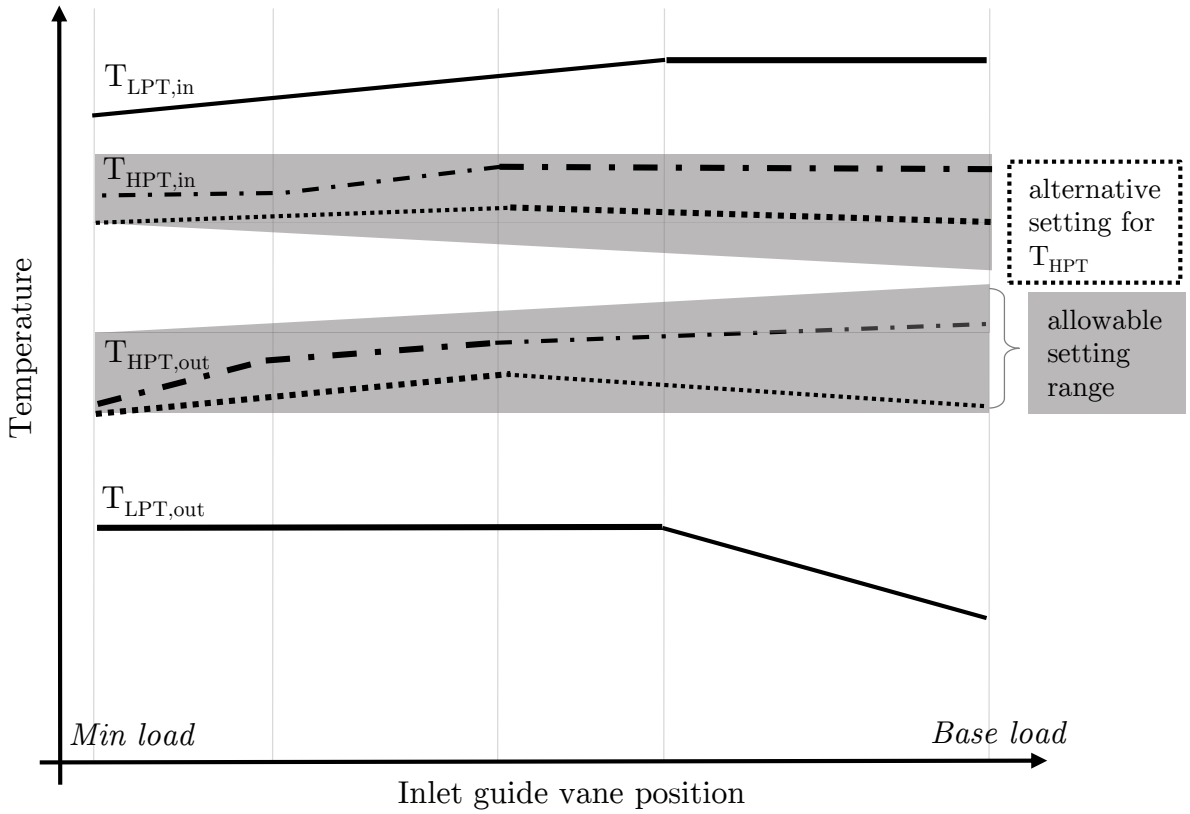

Figure 3.5.: Exemplary temperature set points for fictional operational concept (OPC). Thick lines indicate active limits, thin lines are corresponding coupled temperature trends.

The flexibility as a feature of the sequential architecture also allows for an adaptation to changing fuel compositions and engine conditions. The burner concepts (swirl stabilized and auto-ignition) favor for example different emissions throughout the lifetime of gas turbine components, as will be later shown in this work, so that an adjustment of fuel split according to the engine state or the fuel supply may counteract undesired gas turbine behavior in long-term operation.

3.2. Available Data

As data build the foundation for this work, its availability and quality determines the possibilities and the success of modeling. Thus, special focus is given to the presentation and pre-processing of data in this chapter.
Four data sets were employed in the course of this work:
1. Detailed design information from a gas turbine model of the investigated engine type served as a source of information for component behavior, such as compressor and turbine mapping with respective cooling air flows, pressure levels, and estimated temperatures.
2. For model identification, there were two different data-sets with measured data available: Commissioning and re-adjustments data.
3. Models, as identified on commissioning data, were tested on long-term operation data.
4. Fleet data from the GT24/26 was used to generalize findings on aging with respect to operation regimes.
As quality and characteristics of the particular data sets differ significantly from each other, they will be presented in detail in the following.

3.2.1. Design Data

The design data set is an output of the OEM's detailed gas turbine model. It was created from a parameter variation of this detailed gas turbine model for different engine set points and ambient conditions. Independent variations of the input parameters yield a full description of the engine's behavior over different load levels and its response to ambient changes. As inherent to low-dimensional gas turbine modeling, important intermediate state variables such as temperatures and flows, that cannot be measured directly on the engine, are calculated.

3.2.2. Commissioning

Commissioning and re-adjustments include a variation of operation parameters to identify the 'operation window' with respect to pulsations and emissions and to correspondingly determine operational settings. Commissioning and re-adjustment measurements are usually manually carried out[3], often with additional instrumentation, e.g. for accu-

[3]Data points may thus include time-averaged values as well as single data points whose stationarity is assessed through monitoring by the commissioner.

rate emission measurement and to allow detailed heat balancing with the aid of original equipment manufacturer (OEM) design models. Commissioning and re-adjustments data thus include high quality data of the gas turbine, compromising additional exhaust gas measurements and larger variations of combustion parameters. Thus, this data set (see Tab. 3.1) covers large parts of the typical commercial operation window where initially fixed engine set points can be changed or readjusted from one operation concept to another during an investigated time period. Tab. 3.1 shows the available data points for the respective emission analysis after removal of potentially erroneous measurement points and disregard of irrelevant operation ranges.

Table 3.1.: Available data points for investigated engines during engine commissioning

	engine A	engine B	engine C
# data points NOx	124	186	168
# data points CO	25	32	30

For the NOx investigations, low load points (<60% of base load) were ignored. Similarly, data points with irrelevant operation conditions outside previously defined CO thresholds were also disregarded. Potentially erroneous measurements were detected by comparison of the permanently installed Continuous Emission Monitoring System (CEMS) to a redundant, reliable emission measurement system, which is used only during commissioning.

3.2.3. Commercial long-term operation

Operation schedules are fixed after commissioning for commercial operation when long-term data was recorded. This data set consists of five-minute averaged operation data of three GT26 gas turbines including standard measuring points such as pressures along the gas path, turbine outlet temperatures, ambient conditions, fuel flow and fuel composition. Data was further processed using a mild filter (see Sec. 3.2.5) to remove occasional signal errors after deleting irrelevant operation conditions such as rotational speeds out of the nominal grid frequency or stand-still times with no fuel mass flow. Additionally, the emission-specific thresholds, as defined for the commissioning data set, were also

applied to the long-term data. Remaining data points after filtering for NOx and CO modeling are given in Tab. 3.2.

Table 3.2.: Available data points for investigated engines during long-term operation

	engine A	engine B	engine C
# data points NOx	85,735	126,132	162,191
# data points CO	152,742	151,491	178,875
time period	1,248 days	885 days	984 days

Since data from commercial operation is intended for monitoring and diagnostics purposes, it shows less absolute measurement accuracy than data of, for example, performance testing. In contrast, a satisfying repeatability of measurements is necessary for methods using trend analysis of specific values as often used in monitoring and diagnostics [90].

3.2.4. Fleet Data

In addition to the three engines with the enhanced data sets (commissioning + long-term, knowledge of operation concepts and service intervals), raw data of a large part of the GT24/GT26 fleet was available. In total, 25 engines feature data record and transfer, yielding a data set of 100+ years of operation. This data set includes variations in operational concepts (OPC) (load regimes) and may thus generalize the aging approach and link it to the mode of engine operation.

3.2.5. Filtering of Long-term Data

As the main purpose of the measurement system installed for long-term monitoring is operational safety, some surplus parameters, which can however be precious for modeling, may be outliers. Thus, a filtering technique was applied to long-term data from commercial operation. The filtering itself utilizes a density-based technique: This concept implements the idea that data points are more reliable when a similar combination of measurements is acquired several times during normal operation, which makes the measurements temporally independent from each other. Thus, the so-called time-dependent density weighs each cluster of data points according to their total number and temporal appearance during normal operation. Scattered clusters below a threshold of time-

dependent density are deleted. A time-dependent density filter was processed using a load parameter as first input variable and fuel flows of the two combustion chambers, turbine outlet temperatures and emission data (NOx and CO) as second input parameters. Filtering of emissions was further done by simple outlier detection with a threshold of 95% deviation from the median of all points in a certain load range. The number of available data points after filtering and covered operation period for the investigated engines are shown in Tab. 3.2.

3.2.6. Emission Measurement System

The emission analyzer in the Continuous Emissions Monitoring Systems (CEMS) measures the concentration of NOx and CO in a sample of the exhaust gas. The sample is extracted in the stack by a heated probe and transported to the analyzer by a heated pipe in order to prevent condensation and thus corrosion in the sample lane. The sample is then cooled down in a controlled manner in the analyzer to protect the instrumentation downstream from moisture and eliminate possible interference of water to the analyzed values. Values measured in the CEMS thus relate to a 'dry gas' state. As the distance between the probe location at stack and the actual analyzer leads to a delay in sampling, the emission data must be corrected accordingly by an interpolation at the delay between two five-minute averaged data points before further processing.
The NOx analyzer itself employs the ultraviolet (UV) absorption principle. Distinctive absorption peaks of the NO and NO_2 in the UV spectrum allow for an independent measurement of their concentrations: The detected loss of intensity at wavelengths bands, emitted by a defined UV source and passed through the sample, correlates with the concentration of the absorptive gaseous NO/NO_2. Similarly, the CO and O_2 concentration features non-dispersive infrared (IR) absorption, which carries out a comparable measurement to the NOx analyzer for the IR spectrum, where CO has its absorption peaks.
Despite the fact that NOx and CO are measured in the dry state and normalized to 15% oxygen for legislative purposes, the measurements must be denormalized again and refer to actual concentration in the wet exhaust gas for the modeling approach. This is necessary for a sequential combustion engine since the second combustor reduces the oxygen content significantly depending on the operating conditions, thus the standard normalization to 15% O_2 would bias the analysis. The relation between emission concentration at 15% reference oxygen content and actual measurement is given by:

$$emission_{15\%O_2} = emission_{\mathrm{m}} \cdot \frac{21 - 15}{15 - O_{2\mathrm{m}}} \tag{3.1}$$

The water content in the exhaust gas is recalculated by a global element balance, starting from the remaining oxygen content and incorporating the intake air humidity (see Appendix A.1).

3.3. Modeling

As the core application of the method to be developed is long-term modeling, it must ensure extrapolation capability, thus incorporation of aging and engine-specific behavior. This goal was achieved by using commissioning data at non-aged[4] condition for engine-specific model identification, before applying the model to long-term data. The following paragraph briefly summarizes the underlying steps of the developed method while detailed explanation of datasets and procedures is given in the course of this section.

In a first step a simplified model of the gas turbine was built. This model was aligned to design information and used to determine the (unmeasured[5]) combustion conditions, such as hot gas, flame zone temperatures and air mass flow distribution for a 'hypothetical' design engine. In a second step, available commissioning data was used to identify engine-specific and semi-empirical emission models for non-aged conditions dependent on computed virtual and actual physical measurements for the investigated gas turbine. As mentioned in Sec. 1.1.3 & 1.1.4, special interest among gas turbine emission was given to NOx and CO, whose presence in gas turbine combustion and their underlying formation mechanism are explained.

Subsequently, the engine design model was used to process real long-term continuous data and to extract aging information from this dataset. According to the detected state of aging, output parameter of the model (i.e. hot gas temperatures) were then adapted to aging phenomena. Finally, the output parameters, which then inherently indicated the degree of aging, served as input to the previously formulated NOx model and allowed for identifying different aging effects in comparison to the measured emissions from the regulatory binding continuous emission measurement system.

[4] In this context, non-aged condition describes the engine's state during commissioning, which does not have to be necessarily brand-new, as engines after a major inspection reach non-aged performance despite their pre-inspection operating hours.

[5] As explained later, hot gas temperatures are usually not measured during operation as the high temperatures would not allow reliable temperature measurement over a significant period of time at reasonable costs.

It is worth noting that this method enabled a clear distinction between data used for model identification (i.e. commissioning data) and model validation (long-term data from commercial unit operation).

3.3.1. Simplified Engine Model

Very high temperature levels and the complex mechanical structure of gas turbines impede reliable measurements in the hot gas path of the engine. In commercial industrial turbines, direct hot gas temperature measurements are therefore not performed. Due to its major influence on combustion performance, the combustion temperature must be reconstructed from a simplified engine model in combination with mapped components (see Fig. 3.6). The same applies to the air mass flows entering the combustor, which cannot be measured either, as well as to the power output of the gas turbine in a single-shaft configuration.

Design data can serve as a data basis for the development of component models in order to reconstruct such 'virtual' measurements. Component models can be understood as mappings for the reconstruction of the unmeasured, 'virtual' state variables from measured parameters. These models, or mappings, were created to gain surrogates of the detailed design data (see Sec. 3.2.1) by so-called observer models. When building the model, the target variable is the design data equivalent of the 'virtual' state variable; input parameters to the model f are taken at locations that have corresponding measurements in the commissioning and long-term data set.

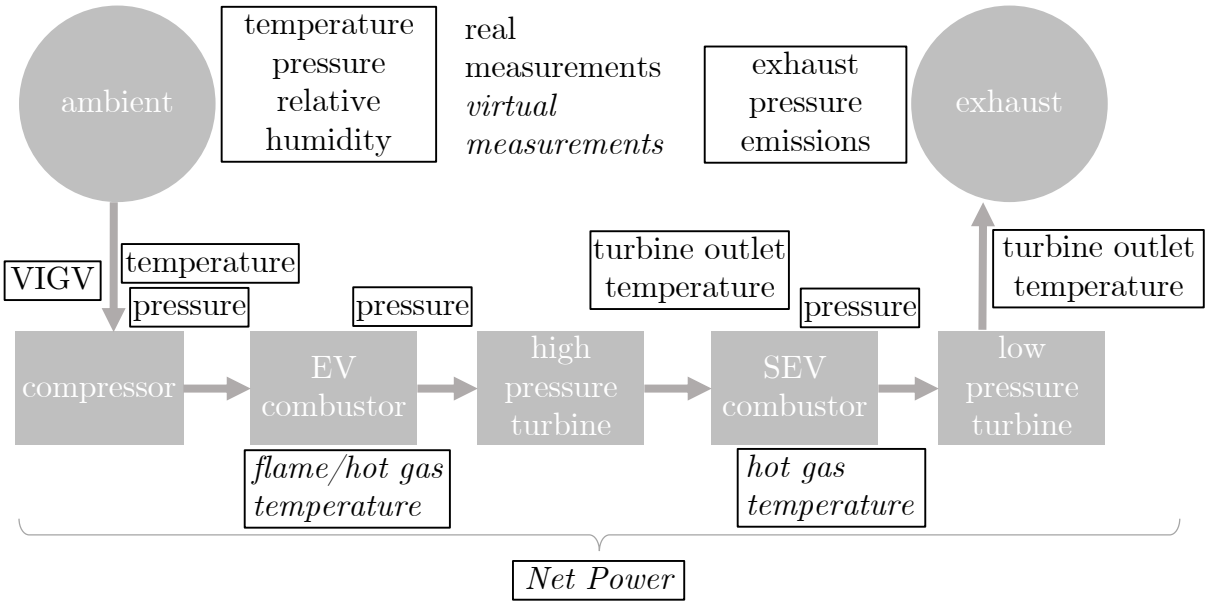

Figure 3.6.: Simplified engine model.
Figure reprinted from Lipperheide et al. [76, 80].

3.3.1.1. Hot Gas Temperature Assessment

Temperatures in the combustors as used in this study are defined as follows: The hot gas temperature T_{hg} corresponds to the mixing temperature at the combustor exit with combustor cooling air already mixed into it. The flame temperature T_{flame} as used for the EV combustor solely corresponds to the temperature without the mixing of combustor cooling air.

For the SEV combustor, only one hot gas temperature is relevant for modeling, as the difference between SEV hot gas and flame temperature is expected not to change significantly with time. In contrast to the EV combustor, geometry and cooling air distribution is kept simpler in the SEV combustor. The cooling air distribution is thus less prone to aging effects.

Concerning the estimation of the hot gas temperature, two different approaches were available. With the first approach, named 'energy-balance-calculation' in the following, the hot gas temperature can be computed with a simple combustion calculation, i.e. an enthalpy balance between reactants and products, considering complete oxidation of the fuel species. This calculation, however, requires reliable information on fuel composition/mass flow and air mass flow. Another approach, which is referred to as 'turbine-characteristic-method' in this work, uses the mapping approach as described in Sec. 3.3.1 to derive the hot gas temperature from measurable parameters such as the

turbine outlet temperature and the pressure ratio over the turbine (see Fig. 3.7).

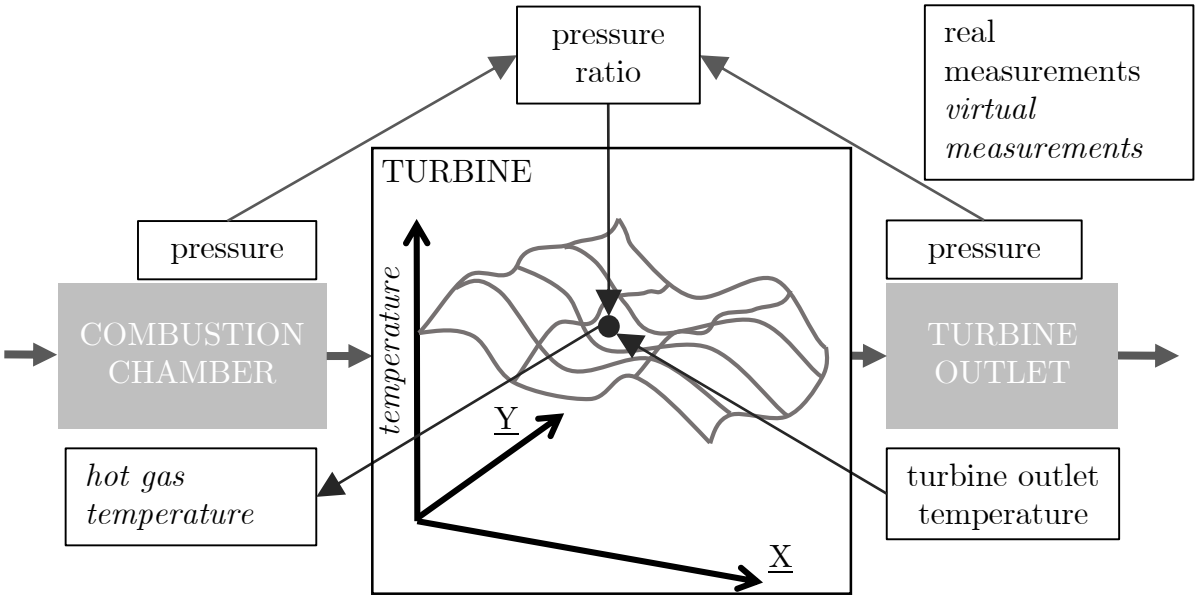

Figure 3.7.: Component modeling approach for hot gas temperature assessment by mapping. Actual measurements for turbine outlet temperature and pressure ratio over the respective turbine define main input parameters to a mapping, which accordingly outputs the hot gas temperature as a virtual measurement.
Figure reprinted from Lipperheide et al. [83].

While the 'energy-balance-calculation' seems to be the obvious method, it includes some serious drawbacks. As the combustor air flow must be derived by a compressor flow calculated from a compressor map (see following Sec. 3.3.1.2), it would thus add 'virtual' measurements to the method anyway. Additionally, fuel mass flow measurements may also show a notable uncertainty, as their accurate assessment is not part of the engine control. Measurement and information uncertainties also exist in the 'turbine-characteristic-method', because turbine performance can vary with time and operation. While pressure measurements are considered reliable, thermocouples at the outlet of the high pressure turbine also show measurement errors due to their location in extreme thermal conditions (as explained later in Sec. 3.3.4.1).
Nevertheless, advantages of the 'turbine-characteristic-method' predominate: The 'turbine-characteristic-method' enables fast computation by its analytic formulation. Furthermore, the use of the turbine outlet temperature directly links the hot gas calculation to a parameter for actual gas turbine control during operation.
A second order mapping approach of turbine outlet temperature $T_{\mathrm{HPT,out}}$ and $T_{\mathrm{LPT,out}}$

and pressure ratio π_{HPT}, π_{LPT} respectively, of the turbine was found to match hot gas temperature trends. Remaining residuals between mapping and design data from that step were modeled as a fourth-order function of inlet guide vane position $VIGV$ and ambient temperature T_{amb} (additionally ambient humidity RH_{amb} for SEV temperature) and added to the hot gas temperature prediction method, so that the surrogate model is able to reach an accuracy of ± 1 Kelvin (EV) and ± 3 Kelvin (SEV) for the engine states of interest. Mathematically, the calculation of the hot gas temperatures by the mapping approach with the surrogate models f_{HPT} and f_{LPT} can be expressed as

$$T_{\mathrm{hg,EV}} = f_{\mathrm{HPT}}(T_{\mathrm{HPT,out}}, \pi_{\mathrm{HPT}}, VIGV, T_{\mathrm{amb}}) \tag{3.2}$$

$$T_{\mathrm{hg,SEV}} = f_{\mathrm{LPT}}(T_{\mathrm{LPT,out}}, \pi_{\mathrm{LPT}}, VIGV, T_{\mathrm{amb}}, RH_{\mathrm{amb}}) \tag{3.3}$$

with the variables being measurements. Since benchmark experimental measurements were not at hand, a comparison between the two calculation methods was performed qualitatively. As NOx emission are commonly expected to increase exponentially with temperature (as later explained in Sec. 3.3.2), the functional correlation of calculated temperatures to NOx emission was evaluated in Fig. 3.8 for a limited number of defined temperature variations within the commissioning data set. Especially at low temperatures, the ‘turbine-characteristic-method’ outperforms the ‘energy-balance-calculation’ and was thus selected as approach in this work.

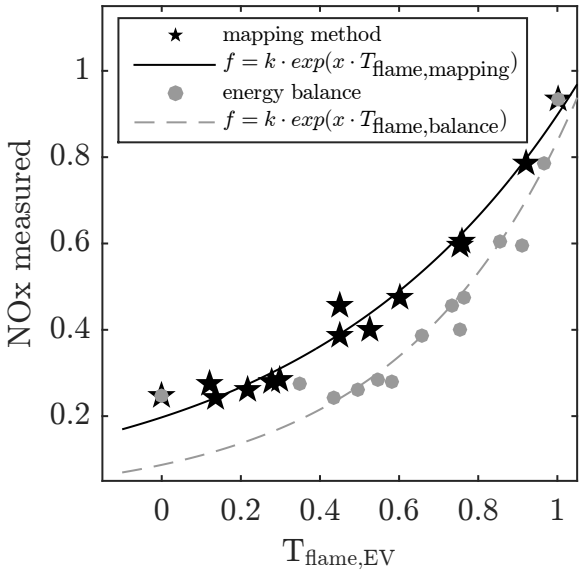

Figure 3.8.: NOx measurements for EV-only operation over calculated flame temperature (calculation of theoretical flame temperature with a)mapping method and b)energy balance) and corresponding fit with expected e-function shape for approximately constant pressure. All scales are normalized to a reference value.
Figure reprinted from Lipperheide et al. [80].

3.3.1.2. Air Mass Flow Assessment

The reconstruction of mass flow, with respect to the specific load point and ambient conditions, was also done through an empirical algebraic model f_{comp}, according to the described approach in Sec. 3.3.1: The model predicts the mass flow as a second-order approximation to inlet guide vane position and ambient temperature, additionally combined with linear models for turbine outlet temperature and ambient humidity influences. The mathematical description of this calculation is

$$m_{\text{comp,out}} = f_{\text{comp}}(T_{\text{amb}}, VIGV, T_{\text{LPT,out}}, T_{\text{HPT,out}}, RH_{\text{amb}}) \tag{3.4}$$

, where T_{amb}, RH_{amb}, $T_{\text{LPT,out}}$, $T_{\text{HPT,out}}$ and $VIGV$ are measured and f_{comp} is the surrogate model of the compressor map, which has been determined from design data at variations of these parameter in design data.
Other possibilities for mass flow reconstruction based on measurements such as a correlation for the pressure drop over the intake filter or a global O_2 element balance for a given fuel mass flow were also tested. However, they did not turn out to be a reliable and accurate method, due to high scatter in the required data (global O_2 element balance)

or missing information and benchmark for the intake characteristics (pressure drop over the intake filter).

3.3.1.3. Power Output Modeling

Performance modeling was not subject to this research, but serves as a tool for validation. However, the single-shaft architecture couples the power output of the steam and gas turbine in the same measurement for a combined cycle power plant. Power measurement can thus only serve as a reference, since details of the steam process and its evaluation over lifetime are out of the scope of the present research.
Performance modeling was also done by mapping. The model consists of a polynomial approach of second order for all independent variables, created and aligned to the design data set (see Sec. 3.3.1). Variables for the performance model were chosen to cover the driving physics of power generation in gas turbines and therefore include expressions for the mass flow ($\equiv$ VIGV position), the enthalpy difference over the turbines ($\equiv T_{\mathrm{hg,EV}} - T_{\mathrm{HPT,out}}$ and $\equiv T_{\mathrm{hg,SEV}} - T_{\mathrm{LPT,out}}$) and the pressure at the low pressure turbine inlet p_{SEV}, which also comprises T_{amb} variations by the characteristic turbine geometry:

$$P_{\mathrm{out}} = f_{\mathrm{power}}(p_{\mathrm{SEV}}, VIGV, T_{\mathrm{hg,EV}} - T_{\mathrm{HPT,out}}, T_{\mathrm{hg,SEV}} - T_{\mathrm{LPT,out}}) \tag{3.5}$$

This performance model was used in the course of this research to double-check turboset aging, as a change of implicitly modeled turbine characteristics would be indicated by an increasing ratio of predicted gas turbine power to the measured combined cycle power.

3.3.2. NOx Model

Before creating the NOx model, which was adapted to the purpose of long-term emission modeling, driving formation phenomena are presented. The shape of a semi-empirical function can then be deduced from kinetics and compared to approaches in literature. Last, the process of the model alignment to the investigated engine will be explained.

3.3.2.1. NOx Formation

NO reaction chemistry includes many branched elementary reactions with nitrous intermediate products. Amongst these reactions, driving routes for the conversion of N_2 to nitrogen oxides NO and NO_2 could be identified by extensive research in the last decades, as represented in the standard reference works of, for example, Lefebvre and Ballal [24], Warnatz et al. [91] and Irvin Glassman and Richard A. Yetter [92]. Their

conclusions will be shortly summarized in the following and then transferred to the very-own purpose of this work.

Zeldovich/Thermal NOx In the Zeldovich mechanism, which is also often referred to as 'thermal NOx', nitrogen and elementary oxygen react in a series of reactions:

$$N_2 + O \rightleftharpoons NO + N \quad \text{(R 3.1)}$$
$$N + O_2 \rightleftharpoons NO + O \quad \text{(R 3.2)}$$
$$N + OH \rightleftharpoons NO + H \quad \text{(R 3.3)}$$

Since the activation energy E_a to crack the N_2 bound requires high temperatures, the NOx production by this path is mostly determined by temperature, as the term 'thermal' NOx indicates.

NO_2 pathway The NOx production over the N_2O-intermediate was found to be important in lean conditions ($\lambda > 1.24$) and under high pressure, which favors the three-body reaction with inert shock partner 'M' [25].

$$O + N_2 + M \rightleftharpoons N_2O + M \quad \text{(R 3.4)}$$
$$H + N_2O \rightleftharpoons NO + NH \quad \text{(R 3.5)}$$
$$O + N_2O \rightleftharpoons NO + NO \quad \text{(R 3.6)}$$

Fenimore/Prompt NOx Fenimore [93] proposed an additional reduced mechanism to the Zeldovich mechanism, to account for 'prompt' NOx production in the primary zone by in-flame carbon C and hydrocarbon CH radicals.

$$CH + N_2 \rightleftharpoons HCN + N \quad \text{(R 3.7)}$$
$$C + N_2 \rightleftharpoons CN + N \quad \text{(R 3.8)}$$

NNH route The NNH route accounts for NOx production by H radicals under the formation of intermediate NNH [94]. This reaction path is usually regarded as less present in natural gas fired combustion but can be of major importance in hydrogen-rich fuels, when the concentration of H radicals is higher [95].

$$N_2 + H \rightleftharpoons NNH \quad \text{(R 3.9)}$$
$$NNH + O \rightleftharpoons NO + NH \quad \text{(R 3.10)}$$

The formation of NO_2 from NO Since NO is a very reactive radical, it is oxidized rapidly to NO_2 under ambient conditions via:

$$2\,NO + O_2 \rightleftharpoons 2\,NO_2 \tag{R 3.11}$$

$$NO + O_3 \rightleftharpoons NO_2 + O_2 \tag{R 3.12}$$

At high exhaust temperatures however, NO_2 is not stable, so that the exhaust gas mostly contains colorless NO. Under low-load or hyperstochiometrical conditions, NO-rich regions with a temperature $T < 1200K$ can lead to an undesired conversion to NO_2, the exhaust gas then turns into a yellow color. Under ambient conditions far downstream of the turbine exhaust, NO is slowly oxidized to NO_2 with time.

Contributions of different routes to total NOx Absolute amounts of certain paths to total NOx production are difficult to evaluate. One approach is to eliminate the paths one by one and model the kinetics of the remaining paths in a chemical reaction network, consisting of reactor models (see Appendix B) [96]. However, the paths itself are connected by branching reactions, leading to an inevitable but acceptably small error of this approach [97]. Furthermore, the exact design of the chemical reactor network and boundary conditions also influence the percentage of investigated NOx mechanism of total NOx production.

Temperature dependency The temperature influence on total NOx emissions of gas turbines is most commonly estimated to be exponential [24], regardless of the different reported contribution of reaction paths to the overall NOx emission reported in literature. The assumption of a simple exponential correlation for gas turbine combustion parameters can be explained by a kinetic evaluation of the elementary reactions (Eq. R 3.1-Eq. R 3.12), as described previously.

Eq. R 3.1 of the thermal NOx mechanism is rate-determing in the postflame zone[6], as it has a very high activation energy, causing high sensitivity regarding temperature changes [99]. Together with Eq. R 3.2 and the assumption of a partial equilibrium of N, the formation rate can easily be found to be [25, 100, 101]:

$$\frac{d[NO]}{dt} = -k \cdot [N_2][O] \tag{3.6}$$

[6]The postflame zone denotes the part of a combustion process, where a major part of the fuel-bound energy has already been released. Detailed discussion of the definition is given by Biagioli and Güthe [98].

The temperature dependency of the reaction rate constant k can be modeled by the Arrhenius approach:

$$k = A \cdot \exp\left(-E_\mathrm{a}/RT\right) \tag{3.7}$$

where E_a denotes the activation energy and A is the so-called pre-exponential factor. Eq. 3.6 can thus be extended to:

$$\frac{d[\mathrm{NO}]}{dt} = A \cdot [\mathrm{N_2}][\mathrm{O}] \cdot \exp\left(-E_\mathrm{a}/RT\right) \tag{3.8}$$

The concentration of N_2 can be assumed to be constant. The presence of O-radicals may relate to the temperature-dependent equilibirum of O_2 dissociation but is expected to be higher for in-flame locations due to an elevated free radical generation in the primary zone [102].

Pressure dependency Literature examining the influence of pressure on NOx formation is far less unanimous. Correa [100] proposed that NOx emissions rise with pressure

$$\frac{c_\mathrm{NOx}}{c_\mathrm{NOx,1\ bar}} = p^\alpha \tag{3.9}$$

with an exponent α, for which experimental studies, as reported in literature (see [98] and references therein), yield varying results while values of $\alpha \approx 0.5$ generally seem reasonable for kinetic investigations of the Zeldovich mechanism.

3.3.2.2. Model Function

Biagioli and Güthe [98] and Güthe et al. [3] developed an Arrhenius-like NOx correlation for the EV burner as a simplified form of Eq. 3.8, normalized to a reference flame temperature and extended by the pressure dependency of Eq. 3.9 in the pre-exponential factor. Their findings are based on reactor modeling with detailed kinetics and were validated with high-pressure combustor test rig experiments. As the real GT24/GT26 engine compromises of two separate combustion chambers, each of them must be modeled independently while overall NOx formation of the gas turbine is the sum of EV and SEV NOx formation.

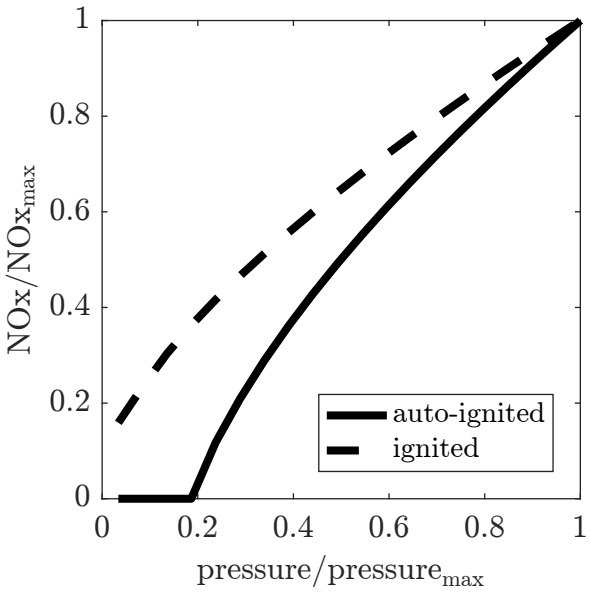

Figure 3.9.: Influence of auto-ignition on NOx behavior over pressure variation for fixed temperature.
Emissions were calculated by a simple Cantera network model (using the Gri30 mechanism), featuring a plug flow reactor with a limited number of of H-radicals added for the ignited case. Fuel and air inlet temperature 1080 K, pressure 1-29.5 bar and constant residence time.

The exact same model function, as shown in Biagioli and Güthe [98] was used in this work for the EV combustor. For the SEV combustor however, this original model was slightly changed to account for the auto-ignition character of the SEV flame, with parameter p_{min} (see Fig. 3.9), being the minimum pressure where ignition takes place:

$$c\_NOx_{\mathrm{EV}} = c\_NOx_{0,\mathrm{EV}} \cdot \left(\frac{p_{\mathrm{EV}}}{p_{\mathrm{ref,EV}}}\right)^{\alpha} \cdot \exp\left(\beta \cdot \left(\frac{T_{\mathrm{flame,EV,ref}}}{T_{\mathrm{flame,EV}}} - 1\right)\right) \tag{3.10}$$

$$c\_NOx_{\mathrm{SEV}} = c\_NOx_{0,\mathrm{SEV}} \cdot \left(\frac{p_{\mathrm{SEV}} - p_{\mathrm{min}}}{p_{\mathrm{ref,SEV}}}\right)^{\gamma} \cdot \exp\left(\delta \cdot \left(\frac{T_{\mathrm{hg,SEV,ref}}}{T_{\mathrm{hg,SEV}}} - 1\right)\right) \tag{3.11}$$

$$c\_NOx_{\mathrm{total}} = c\_NOx_{\mathrm{EV}} + c\_NOx_{\mathrm{SEV}} \cdot \phi \tag{3.12}$$

$$\phi = \begin{cases} 0 & \text{if SEV off} \\ 1 & \text{if SEV on.} \end{cases} \tag{3.13}$$

Input parameters to both equations are pressure p and respective relevant temperature T_{flame} for the EV combustor and T_{hg} for the SEV combustor, which are reconstructed

by the combustor and engine model. While the reference parameters $p_{\text{ref,EV}}$ for the EV combustor or $p_{\text{ref,SEV}}$ for the SEV respectively, and $T_{\text{flame,EV,ref}}$, respectively$T_{\text{hg,SEV,ref}}$ in the equation were set in advance, model parameters such as NOx concentration at reference point $c\_NOx_{0,\text{EV/SEV}}$ and pressure (α and γ) and temperature coefficient (β and δ) were fit with commissioning data.

By doing this, the fitting method itself must account for the special characteristics of data recording in commissioning. During commissioning, the operation window of the gas turbine is assessed by systematically varying its operation parameters (i.e. firing temperatures, internal fuel splits, etc.) in order to determine the settings that satisfy the various targets (e.g. performance, emissions, combustion dynamics). In the course of that procedure, some engine conditions are observed more densely/frequently than others, giving them a higher share of data points. The fitting method must consider this fact in order to avoid misleading formulations that are biased by the uneven distribution of data points, as presented in the following.

A sole fit of the EV combustor in a first step appeared to be a robust method to achieve satisfying results with the limited data available. For this fit, in the case where only the EV combustor is operated, data points were extracted to identify the parameters for NOx contribution from the EV burner. While parameters pertaining to the NOx production of the EV burner were fixed, the parameters of the SEV contribution were then fit to the residuals from all remaining points in a second step. This approach of adding two concentrations is valid here, since NOx emissions refer to the final amount of substance in the exhaust, which does not change significantly in EV-only compared to normal operation. In a third step, the fitting of all available points were evaluated and a slight re-adjustment of the parameters compared to the previously obtained values within predefined bounds was allowed. For the entire fitting process, the Least-Square method[7] from Matlab was used for parameter identification. In order to reduce the dimensionality of the fit, the pressure coefficient from [98] was directly taken from their rig data to a complete engine environment.

[7]Mathematically expressed, this method minimizes the squared error for all n avalaible data points between the measured values y_i with $i = (1, ..., n)$ and the function $f(x_i, \vec{c})$. In this method, parameters $\vec{c}$ are adjusted to match function output of input variables x_i to the measured values y_i: $\min_{\vec{c}} \sum_{i=1}^{n} (f(x_i, \vec{c}) - y_i)^2$

3.3.2.3. Parameter Identification

Tab. 3.3 shows the obtained fitting accuracy from commissioning data for each of the three engines. Parameters vary significantly between data sets due to engine-specific behavior, caused by production and assembly, measurement inaccuracies and available data during commissioning/adjustment, whose distribution was observed to have a great impact on fitting parameters. Especially, availability of EV-only operation is very crucial to the accuracy and the mathematical robustness of the fitting procedure as it determines the first part of the NOx model solely.

Table 3.3.: Model identification from commissioning data: fitting accuracy for NOx model

	engine A	engine B	engine C
rRMSE	0.15	0.55	1.64

A general problem is that pressure and temperature are not varied fully independently from each other during operation of a gas turbine so that one fitting parameter could compensate for another one, thus reducing the meaningfulness of the fitting. Nevertheless, a clear trend is distinguishable (see Fig. 3.10 and Tab. 3.3) and an acceptable fitting accuracy was obtained. Furthermore, Fig. 3.10d) compares the second redundant measurement system, which is only connected during commissioning, to the actual CEMS emission measurements.

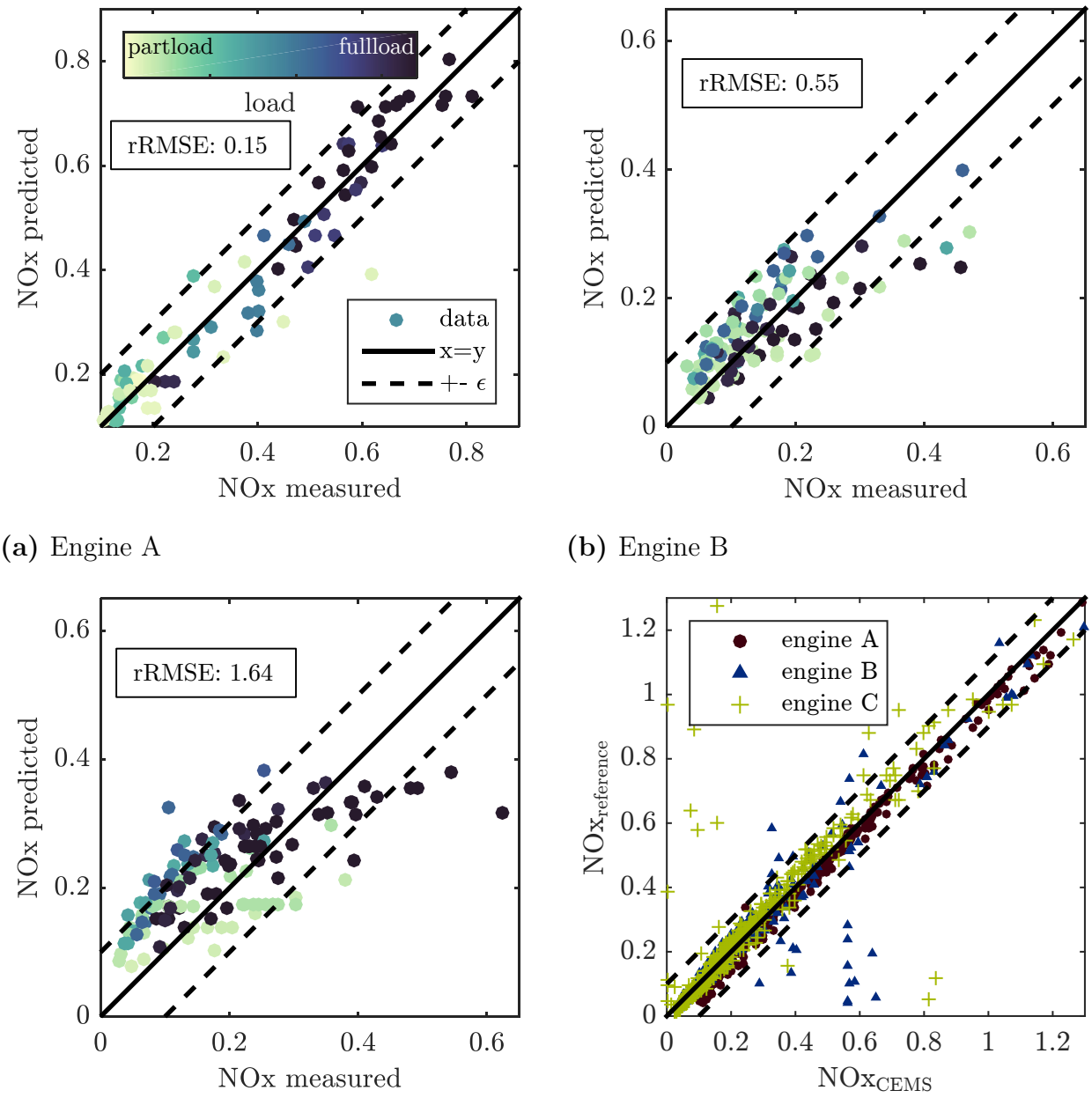

(a) Engine A

(b) Engine B

(c) Engine C

(d) CEMS NOx performance

Figure 3.10.: Model identification (as in Eq. 3.10-3.12) of NOx prediction model and performance of emission measurement system during commissioning. ϵ indicates the expected uncertainty of the measurement system. All scales are normalized to a reference value.
Figure reprinted from Lipperheide et al. [76, 80].

3.3.3. CO Model

CO models can be derived from kinetics easily, as the elementary reactions can be reduced to one driving oxidation reaction. This leads to a semi-empirical formulation,

which has similarly been used before but in a different context. The semi-empirical formulation was then adapted to the special purpose of long-term modeling, with few global combustion measurements available. It was then fitted to the investigated engines.

3.3.3.1. CO Formation

Carbon monoxide (CO) is an intermediate product of the combustion process of hydrocarbons. Detailed investigations on combustion kinetics and reaction paths conclude, that the formation of CO during combustion occurs along many different paths and intermediate products in in-flame kinetics. However, the further oxidation of CO only yields the end-product CO_2, as explained in Turns et al. [103]:

$$\mathrm{CO} + \frac{1}{2}\,\mathrm{O_2} \rightleftharpoons \mathrm{CO_2} \tag{R 3.13}$$

Glassman et al. [104] showed that governing elementary chemical reactions for the CO oxidation can be expressed by the following reduced kinetics:

$$\mathrm{CO} + \mathrm{O_2} \rightleftharpoons \mathrm{CO_2} + \mathrm{O} \tag{R 3.14}$$

$$\mathrm{O} + \mathrm{H_2O} \rightleftharpoons \mathrm{OH} + \mathrm{OH} \tag{R 3.15}$$

$$\mathrm{CO} + \mathrm{OH} \rightleftharpoons \mathrm{CO_2} + \mathrm{H} \tag{R 3.16}$$

$$\mathrm{H} + \mathrm{O_2} \rightleftharpoons \mathrm{OH} + \mathrm{O} \tag{R 3.17}$$

Moreover, Connors et al. [105] and Klarmann et al. [60] stated, that only equation R 3.16 is rate-determing for CO oxidation under gas turbine combustion conditions. Additionally, the concentration of OH is assumed to be in equilibrium ($[OH] = const$) in high-temperature post flame eddies, where CO oxidation occurs [103]. Neglecting the irrelevant inverse reaction, the time-dependent conversion of CO (according to Eq. R 3.16) then follows the simple differential equation:

$$\frac{d[\mathrm{CO}]}{dt} = -k \cdot [\mathrm{CO}] \cdot [\mathrm{OH}] \tag{3.14}$$

The solution of Eq. 3.14 is an exponential function that asymptotically approaches zero, as the reverse reaction is neglected[8]. Accordingly, the occurrence of CO in gas turbine exhaust gas is caused by insufficient kinetic progress to completion. This can either be caused by a short time $\int_{t_{\text{ignition}}}^{t_{\text{exit}}} dt = \tau_{\text{pf}}$ for post-flame oxidation for a given overall combustor residence time with a long ignition delay or by a small reaction rate constant k due to low temperature levels.

3.3.3.2. Model Function

As a consequence and proposed similarly by Connors et al. [105], the CO concentration can be modeled as a decreasing exponential function of a dimensionless characteristic time

$$\tau_{\text{red}} = \frac{\tau_{\text{pf}}}{\tau_{\text{cox}}} \tag{3.15}$$

where τ_{pf} is a measure for residence time in the post flame zone and the difference of overall residence time τ_{res} and ignition delay time τ_{ign}. As schematically illustrated in Fig. 3.11, τ_{cox}[9] as a measure for the complete oxidation time implicitly includes the reaction rate constant k while τ_{res} represents the overall residence time.

[8] Otherwise, the more complex function with incorporation of the reverse reaction would asymptotically approach the equilibrium concentration

[9] The complete oxidation time can be understood as the time, which is needed to reach a CO concentration sufficiently close to its equilibrium or, if the reverse reaction is neglected, close to zero.

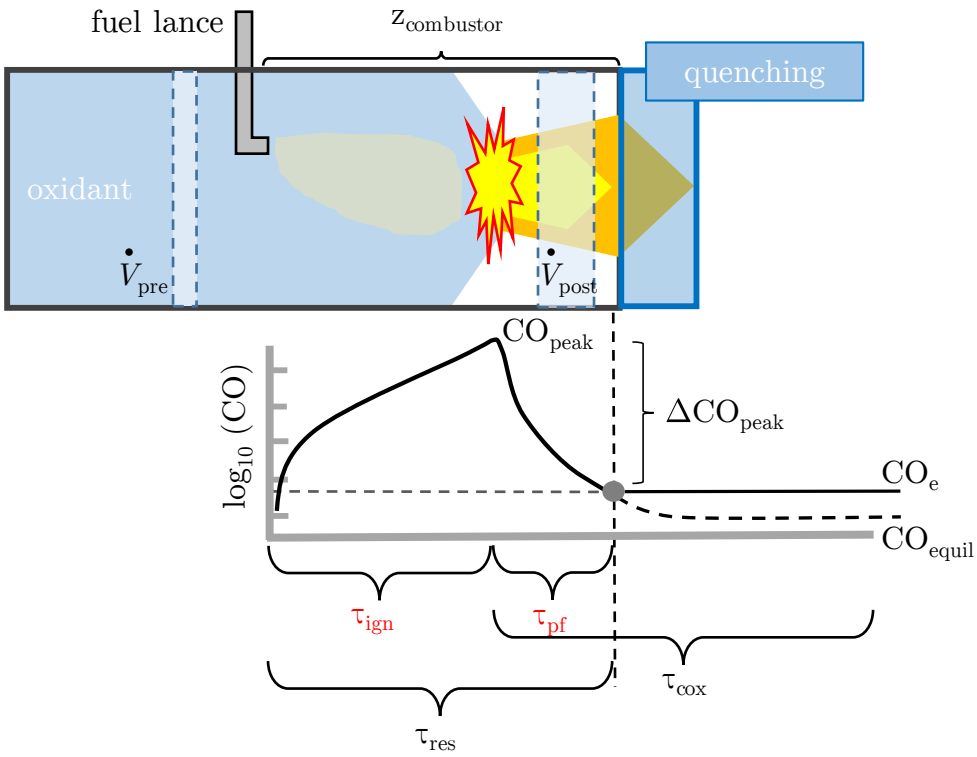

Figure 3.11.: Simple representation CO formation in an auto-ignited combustor

Thus, the dimensionless (reduced) time τ_{red} is a measure for the burnout progression, ranging from $\tau_{\text{red}} = 0$ (no burnout) to $\tau_{\text{red}} =$inf, while the first occurrence of complete burnout is reached at $\tau_{\text{red}} = 1$ (with $\tau_{\text{res}} = \tau_{\text{cox}}$ by definition [28].

The oxidation of CO leads thus to a decline of the initial value CO_{peak} of Eq. (3.14) to its equilibrium CO_{equil} by oxidation of $\Delta CO_{\text{peak}} = CO_{\text{peak}} - CO_{\text{equil}}$ within (reduced) time τ_{red} and slope α:

$$CO_{\text{e}} = \Delta CO_{\text{peak}} \cdot \exp\left(-\theta \frac{\tau_{\text{pf}}}{\tau_{\text{cox}}}\right) + CO_{\text{equil}}$$
$$= \Delta CO_{\text{peak}} \cdot \exp\left(-\theta \frac{\tau_{\text{res}} - \tau_{\text{ign}}}{\tau_{\text{cox}}}\right) + CO_{\text{equil}} \quad (3.16)$$

According to investigations by Klarmann et al. [60] the physical meaning of the 'peak value' is the CO concentration at the transition point from an in-flame CO kinetic to its post-flame equivalent and therefore the starting point of the post-flame oxidation.

While the characteristic-time-based modeling approach described above allows for a detailed chemical modeling giving insights into the chemical processes of CO oxidation, it cannot be successfully extended to the present engine operational data set. Important

boundary conditions such as the fuel and oxidant flows, which these time scales are very sensitive to, are not available during commercial long-term operation with the required accuracy. Moreover, reactor models lack the possibility to adapt for changing engine- or even burner-specific characteristics (i.e. aging) during operation by parameter identification.
The advantage of semi-empirical approaches is thus to allow for the adaption to different burners/engines and the use of already existing or reliable reconstructed measurements. Therefore, the above presented formulation for CO oxidation (Eq. R 3.16) was adapted to standard global gas turbine parameters and made suitable for subsequent application to long-term data with aging.
First, the exponent of Eq. 3.16 was transformed into a spatial dependent formulation so that overall residence time τ_{res} can be expressed by a global combustor length z_{com} and the volumetric flows ($\dot{V}_{\mathrm{pre}}$ and $\dot{V}_{\mathrm{post}}$) before and after combustion, using the assumption of a constant cross-sectional area A_{com} and the kinematic relation of $\dot{V}/A_{\mathrm{com}} = v = \frac{z}{\tau}$ with v denoting velocity:

$$-\theta \cdot \frac{\tau_{\mathrm{res}} - \tau_{\mathrm{ign}}}{\tau_{\mathrm{cox}}} = -\theta \cdot \frac{z_{\mathrm{com}} - v_{\mathrm{pre}} \cdot \tau_{\mathrm{ign}}}{v_{\mathrm{post}}} \cdot \frac{1}{\tau_{\mathrm{cox}}} \tag{3.17}$$

The remaining two characteristic times, τ_{ign} and τ_{cox} were replaced by first-order approximations of global combustion chamber parameters such as pressure p, combustor inlet temperature T_{in}, hot gas temperature $T_{\mathrm{hg,SEV}}$ and respective model parameters κ, ξ, υ, χ, ψ:

$$\tau_{\mathrm{ign}} = f(T_{\mathrm{in}}, p) \approx \kappa + \xi \cdot T_{\mathrm{in}} + \upsilon \cdot p \tag{3.18}$$

$$\tau_{\mathrm{cox}} = f(T_{\mathrm{hg,SEV}}, p) \approx f(T_{\mathrm{hg,SEV}}) \approx \chi + \psi \cdot T_{\mathrm{hg,SEV}} \tag{3.19}$$

While both times depend on their respective temperature levels and on the combustor pressure, the function for τ_{cox} could be simplified due to the coupling of both variables in gas turbine operation, where pressure and hot gas temperature are directly related under given choked turbine conditions for the investigated turbine at the relevant load levels. Equation 3.17, 3.18 and 3.19 were then used in Equation 3.16, where input parameters are normalized to a reference value (denoted by $_{\mathrm{ref}}$) to enhance the numerical stability for later parameter identification:

$$CO_\mathrm{e} = \Delta CO_\mathrm{peak} \cdot \exp\left(-\theta \frac{z_\mathrm{com} - \frac{v_\mathrm{pre}}{v_\mathrm{pre,ref}} \cdot \left(\kappa + \xi \cdot \frac{T_\mathrm{in}}{T_\mathrm{in,ref}} + \upsilon \cdot \frac{p}{p_\mathrm{ref}}\right)}{\frac{v_\mathrm{post}}{v_\mathrm{post,ref}} \cdot \left(\chi + \psi \cdot \frac{T_\mathrm{hg,SEV}}{T_\mathrm{hg,SEV,ref}}\right)}\right) + CO_\mathrm{equil} \quad (3.20)$$

The number of model parameters θ, κ, ξ, υ, χ, ψ and z_com could be further reduced. Introducing $b_1 = \kappa \cdot (\theta \cdot z_\mathrm{com})$ and similar for ξ, υ, χ and ψ results in:

$$CO_\mathrm{e} = \Delta CO_\mathrm{peak} \cdot \exp\left(\frac{1 + \frac{v_\mathrm{pre}}{v_\mathrm{pre,ref}} \cdot \left(b_1 + b_2 \cdot \frac{T_\mathrm{in}}{T_\mathrm{in,ref}} + b_3 \cdot \frac{p}{p_\mathrm{ref}}\right)}{\frac{v_\mathrm{post}}{v_\mathrm{post,ref}} \cdot \left(b_4 + b_5 \cdot \frac{T_\mathrm{hg,SEV}}{T_\mathrm{hg,SEV,ref}}\right)}\right) + CO_\mathrm{equil} \quad (3.21)$$

For further simplification, the choked capacity of the low pressure turbine downstream of the SEV combustor was assumed to be constant and the influence of $\dot{v}_{pre}$ was estimated to be negligible at the given parameter variations, so that both velocities ($\sim$ volumetric flows) were regarded as constant and could be ignored in the numerical expression:

$$CO_\mathrm{e} = \Delta CO_\mathrm{peak} \cdot \exp\left(\frac{1 + \left(b_1 + b_2 \cdot \frac{T_\mathrm{in}}{T_\mathrm{in,ref}} + b_3 \cdot \frac{p}{p_\mathrm{ref}}\right)}{b_4 + b_5 \cdot \frac{T_\mathrm{hg,SEV}}{T_\mathrm{hg,SEV,ref}}}\right) + CO_\mathrm{equil} \quad (3.22)$$

C_{2+} and Humidity Influence Additional determining influences on CO emissions are fuel composition and ambient air humidity due to their significant effects on ignition delay time τ_ign. So called 'long-chain hydrocarbons' C_{2+} show a higher reactivity than pure methane, which results in shorter ignition delays during auto-ignition and thus lower CO emissions, compared to methane combustion at equal combustion conditions. High humidity in the air adversely affects CO emissions as high water content in the oxidant extends the ignition delay. As both phenomena are difficult to assess by gas turbine operation data analysis due to their infrequent and random appearance, a generic reactor, programmed in the Cantera environment in Matlab, served as an auxiliary tool

(see App. B).
The generic reactor features a plug-flow characteristic, which makes it suitable to account for auto-ignition effects, similar to the actual combustor. The chemistry was modeled in detail with the Saudi Aramco Mechanism, developed at the National University of Ireland Galway [106]. Although the assumption of a plug-flow reactor simplifies an auto-ignited gas turbine combustion chamber by neglecting cooling flows, it ensures that the driving pre- and post-flame kinetics of CO oxidation are explicitly modeled without secondary effects. The results of the reactor model as shown in Fig. 3.12 allowed for a calculation of an equivalent inlet temperature T_{in}^{+} at reference fuel composition and humidity.

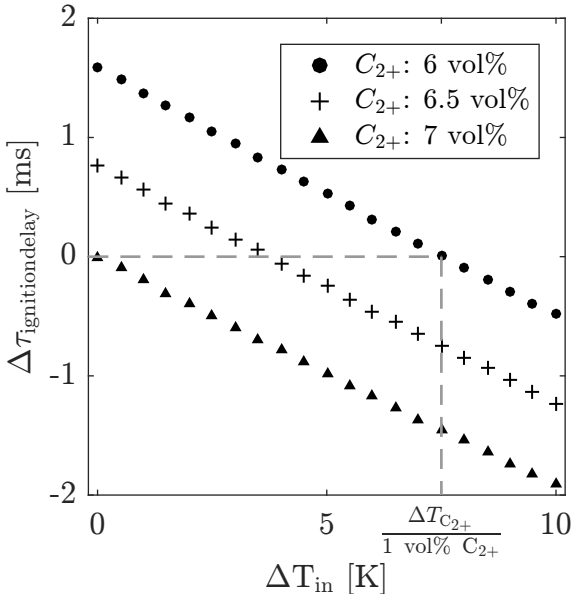

Figure 3.12.: Influence of C_{2+} fraction and combustor inlet temperatures T_{in} on ignition delay as modeled by a generic plug flow reactor

The difference between T_{in}^{+} and T_{in} compensates for the changes in the ignition delay by these effects through a corresponding change in temperature, which would have the same effect on ignition delay:

$$T_{\mathrm{in}}^{+} = T_{\mathrm{in}} + \Delta T_{\mathrm{C_{2+}}} + \Delta T_{\mathrm{humidity}} \tag{3.23}$$

Equation 3.22 is thus extended to:

$$CO_{\text{emission}} = \Delta CO_{\text{peak}} \cdot \exp\left(\frac{1 + \left(b_1 + b_2 \cdot \frac{T_{\text{in}}^{+}}{T_{\text{in,ref}}^{+}} + b_3 \cdot \frac{p}{p_{\text{ref}}}\right)}{b_4 + b_5 \cdot \frac{T_{\text{hg,SEV}}}{T_{\text{hg,SEV,ref}}}}\right) + CO_{\text{equil}} \quad (3.24)$$

The final equation 3.24 served as the governing expression for predicting CO emissions at the SEV combustor outlet as a function of its equivalent inlet temperature T_{in}^{+}, pressure p and hot gas temperature $T_{\text{hg,SEV}}$. The five unknown parameters b_1-b_5 are implicitly related to kinetic and/or engine specific parameters and thus allow for an engine-specific adaption by parameter identification. As CO_{equil} is a purely physical parameter, it was not fitted to the specific engine but modeled by an exponential expression as function of combustor outlet temperature $T_{\text{hg,SEV}}$ only. The value of ΔCO_{peak} was, however, burner specific and dependent on boundary conditions such as air-fuel-ratio or oxidant gas composition. Especially in-flame phenomena are expected to influence this peak value. For the sake of simplicity and mathematical stability of the parameter identification, these influences were not modeled and a constant ΔCO_{peak} was set according to findings from Klarmann et al. [60]. The choice of a constant ΔCO_{peak} is consistent with investigations made by Connors et al. [105]. Their linear modeling approach also sets a constant y-intercept, which can be interpreted as a CO peak value.

Required Measurements While the inlet temperature T_{in} is equal to the measured turbine outlet temperature of the high pressure turbine ($T_{\text{HPT,out}}$)

$$T_{\text{in}} = T_{\text{HPT,out}} \quad (3.25)$$

and p is also recorded during gas turbine operation, the hot gas temperature $T_{\text{hg,SEV}}$ cannot directly be measured. This value is reconstructed from measured engine parameters (see Fig. 3.7) through the surrogate model (see 3.3.1.1).

3.3.3.3. Parameter Identification

The commissioning and re-adjustment data (see Tab. 3.1) of each engine served as the parameter identification data set to determine the parameters b_1-b_5 of equation 3.24 with a Least-Square[10] fitting method in Matlab. Since CO emissions can vary up to

[10]See Sec. 3.3.2.2 for a mathematical description of the least-square method

four orders of magnitude during gas turbine operation, parameter identification, result visualization and evaluation are done in a logarithmic scale (basis 10) to achieve a balanced weighting of the different scales.

Table 3.4.: Model identification from commissioning data: fitting accuracy for CO model

	engine A	engine B	engine C
rRMSE	0.10	0.16	0.13

Fig. 3.13 and Tab. 3.4 show the obtained fitting accuracy for all three engines (Fig. 3.13a)-c)) and an evaluation of the accuracy of their continuous emissions measurement system vs. the redundant one used as a reference during commissioning (d). The model accurately reproduces CO emissions in a wide range but loses accuracy at low emission levels. The low CO concentrations lie within the accuracy range of the measurement system itself, so that a random distribution can be observed in this emission range. The scattered distribution of measurements in the parity plot of the CEMS measurement system and the reference system, which is only present during commissioning, confirms this observation. Thus, low CO emissions below a threshold were initially excluded from all evaluation.

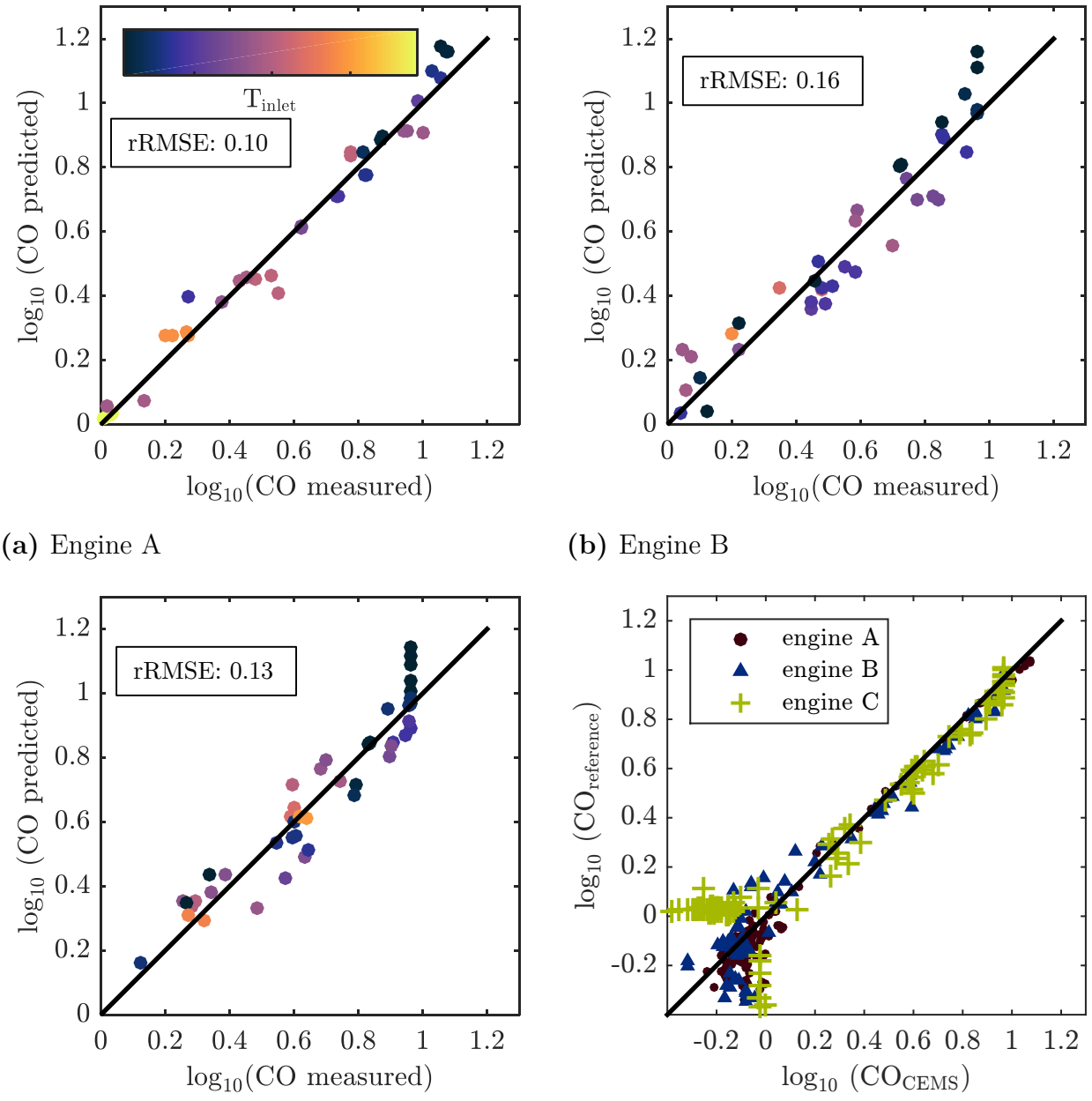

(a) Engine A

(b) Engine B

(c) Engine C

(d) CEMS CO performance

Figure 3.13.: Model identification of CO prediction model and performance of emission measurement system during commissioning. All scales are normalized to a reference value.

3.3.4. Aging Modeling

Two main aging effects on combustion behavior were observed and extracted for further examination and modeling in the course of the research. The first aging effect could be detected at the high pressure turbine outlet temperature, the second one is a change of cooling air distribution in the EV combustor. After linking the identified aging phenomena to root causes and addressing methodological challenges, their impact on emission behavior is explained and modeled in this section.

3.3.4.1. High Pressure Turbine Outlet Temperature

For the given GT24/GT26 gas turbine, the high pressure turbine outlet temperature $T_{\mathrm{HPT,out}}$, which is located and measured at the entrance of the second combustor, is used as a control parameter for the first combustor. This high pressure turbine outlet/SEV inlet section is a complex assembly that is particularly exposed to thermo-mechanical wear due to the high temperatures at the HPT outlet and is thus prone to aging.
Fig. 3.14 shows exemplary two different aging effects related to the high pressure turbine outlet temperature, as similarly reported in literature (see Sec. 2). First, the so-called temperature-shift describes a general negative deviation of the averaged temperature measurements from the actual gas temperature, which was found in the long-term data. Second, the $T_{\mathrm{HPT,out}}$ measurement spread describes the hot and cold spots, respectively their degree of deviation.

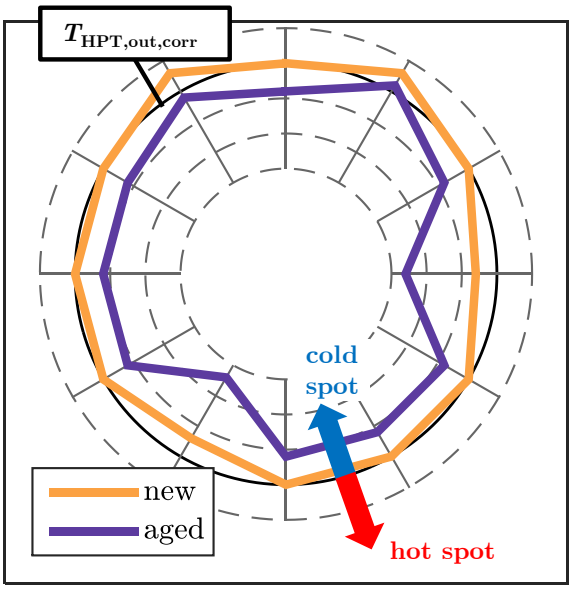

Figure 3.14.: Schematic deviation of circumferential thermocouples in annular combustor to corrected gas temperature. The black circle indicates zero deviation (=ideal initial state).

The temperature inhomogeneity and the general bias can theoretically be induced by different root causes. Part of the temperature deviation can be caused by marginal cold streaks which are assumed to only deviate the temperature measurement by locally cooling single thermocouples. Additionally, thermocouples can be subject to aging/drifting by metallurgical changes themselves which is, however, unpredictable [107], especially in varying operation conditions. At the same time, actual cold gas break-in may create a real, existent and measured cold spot. Cold spots at high pressure turbine outlet can also be caused by uneven annular air distribution in the EV combustor, leading to hotter and colder burners. Such an inhomogeneous temperature is likely to propagate through the turbine to differing temperature zones at the turbine outlet.
The actual contribution of these three different possible root causes (1. temperature drift, 2. temperature spread by cold gas break-in and 3. temperature spread by marginal cold gas streaks and/or metallurgical thermocouple aging) of the observed temperature deviation could, however, not be quantified with the given operation data set. Especially in the hottest part of the engine, the spatial resolution, reliability and redundancy of measurements and the determination of the combined measurement system are not sufficient to detect such detailed flow phenomena. Yet, it was possible by model-based approaches to link observable emission progression effects to these phenomena and in-

troduce state variables to determine the aging progression by phenomenon, as explained in the following sections.

Impact and Modeling of $T_{\mathrm{HPT,out}}$ Measurement Drift Since the amount of fuel injected into the first burner array (EV) is commanded by the control system (see Sec. 3.1.2) in order to reach and stabilize a certain turbine outlet temperature $T_{\mathrm{HPT,out}}$, the $T_{\mathrm{HPT,out}}$ measurement has a direct influence on actual the hot gas temperature. For example, Gulen et al. [51] reported that the spread and drift in turbine outlet temperature measurements lead to a significant difference in power output between two gas turbines of the same type. This is doubtful in this context with the GT24/GT26 architecture, since the EV temperature only marginally affects power and efficiency.
For the given engines, examination of the turbine outlet temperature $T_{\mathrm{HPT,out}}$ over lifetime has shown that temperature measurements tend to measure lower temperatures compared to actually prevailing temperatures. In return, that causes the control system to command higher fuel flow rates to the EV burner while the overall fuel mass flow is set by the total demanded power (see Fig. 3.16). Consequently, this change in fuel split between EV and SEV leads to higher real EV-firing temperatures and thus to an increase in NOx-formation rate. The drift in measured turbine outlet temperature was evaluated in the current research by using the special architecture of the GT24/GT26 gas turbine, where sequential turbine outlet temperature measurements $T_{\mathrm{HPT,out}}$ allow for a quantitative turbine outlet temperature comparison over a lifetime during a certain operation mode.

By comparing the actual temperature difference $\Delta T_{\mathrm{HPT\text{-}LPT,out}} = T_{\mathrm{HPT,out}} - T_{\mathrm{LPT,out}}$ to its initial value $\Delta T_{\mathrm{t=0,HPT\text{-}LPT,out}}$ during the specific operation mode, the actual high pressure turbine outlet temperature could be assessed periodically in operation data (Fig. 3.16). In the course of this assessment, aging effects for the low pressure turbine thermocouples at their moderate environment are assumed to be negligible, as for example the progress of temperature deviation between the spot temperatures at the LPT outlet indicate (see Fig. 3.15, especially in comparison to Fig. 3.18).

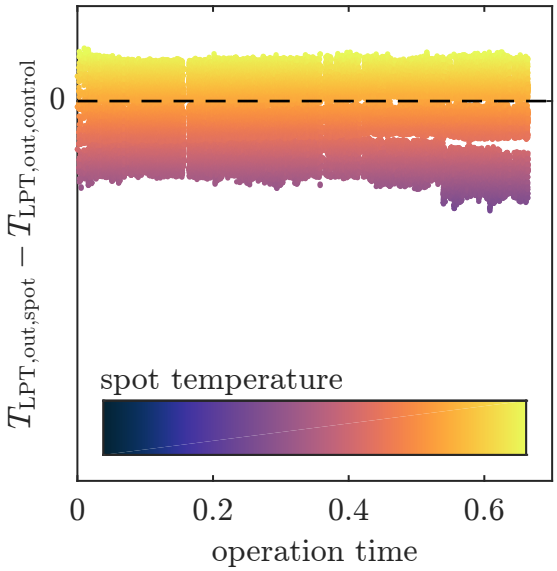

Figure 3.15.: Long-term temperature stability at LPT outlet indicated by deviaton of spot temperatures to control value.
Cold and hot spot temperature is calculated as the mean of the three coldest/hottest thermocouples, average spot temperature is the mean of the remaining thermocouples. Scales not shown due to confidentiality.

The effect of the $T_{\mathrm{HPT,out}}$-drift further justifies the choice of the 'turbine-characteristic-method' for calculation of the hot gas temperature, which directly links the thermocouple aging effect to a deviation in the combustion control. Even though the exact root causes for the temperature drift (as presented in Sec. 3.3.4.1) could not be revealed, the effect is clearly quantifiable with the explained method: The detected temperature drift is processed by the control system, which in return overcontrols hot gas temperature $T_{\mathrm{hg,EV}}$.

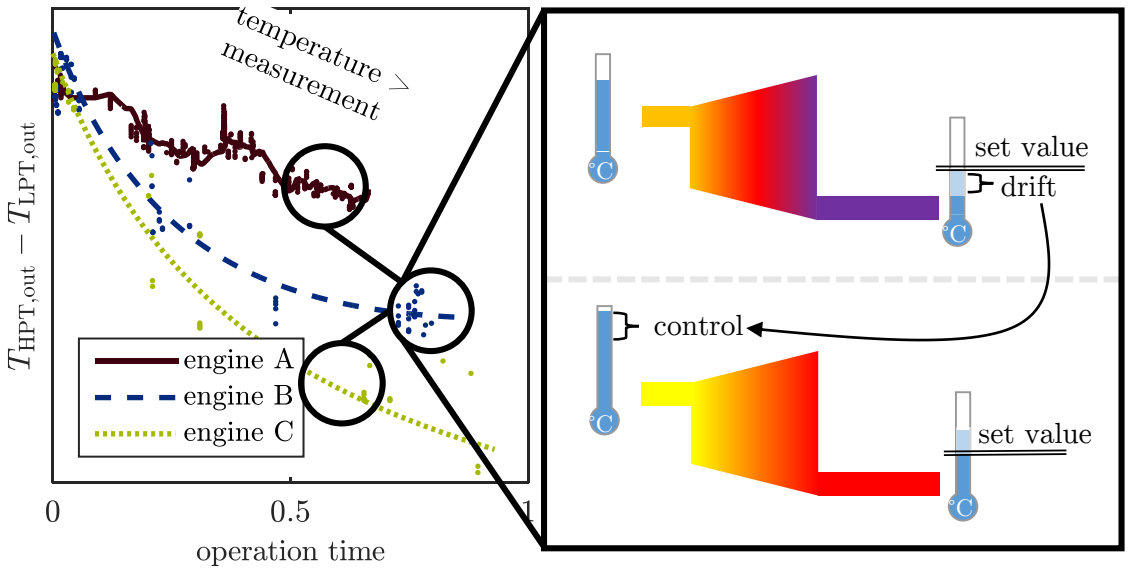

Figure 3.16.: Schematic aging model for temperature measurement drift at HPT outlet. Scales not shown due to confidentiality.
Figure partially reprinted from Lipperheide et al. [76, 80].

The phenomenon of the $T_{\mathrm{HPT,out}}$ measurement drift could be detected redundantly by fuel flow measurements for cases when they were available (Engine A features frequent mass flow measurements of fuel, Engines B& C suffer from infrequent fuel mass flow records):
When the $T_{\mathrm{LPT,out}}$ is set for the maximum load point, the total fuel flow is fixed, too. The split between the two combustors, however, is done by the engine control, which is then obviously mislead by the bad temperature measurement at HPT outlet.
Fig. 3.17 displays the deviation between actual measured turbine outlet temperature $T_{\mathrm{HPT,out}}$ and its calculated equivalent over operation time, based on the fuel split between both combustors. It is worth noting, that a simple depiction of the fuel-flow split instead of reconstructed temperatures in Fig. 3.17 is not possible. Adjustments in the OPC impact the fuel split on purpose, because of changes of the set parameters. This would superimpose the displayed aging effect.

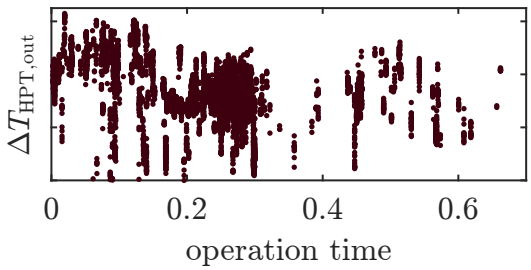

(a) Engine A

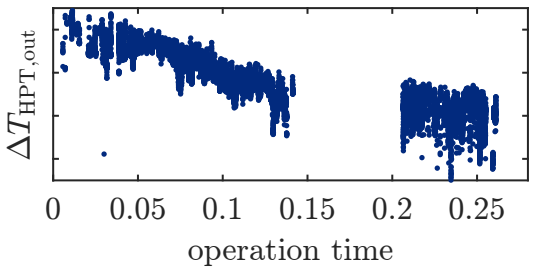

(b) Engine B

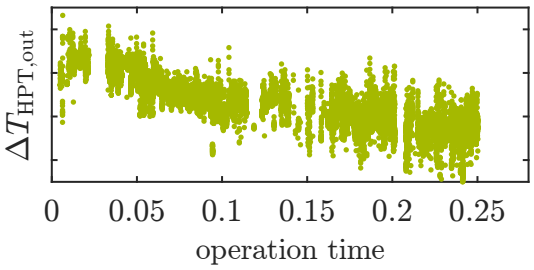

(c) Engine C

Figure 3.17.: Fuel split-based temperature drift $\Delta T_{\mathrm{HPT,out}} = T_{\mathrm{HPT,out,measured}} - T_{\mathrm{HPT,out,calculated}}$ between measured turbine outlet temperature and its fuel-flow-based calculation (according to GE-internal calculations schemes) at base load. Engines B & C lack frequent fuel mass flow data. Scales not shown due to confidentiality.

Impact and Modeling of $T_{\mathrm{HPT,out}}$ Measurement Spread While the use of the high pressure turbine outlet temperature for control purposes employs the mean value of all circumferential temperature measurements, the incorporation of aging to the SEV's second combustor requires a more detailed and spatially resolved approach. Still, the combustion behavior of the second combustor, which is governing CO formation, is influenced by $T_{\mathrm{HPT,out}}$: This temperature is closely related to the combustor's inlet temperature and thus influences the ignition delay, which in return is driving the CO formation in the SEV.

Locally low temperatures increase the ignition delay for individual burners and accordingly reduce the time available for oxidation, eventually leading to a reduced CO burnout and thus to increased CO emissions. Taking such local effects into account, one obvious approach is to determine the individual CO formation of each of the 24 burners within the annular combustor, based on their individually measured inlet temperature. However, a drawback of the method is its sensitivity to single outliers in the temperature

measurement, which are themselves also biased by leakage [79].
A more balanced approach is to group the burners into $g = 3$ groups with $d = 3$ cold burners in group $g = 1$, $d = 3$ hot burners in group $g = 2$ and $(24-2\cdot d)$ average burners in group $g = 3$ according to the long-term behavior of the temperature spread. The total CO formation of the combustor is then the weighted addition of the CO emission of each zone:

$$CO_{\mathrm{e}} = CO_{\mathrm{e,g=1}} \cdot \frac{d}{24} + CO_{\mathrm{e,g=2}} \cdot \frac{d}{24} + CO_{\mathrm{e,g=3}} \cdot \frac{24 - 2 \cdot d}{24} \tag{3.26}$$

The temporary evolution of the zones measurement deviation is displayed in Fig. 3.18 for cold, hot and average zones with a schematic azimuthal temperature distribution for different stages of aging.

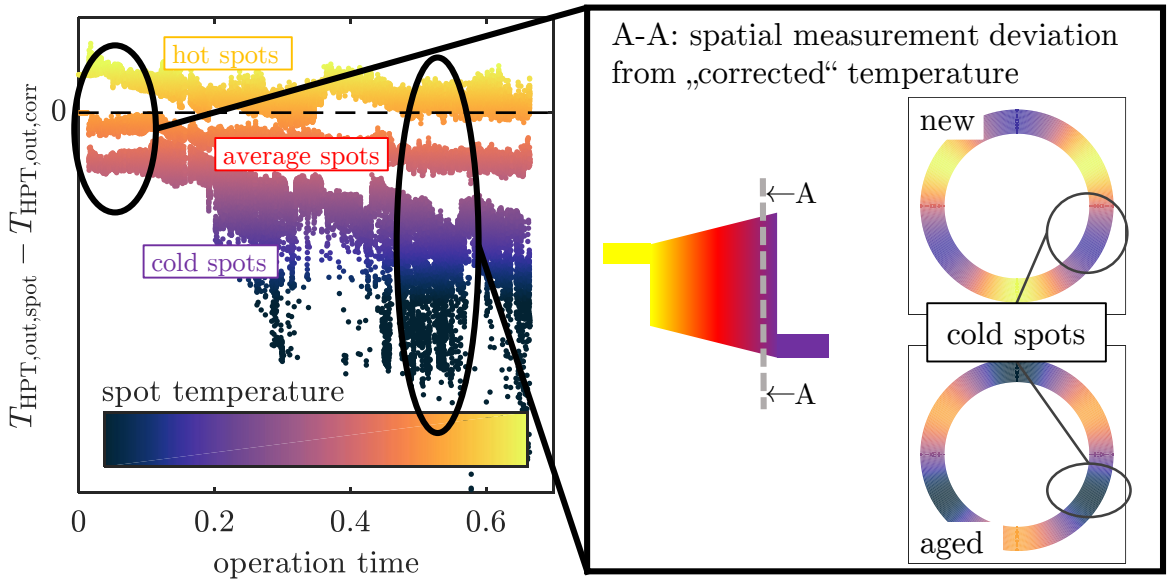

Figure 3.18.: Schematic aging model for increasing temperature measurement spread with same axis scaling as in Fig. 3.15. Scales not shown due to confidentiality.

With ongoing aging of the engine, the actual gas temperature ($T_{\mathrm{HPT,out,corr}}$) itself differs from the average of all thermocouple measurements due to measurement bias described by Lipperheide et al. [79] (see Sec. 3.3.4.1). Based solely on standard gas turbine instrumentation, an accurate evaluation of the root cause and impact of the temperature deviations with aging was not explicitly feasible. As explained before, temperature measurements could either show actual cold zones by shifted cooling air leakage, or just deteriorated measurements by metallurgical aging/drift of a thermocouple and/or marginal cold gas streaks, which are not expected to influence the actual

inlet temperature of an individual burner but only the temperature measurement. In order to account for these two aging influences, i.e. temperature inhomogeneity due to cooling air leakage and measurement bias because of marginal cold streaks/thermocouple aging, temperature measurements for each g^{th} thermocouple group (ranging from $g = 1$=hottest to $g = 3$=coldest) were corrected according to a constant parameter X_{CO} over lifetime t, which is a measure for the share of actual cooling air leakage compared to total assessed temperature deviation (as displayed in Fig. 3.18).

$$T^{+}_{\mathrm{g,in}}(t) = T^{+}_{\mathrm{in,corr}}(t) + [\Delta T_{\mathrm{g,in}}(t=0) + (\Delta T_{\mathrm{g,in}}(t) - \Delta T_{\mathrm{g,in}}(t=0)) \cdot X_{\mathrm{CO}}] \tag{3.27}$$

with

$$\Delta T_{\mathrm{g,in}}(t) = T_{\mathrm{g,in}}(t) - T_{\mathrm{in,corr}}(t) \tag{3.28}$$

where T^{+} denotes the described surrogate temperature to account for fuel composition and ambient condition changes, as detailed in Equation 3.23. Thus, $X_{\mathrm{CO}} = 1$ describes the case, where deviation over lifetime is entirely caused by actual cooling air leakage, whereas $X_{\mathrm{CO}} = 0$ associates all deviation to the measurement bias by marginal cold gas streaks and metallurgical aging/drifting of a thermocouple. As X_{CO} is an engine-specific aging parameter assumed as constant, its constant value was identified from long-term data by minimizing the overall model deviation between CO prediction and measurement.

3.3.4.2. Combustor Flow Distribution

The air flow through the lean premixed EV combustor is guided by a liner, which cools the casing of the combustor through little holes before the combustion air enters the actual burner. This intended air flow may change with aging, due to sealing losses along its way, shifting more cooling flow to larger cross-section when sealing performance deteriorates. The second aging effect which could be observed is an ongoing decrease in (relative) pressure drop Δp_{EV} over the first combustor (EV) for respective load levels (see Fig. 3.19).

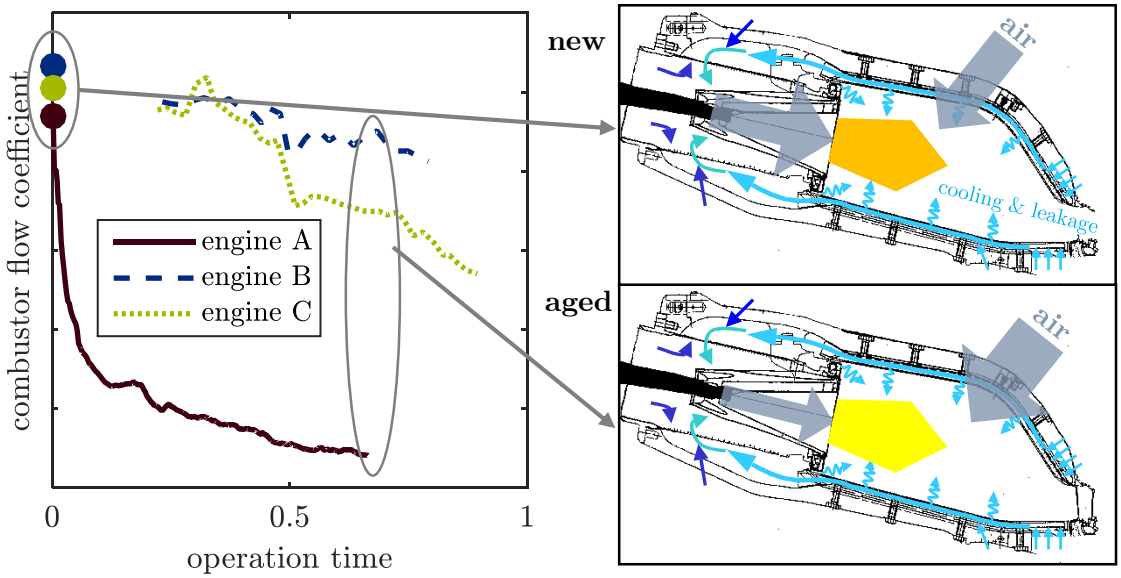

Figure 3.19.: Schematic aging model for decrease of combustor discharge coefficient. Scales not shown due to confidentiality.
Figure partially reprinted from Lipperheide et al. [76, 80].

In order to compare different load levels, the measured static pressure drop Δp_{EV} has to be transformed to a discharge coefficient ζ (with density ρ_{ref} and velocity v_{ref}; reference at compressor outlet) [108] and smoothed by a moving average filter[11]. The general defitinion of a flow coefficient is given in Eq. 3.29):

$$\zeta = \frac{\Delta p \cdot 2}{\rho_{\mathrm{ref}} \cdot v_{\mathrm{ref}}^2} \tag{3.29}$$

From this global point of view the thermally-induced pressure drop and/or dynamic pressure showed only minor influences on the pressure measurement in the specific EV combustor, therefore these two phenomena were no subject of further investigation.

[11] A moving average filter calculates the arithmetic mean $\zeta_{\mathrm{m(t)}}$ at a timestep t of n previous data points with $\bar{\zeta(t)} = \frac{1}{n}\sum_{i=0}^{n}\zeta(t-i)$

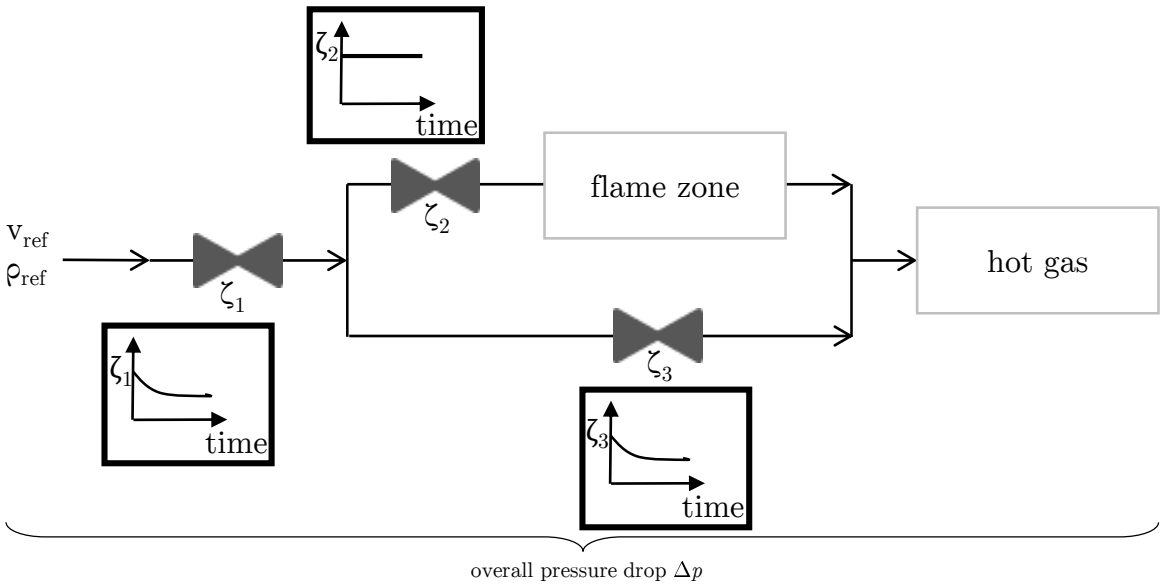

Figure 3.20.: Simplified air distribution model of EV combustor.
Figure reprinted from Lipperheide et al. [76, 80].

A simplified network model of the air flow system in the combustion chamber was then used to correlate the change of air flow distribution to the decrease of the overall pressure drop, i.e. the change of the total flow coefficient. This model had been derived from a detailed geometry-based design model by lumping the various main flow, cooling and leakage paths into an overall network.

In order to allow for determining all its parameters by the measured long-term data, this network was kept simple. The architecture shown in Fig. 3.20 preserves the main characteristics of the aging combustion chamber while limiting the amount of parameters in such a manner that its values can be identified from the data and one assumption on the flow distribution.

The simplified combustor model (Fig. 3.20) showed good agreement with an GE-internal geometry-based design model for air flow distribution in the combustion chamber. Additionally, the detailed information about the flow from the design model was used to derive the value of the discharge coefficient ζ (Eq. 3.29) under new and non-aged conditions.
With ongoing operation and aging, the measured overall discharge coefficient (Eq. 3.29) deviates from the design point. Different parts of the combustor (or discharge coefficients as their equivalents in flow models) can age in a different manner, leaving the network mathematically underdetermined. The difference between design discharge coefficient and time-variant actual discharge coefficient derived from measurements therefore had

to be distributed to the different discharge coefficients by the following assumptions: The main flow path of combustion air (ζ_2 , burner/flame zone) were assumed to show no aging effects, as reported during visual checks of the combustor during inspection. The split (X_{NOx}) (see Eq. 3.32) between pressure drop change in the inlet (ζ_1) and the combustor (equivalent resistance of ζ_2 and ζ_3) was thus assumed to be constant for the observed time period. In order to adapt for specific engine behavior, the value of X_{NOx} was identified as a constant parameter from the commercial operation data for an optimum match between prediction and measurement for the given gas turbine while $X_{\mathrm{NOx}} = 1$ would estimate all aging to the discharge coefficient ζ_1 which would accordingly relate to no change in cooling air distribution. The mathematical formulation of the network as the combination of the different flow coefficients, each given by Eq. 3.29,

$$\zeta_{\mathrm{total}} = \zeta_1 + \left(\frac{\zeta_{2,\mathrm{design}} \cdot \zeta_3}{\zeta_{2,\mathrm{design}} + \zeta_3} \right)^2 \tag{3.30}$$

eventually gives an analytic description of the adapted flow coefficient ζ_3 as a function of constant flow coefficient ζ_2, aging split X_{NOx}, design discharge coefficient and the total flow coefficient ζ_{total} that was calculated from the continuous operation data and is changing with ongoing operation by aging. Solving Eq. 3.30 for ζ_3 yields:

$$\zeta_3 = \left(\frac{1}{\sqrt{(1 - X_{\mathrm{NOx}}) \cdot \zeta_{\mathrm{total}} - \zeta_{1,\mathrm{design}} + X_{\mathrm{NOx}} \cdot \zeta_{\mathrm{total,design}}}} - \frac{1}{\sqrt{\zeta_{2,\mathrm{design}}}} \right)^{-2} \tag{3.31}$$

with

$$X_{\mathrm{NOx}} = \frac{\zeta_{1,\mathrm{design}} - \zeta_1}{\zeta_{\mathrm{total,design}} - \zeta_{\mathrm{total}}} = const. \tag{3.32}$$

As the air distribution is then given in the combustion chamber, it was possible to determine the flame zone temperature T_{flame} (see Fig. 3.20) from the previously derived hot gas temperature. In order to do so, the enthalpy flow of the cooling air h_{cooling} at compressor outlet temperature $T_{\mathrm{comp,out}}$ was subtracted from the hot gas temperature h_{hotgas}. For engine A the NASA polynoms were used as an analytic formulation of the enthalpy of the exhaust gas, whose composition was obtained by the assumption of complete combustion. Since the transmission of fuel flow data is frequently missing for engines B and C, constant heat capacities had to be assumed instead. This assumption further simplifies the calculation to the mass weighted mixing law. The computationally expensive recursive calculation of a temperature from a given enthalpy for engine A was

further avoided by setting the averaged heat capacity of the flame zone equal to the averaged one of the hot gas:

$$h_{\text{flame}} = h_{\text{hotgas}} \cdot \left(1 + \frac{\zeta_2}{\zeta_3}\right) + h_{\text{cooling}} \cdot \frac{\zeta_2}{\zeta_3}. \tag{3.33}$$

$$T_{\text{flame}} = \frac{h_{\text{flame}}}{\frac{h_{\text{hotgas}}}{T_{\text{hotgas}} + T_{\text{ref}}}} + T_{\text{ref}} \tag{3.34}$$

The influence of the change in pressure drop was thus related to an increase in flame hot gas temperature by adapting the share of the secondary cooling air flow.

3.3.4.3. Turboset Aging

When gas turbine aging in industrial applications is reported in literature (see Sec. 2) and industrial applications, deterioration of the turboset (compressor and turbine) is often mentioned as the main root cause, especially when power output and efficiency is investigated. Even though this work focuses on the emission progression, the influence of turboset aging on the chosen method had still to be estimated and considered.
The following section discusses turboset aging influences, separated into compressor and turbine, on NOx and CO emissions for the respective combustors. While compressor influences could be neglected a-priori by the structure of the model for reasons given in the next section, turbine aging may have an influence on the hot gas mapping. Thus, a step-by-step approach is presented to evaluate the influence of turbine aging, as later examined in the results part Sec. 4.2.2.

Compressor Aging A common aging phenomenon in compressors is fouling [51], caused by particle deposition in the compressor despite the efforts taken to filter the intake air. Particle deposition in the compressor eventually results in a deteriorated flow pattern and thus decreasing compressor efficiency and mass flow at the same time [109, 110]. Compressor aging is recoverable to a certain extent by (online-) washing, which clears the deposition, reduces the number of particles in the compressor and regains compressor efficiency. As the compressor needs more than 50% of the power generated by the turbine on the same shaft, those changes in the compressor characteristics can be detected by power output loss of the entire engine. As indicating parameters for compressor efficiency assessment (compressor in- and outlet pressures and temperatures) are measured during gas turbine operation, it can easily be linked with observed power

output loss.
All models (simplified engine model, emission and aging) were aimed to be built independently from parameters influenced by compressor aging, as for example intake mass flows and power output. The possible influence of compressor aging on the specific emission prediction models will be evaluated in the following.

NOx emissions EV NOx emissions prediction turned out to be a function of solely combustor pressure and combustor temperature with satisfying accuracy. As the combustor temperature was assessed by the turbine mapping approach[12], air mass flow is not needed for an energy balance. Merely the recalculation of a flame temperature from the hot gas temperature utilizes the cooling air split, which in return is calculated from the change of mass-flow based discharge coefficients. Cooling air distribution may also be changed by different pressure gradient in the compressor, considered as a secondary or tertiary effect within the general accuracy and thus neglected in the following investigations. Residence time of gas in the EV burner is included implicitly in the model by the pre-exponential factor $c\_NOx_{0,\mathrm{EV}}$. The factor was estimated to be constant for the given swirl-stabilized flame over the examined load range, so that NOx prediction is merely independent from compressor characteristics in the model presented (see Sec. 3.3.2).

NOx emissions SEV Again, the NOx formation in the second combustor is dependent on pressure and temperature only. With the given assumption of a choked flow through the LPT turbine, no influence of mass flow and compressor characteristics on residence time was expected. The cooling air distribution was seen to be determined by geometry only.

CO emissions As CO emissions are affected by combustion in the second combustor (SEV), characteristic volumetric flows may also be seen as constant, assuming choked flow and thus independence from mass-flow.
Once again, the calculation of the hot gas temperature was carried out by the mapping approach and therefore is independent from compressor parameters, which could potentially change through compressor aging.

[12] as a reminder: the turbine mapping approach reconstructs unmeasured hot gas temperatures by the use of component models, i.e. mapping of the turbines, and measured parameters as inputs to the mappings (see Sec. 3.3.1)

Turbine aging Turbine aging is reported to be less prominent in gas turbine operation with light fuels [50]. Yet, it can be detected by power output loss, as suitable parameters for a direct assessment of turbine efficiency are not commonly available in standard gas turbine operation: While inlet and outlet pressures of the turbine are measured, only outlet temperature can directly be detected, as the turbine inlet temperature measurement would require advanced technologies for challenging high-temperature conditions. However, model supported approaches exist (i.e. the use of the ISO inlet temperature) and root causes for turbine aging are also identified, as for example the increase in tip-clearance [111]. When the gap between the blade tip and the casing widens, leakage flow is increased and turbine efficiency and thus power output drops.

Hot Gas Temperature Mapping While hot gas temperatures could be modeled almost independently of compressor mass flow, they may be influenced by turbine aging because the hot gas mapping implicitly includes the polytropic efficiency, which is prone to turbine aging. Thus, uncertainty is added to the method by the hot gas temperature assessments. This topic will be discussed in the following.

Consideration of Turbine Aging Since turboset parameters, which may potentially age as well, could not be avoided completely in the modeling, a detailed evaluation was carried out for a possible case of superposed combustor and turbine aging. First, it is important to understand possible effects of lower turbine efficiency on the hot gas calculation: Given a full load point, a decreased polytropic efficiency would hypothetically lead to lower turbine inlet temperatures for controlled turbine outlet temperatures and a constant pressure ratio (in reality, inlet pressure would even decrease with lower inlet temperatures under choked flow conditions). Still, measured NOx emissions tend to increase with operation time. The NOx characteristics would thus be contradictory to the turbine aging hypothesis. However, the hypothesis of turbine aging could not be discarded, since for both, NOx and CO prediction, an aging-specific parameter had to be introduced to solve the under-determination of the model. As this parameter was adapted during long-term operation, it might have overcompensated unseen trends in hot gas temperature evolution. In the case of NOx prediction, the aging factor X_{NOx} would turn out to be smaller in the presence of turbine aging, since a decrease in hot gas temperature would be compensated by an increase in the difference between hot gas and flame temperature. For CO emissions, the aging factor X_{CO} would also decrease, thus expecting a lower influence of actual cold gas break-ins instead of cold air streaks.

This hypothesis was investigated by a sensitivity analysis for NOx formation:

1. Polytropic efficiencies for both turbines, HPT and LPT, were taken from design data
2. Hot gas temperatures as a function of pressure ratio and polytropic efficiency and corresponding flame temperatures for aged combustor ($\approx 40\%$ discharge flow coefficient drop, assumed $X_{\mathrm{NOx}} = 0.99$) were calculated
3. The calculated flame temperature served as input to the NOx model and yields a NOx formation
4. NOx emission was recalculated by steps 1-3 with decreased polytropic efficiency
5. Aging factor X_{NOx} was adapted to equalize resulting NOx emissions from 3 and 4.

Similarly, the potential influence of consideration of turbine aging on the aging factor X_{CO} was calculated and will be presented in 4.2.2.

3.3.5. Parameters for Modeling Approach

The entire model approach under consideration of emission, aging and engine performance only relies on a few control parameters of the gas turbine (see Tab. 3.5). These parameters from engine control and monitoring either serve directly as an input to the emission and aging models or are pre-processed by the engine model. The aging factors for NOx and CO are incorporated in the model approach as state variables.

Table 3.5.: Parameters in NOx and CO model

		NOx model	CO model
$T_{\mathrm{HPT,out}}$	measurement	X	X
	shift	X	X
	spread		X
$T_{\mathrm{LPT,out}}$		X	X
VIGV		X	X
$T_{\mathrm{comp,out}}$		X	
$m_{fuel,EV}$		X	
$p_{\mathrm{comp,out}}$		X	
Δp_{EV}		X	
p_{SEV}		X	X
p_{amb}		X	X
H_{amb}		X	X
T_{amb}		X	
C_{2+}			X
Aging factor NOx		X	
Aging factor CO			X

3.4. Model Application

In order to identify the root causes for aging, the aging and emission models had to be combined in a specific manner. Different scenario cases for NOx and CO prediction were tested, considering their main aging phenomena separately. The previously formulated emission models thereby quantify the impact of an aging phenomenon when emission progression for an isolated aging phenomenon is compared to the total measured emission progression from available long-term data. Fig. 3.21 illustrates the idea of the isolated aging model use. When an aging model is intentionally left out from the total data processing in the benchmark case, the emission prediction is expected to differ from the measurements by the value of emission progression. With this approach, the aging case may then also quantify the respective emission progression for the left-out aging phenomena, which is equal to the difference between incomplete prediction and measurement.

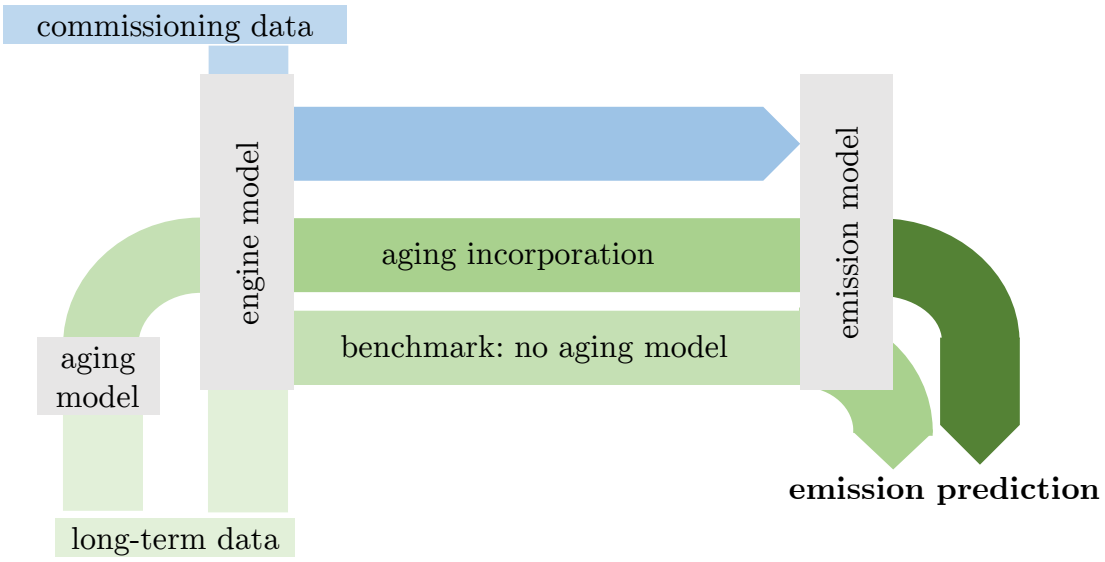

Figure 3.21.: Schematic illustration of model application for aging quantification. The benchmark case predicts hypothetical long-term emissions without aging; the aging case models emission prediction.

3.4.1. Fleet Aging

Since the limited number of three engines used for the detailed model identification is not sufficient to establish a distinct correlation between aging and operation regime (i.e. flexible vs. continuous operation), a broader statistical basis, i.e. a larger part of GE's GT24/GT26 fleet from the fleet data set (Sec. 3.2.4), was necessary. Within this fleet, different engines are operated in different markets, resulting in significant variations of the operation regime. For example, base load engines run for a high number of operation hours but only a few starts per year, whereas cycling or peaking units feature daily start-stop cycles with a very limited amount of operation hours. The existence of different operation regimes within the fleet enables to quantify the impact of flexible gas turbine operation on gas turbine aging: Number of starts was chosen as a measure for flexibility, as they increase thermo-mechanical stress in the engine and are already widely used in the calculation of equivalent operating hours in the industry (see Sec. 2.2). The drift of the high pressure turbine outlet temperature $T_{\mathrm{HPT,out}}$ (see Sec. 3.3.4.1) was thereby considered a useful measure for gas turbine aging, as it directly results in undesired emission progression. This phenomenon is at least partially caused by an actual aging effect, i.e. the increasing leakages (see Sec. 3.3.4.1), and reliably detectable by the $T_{\mathrm{HPT,out}}$ - measurement drift (see Sec. 3.3.4.1).

3.4.1.1. Detection of Inspection Interval

Operation hours and starts are counted continuously during the entire lifetime of the engine. Large inspections after $\sim$ 30,000 equivalent operation hours however, re-establish the initial and non-aged state of the engine. Since inspection intervals are not recorded in the long-term operation data set, they had to be identified from the data itself. The respective procedure is illustrated in Fig. 3.22, depicting the evolution of the turbine outlet temperature measurement deviation over gas turbine lifetime with an inspection event in 2015, where the initial state could be restored.

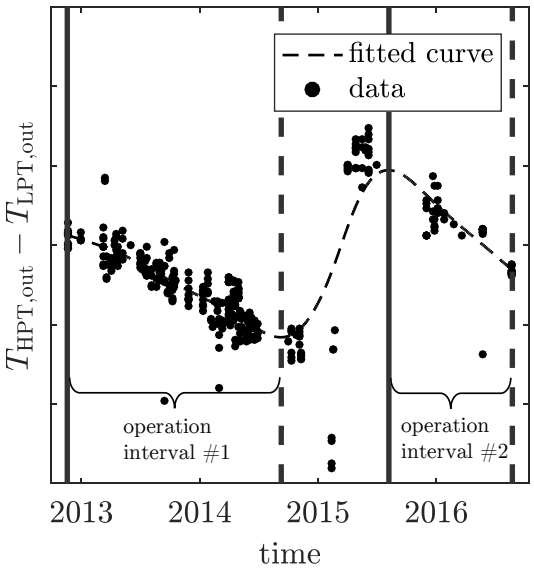

Figure 3.22.: Detection method of service intervals in long-term data.

By the means of a smoothed function (dashed line) of the scattered indicator for the measurement drift, peak values were identified and associated to the event of an inspection that re-establishes the initial state without aging. The entire data record time for each engine was thus divided into intervals from a maximum to a minimum, which correspond to one detected inspection interval each. For the entire interval, the $T_{\mathrm{HPT,out}}$ measurement drift for this investigation could thus be calculated as the difference between the functional value of a maximum point to its corresponding value of the subsequent minimum point. This method however, only provides one average value for the measurement drift over an entire inspection interval. Additional investigations have shown that some engines change their operation regime between seasons. However, available data quality and the temporal distribution of suitable sequential turbine outlet temperature measurements for drift detection did not allow for a more detailed resolution of such operational seasonal 'subperiods' with sufficient precision.

3.4.1.2. Data Set Quality

Fig. 3.23a depicts the distribution of the 25 engines with respective inspection intervals, marked by one star/dot each, according to their operation regime. Obviously, the fleet data set features independent variations of engine starts and operation time, which is obviously necessary for this investigation. If starts and operation hours were strongly correlated, a clear identification of flexible operation on aging would not be possible, since aging could either be a function of operation hours or starts.

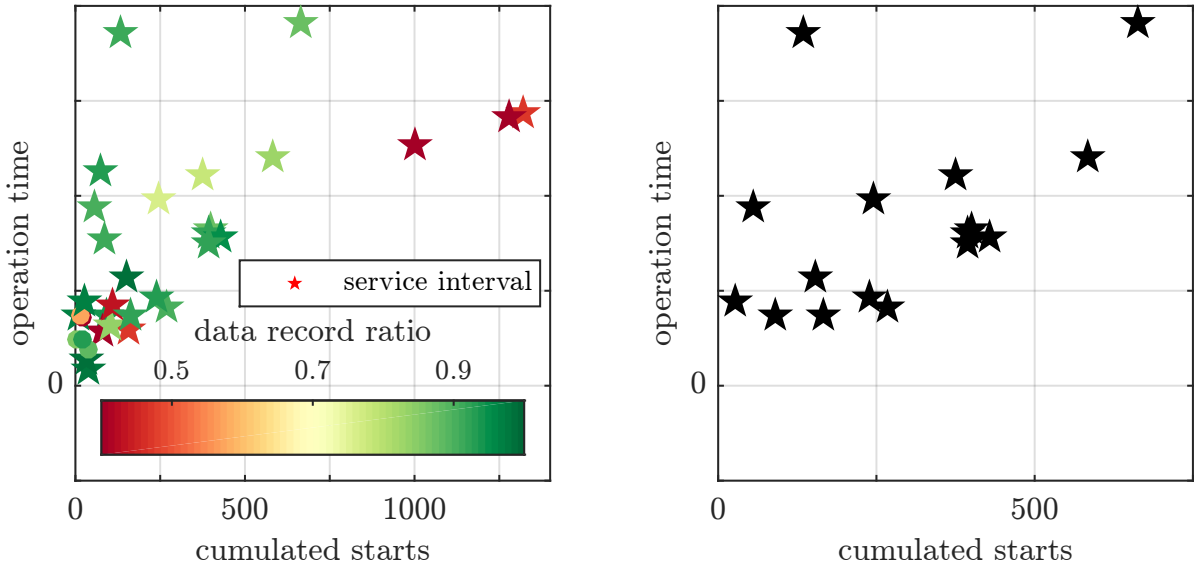

(a) Fleet investigation on (partial) independence of starts and operating hours

(b) Remaining data points after filtering: Cumulated starts vs. operation time

Figure 3.23.: Fleet investigation on (partial) independence of starts and operating hours. Round points indicate intervals disregarded to insufficient overall time periods or absolute number of data. Scales not shown due to confidentiality.

Nevertheless, there are several engines with similar operation time between two inspections, but a differing number of engine starts in for the same time period. This distribution thus enables an isolated investigation of engine starts as a measure for the impact of flexible operation on aging. However, some of the investigated operation intervals lack consistent and sufficiently frequent observations. The 'density' of available data was quantified through a data record ratio, which is defined as ratio between the time span with an active data acquisition system and the total time period in the corresponding operation interval. Infrequent data logging leads to a less reliable investigation,

since parameters had to be interpolated for the unrecorded time and the smoothing, as shown in Fig. 3.22, had to bridge large gaps. For very large gaps and insufficient data, the method might then even miss inspection intervals. Thus, intervals with infrequent data records (data record ratio less than 50%) were discarded from the investigation, because of an unsatisfying amount of total temperature drift data, or a short total time period. Additionally, inspection intervals with a total detected temperature drift below a threshold, which was expected to be the accuracy of the detection method, were discarded from the investigation. Finally, 16 inspection intervals remained for further investigations (see Fig.3.23b)). Although the cleaning of the data set removed some variance from the data set, the distribution of the remaining engines was still considered to be valid for the assessment (see Fig.3.23b)).
A similar study was conducted with the second aging indicator for the EV combustor. The combustor flow coefficient was extracted from fleet data for each inspection interval of the respective engine. After deleting irrelevant data and dismissing periods of infrequent data record, the data basis did not allow for a further investigation, as operation hours and starts were correlated in the data set.

3.4.1.3. Indicator Selection

In order to extract the desired information from the fleet data, the right indicators/parameters used for evaluating flexible operation and aging had to be chosen. Cumulated engine starts have been identified as an appropriate indicator for flexible operation, while aging is well represented by the $T_{\mathrm{HPT,out}}$ drift. Further, the indicator for lifetime i.e. the operation hours as a third variable, must also be displayed to check for a spurious correlation. Since the absolute number of starts and $T_{\mathrm{HPT,out}}$ drift are expected to increase with operation time, only an uncoupled variation of operation time and number of engine starts allows for an isolated identification of the aging impact by cyclic operation. A normalization of aging phenomena to operation time would seem to be an obvious method to include lifetime as a third variable. This normalization would, however, overestimate the influence of inspection interval duration against the actual aging phenomenon by the reciprocal nature of the normalization.

3.5. Statistics

Statistical methods in this context cover validation metrics as well as a benchmark method for data-driven prediction and a probability-based alternative to the Monte-Carlo method for uncertainty assessment.

3.5.1. Validation Metrics

Long-term emission prediction results were compared to measured data by using the root mean square error (RMSE) in favor of, for example, the coefficient of determination, as the RMSE provides a measure of model quality in the actual unit (ppm for emissions), and because it is applicable to the present non-linear regression without any adaptions. The RMSE is defined as

$$RMSE_{\mathrm{NOx}} = \sqrt{\frac{\sum_{t=1}^{n} \left(c\_NOx_{\mathrm{p}}(t) - c\_NOx_{\mathrm{m}}(t)\right)^2}{n}} \tag{3.35}$$

$$RMSE_{\mathrm{CO}} = \sqrt{\frac{\sum_{t=1}^{n} (\log_{10}(c\_\mathrm{CO}_{\mathrm{p}}(t) - \log_{10}(c\_\mathrm{CO}_{\mathrm{m}}(t)))^2}{n}} \tag{3.36}$$

where n is equal to the number of data points (Tab. 3.2), $[]_{\mathrm{m}}$ denotes measured values and $[]_{\mathrm{p}}$ denotes predicted values.

The relative root mean squared error (rRMSE) was used to evaluate the accuracy of the model identification from commissioning data in order to make the model comparable for different engines with possible different overall emission ($[]_{\mathrm{e}}$) levels. It is defined as the RMSE divided by the mean (denoted by the overbar) of all measured values

$$rRMSE = \frac{1}{\overline{c_{\mathrm{e,m}}}} \cdot \sqrt{\frac{\sum_{t=1}^{n} \left(c_{\mathrm{e,p}}(t) - c_{\mathrm{e,m}}(t)\right)^2}{n}} \tag{3.37}$$

Another meaningful value for model quality assessment is the residual between predicted and measured value:

$$Residuals = \log_{10}(c_{\mathrm{e,m}}(t)) - \log_{10}(c_{\mathrm{e,p}}(t)) \tag{3.38}$$

Residuals are displayed in their logarithmic form for simultaneous scaling and referencing to the measured value. This approach was chosen, since a sole referencing to the measured value would overrate errors at low emissions. With the definition given,

positive residuals mean a higher actual measured emission value than its predicted equivalent.

Scatter plots as the most commonly used graphical presentation in the result chapter contribute to the validation as a visual tool, which allowed for the detection of single outliers and distribution of residuals.

3.5.2. Uncertainty and Sensitivity

An uncertainty analysis was performed in this work in order to evaluate inevitable uncertainty contributions of input parameters to the model, beside model-own inaccuracies. The sensitivity analysis, which is closely related to the uncertainty, was then used to examine the influence of improvements in input parameter accuracy on overall model quality. It can be interpreted as the benefit, which an increased accuracy of a single measurement would give to overall model performance.

3.5.2.1. Polynomial Chaos Expansion

The Polynomial Chaos Expansion (PCE) (see C.1) as a very computational cost-effective alternative to the Monte-Carlo-Method is able to define the variance of output parameters of a model with uncertain input parameters. In contrast to the Monte-Carlo-Method, where output parameters have to be calculated for a large number of varying input parameter within their accuracy limits, the PCE features an analytic approach, first developed by Wiener in the late 1930's [112]. The PCE transforms the actual and maybe complex model, which shall be object to the uncertainty analysis, into a metamodel. This metamodel is mathematically structured in a way, that allows for fast assessment of the two main statistical moments, 'expectation value' and 'variance' for a given input parameter distribution. As only few runs of the actual model suffice to build the metamodel, this approach is very advantageous over the standard Monte-Carlo-Method, which would need many runs of the model to obtain a high resolution output distribution. Stefano Marelli and Bruno Sudret [113] developed and published a powerful PCE tool for Matlab which was used in the course of this research. Basic ideas and mathematical transformations are explained in the appendix to raise a basic understanding of the method and its use for uncertainty quantification. An extension of the method features sensitivity analysis by the calculation of 'Sobol Indices', a first-order sensitivity index, that is a measure for the contribution of one parameter to the total

output variance over variation in all other parameters, ranging from 0=no contribution to 1=entire contribution [114].

3.5.2.2. Application to Emission Prediction

In the current research, PCE was used to determine the uncertainty and sensitivity of NOx and CO emission prediction. The entire model, including the analytic emission models and the simplified engine model, could be transformed to a PCE formulation with only few input parameters, which are pressure, VIGV, turbine outlet temperatures, compressor outlet temperature and ambient conditions (pressure, temperature, humidity) and mass fuel flow (see table 3.5). For a set of parameters (corresponding to defined load point[13]), a Polynomial Chaos Expansion was carried out with Gaussian distribution for each of the input variables around its expectation value and variance taken from data sheets and/or expert evaluation.

Variances of these processed parameters as an input to the PCE method were derived from sensor calibration or expert evaluation. For p_{amb}, total sensor performance and long term stability were evaluated to a standard deviation of $\sigma = 0.0005$ bar; the accuracy of a pressure sensor used for gas path measurements were estimated to $\sigma = 0.04$ Pa for compressor outlet and the respective fraction for Δp_{EV} and p_{SEV} in long-term operation[14]. While uncertainties in pressure measurements could be set by information from manufacturers, accuracies of temperature measurements were more difficult to define: As already mentioned in this work and known from literature, hot gas temperature measurements in gas turbines tend to deviate by many indeterminable influences (i.e. leakage streaks, sensor drifts), which are themselves subject to indeterminable uncertainties by aging. Thus, standard deviations in temperature measurements, especially turbine outlet temperature measurements, are solid expert evaluations in accordance with absolute deviations, as previously detected and investigated in this work. The same applies to variance in fuel measurements, which were estimated to be below 5% for the mass flow and below 0.02 percentage points for the C_{2+} content.
Aging factors are neither subject to uncertainty nor to sensitivity, as they are, despite being processed in the model, no input parameters by definition but rather state vari-

[13]Definition of load points by $T_{\mathrm{HPT,out}}$, $T_{\mathrm{LPT,out}}$, VIGV and ambiance only. Pressures for these setups are then derived from the simplified engine model as a surrogate to actual measurements

[14]Assumptions: upper range limit for gas turbine pressure sensor = 55 bar, measurement span = maximum respective combustor pressure [115]; Standard deviation of ambient pressure sensor for overall performance and long-term stability = 32.5 Pa, variance of ambient temperature measurement equal to 0.05 K, variance of relative humidity 1% [116]

ables in the model.
Load points for uncertainty calculations concerning the NOx emissions were distributed over the entire full load and part load range, according to a hypothetic OPC (see Fig. 3.5), CO is only investigated in low load points by varying $T_{\mathrm{HPT,out}}$ at small VIGV openings.

3.5.3. Machine Learning Tools

As a comparison to the semi-empirical model, emission prediction by Artifical Neural Networks (ANN) (further explanations in Appendix D) was tested.

Amongst many available data methods, ANNs were chosen, because they are reported to have successfully modeled gas turbines in the past [117, 118, 119, 120, 121, 122, 123]. The exact same approach as for the physically-based modeling was used with parameter identification, i.e. training for ANNs, on commissioning data and validation with long-term data. Thus, a certain capability of extrapolation was demanded by the neural network method, too.

From the commissioning data set, different data subsets were tested (see Tab. 3.6). First, the 'raw' data set (data subset 'NOx' and 'CO') includes solely raw measurements, which previously served as inputs to determine the engine state by physical modeling.

Table 3.6.: Parameters in data subsets used for Artificial Neural Network (ANN)

	NOx	$\mathrm{NOx_{flame}}$	$\mathrm{NOx_{flame+amb}}$	CO	$\mathrm{CO_{flame}}$
dataset	raw	virtual	virtual+amb	raw	virtual
$T_{\mathrm{comp,out}}$	X				
$p_{\mathrm{comp,out}}$	X	X	X		
VIGV	X	X	X	X	X
$\mathrm{p_{SEV}}$	X	X	X	X	X
$T_{\mathrm{HPT,out}}$	X			X	X
$T_{\mathrm{LPT,out}}$	X			X	
$\mathrm{p_{amb}}$	X		X	X	
$\mathrm{H_{amb}}$			X	X	X
$\mathrm{T_{amb}}$			X		
$\mathrm{C_{2+}}$				X	X
SEV on/off	X	X	X		
$\mathrm{T_{flame,EV}}$		X	X		
$\mathrm{T_{flame,SEV}}$		X	X		X

Merely ambient and thus possibly correlated measurements were intentionally left out whenever possible, since their insufficient variation in the commissioning data set could easily cause over-training of the network. Second, data subsets with processed measurements were created (data subsets '$\mathrm{NOx_{flame}}$' and '$\mathrm{CO_{flame}}$'): From the simplified engine model used in Sec. 3.3.1, the EV flame temperature and SEV hot gas temperature were derived in order to replace the respective turbine outlet temperatures ($T_{\mathrm{HPT,out}}$ and $T_{\mathrm{LPT,out}}$ for NOx, $T_{\mathrm{LPT,out}}$ only for CO) in these data sets. The ANN is thus only used for emission modeling while the engine model (mapping) is employed for raw data processing in this case. In case of NOx, two further investigations were carried out: The aging model and its direct link to the EV flame temperature allows for an easy integration of EV combustor aging to the neural network method. Training could still be done with commissioning data, only the EV flame temperature in the long-term data inputs (data subset '$\mathrm{NOx_{flame}}$') to the neural network had to be replaced by its aged equivalent. Further on, the virtual data-subset was also enriched by ambient measurements (ambient temperature, pressure and humidity) to investigate potential initial mismatches between training and validation data by external influences (data subset '$\mathrm{NOx_{flame+amb}}$').
Similar investigations were, however, not feasible for the CO model, as its structure does not allow for a simple aging incorporation from raw commissioning data: The CO aging model explicitly needs the partitioning of SEV combustion chamber segments into hot, medium and cold groups and its mathematical representation by a weighted addition. With the limited input data from commissioning, such a model could not be established in the framework of ANNs.
Input parameters to different subsets are summarized in Tab. 3.6.

As the neural network training and thus its composition is expected to vary with the data available for training (for details of ANNs, see Appendix D), the number of necessary neurons in the hidden layer was estimated a-priori for each data subset. Fig. 3.24 illustrates the necessary number of neurons in the hidden layer to achieve small errors in the training data set.

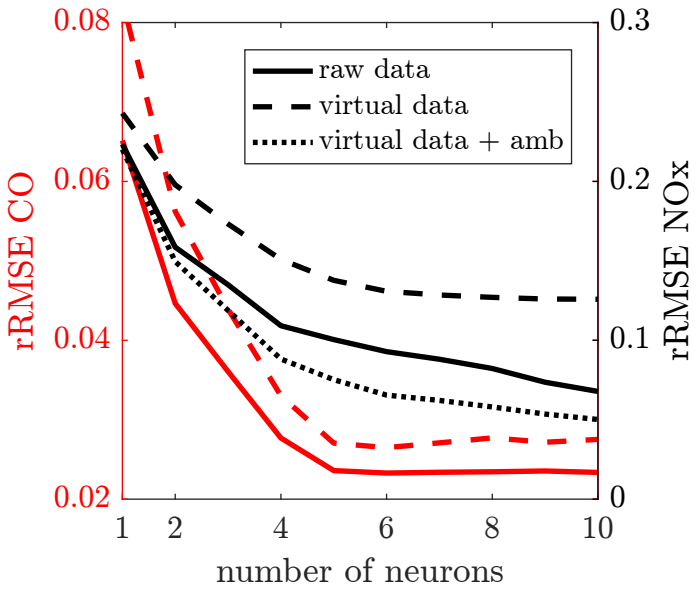

Figure 3.24.: Required number of neurons for different data sets.
20 different runs for each configuration, since ANN performance is dependent on initial parameter guess. Lines show the smoothed minimum achieved errors for respective number of neurons. Final results do not have to correspond necessarily to that minimum, as only one specific ANN with satisfying results in long-term data is shown. Figure reprinted from Lipperheide et al. [83].

When using the virtual data set with flame temperatures from the engine model, five neurons are sufficient to reach maximum accuracy (in terms of rRMSE) in the training data for both emissions investigated. When using raw data or virtual data enriched by ambient measurements, the higher number of parameters also demands more neurons to reach maximum accuracy. Thus, the number of neurons for further investigations were set to five for the following cases:

- NOx_{flame}
- CO_{flame}
- CO

and to ten neurons for:

- $NOx_{flame+amb}$
- NOx.

As an implementation of the above described methods, the Matlab Neural Network Toolbox [124] was used in this study. For the given case, Bayesian regularization was

chosen as an implementation of backpropagation training algorithm, since it promises good regularization even for small datasets, as they are existing for the purposes here. The Matlab Neural Networks Toolbox also features a cross-validation algorithm to potentially prevent the overtraining by an excess of neurons by simultaneously employing three different data sets while training: The actual training was done on the training data sets, which represents 70% of all commissioning data; the error in the validation data set (15%) of all data was simultaneously monitored to prevent overtraining and the remaining 15% were used for testing by default. Although this algorithm is designed to potentially prevent the overtraining by an excess of neurons, the necessary neurons were still estimated a-priori to prevent a potential source of errors in Sec. 3.5.3. Since inherent starting values and the split of data sets into training and validation are influenced by random initial guesses in this method by nature, exact results may vary for each run. Thus, results in the following chapter will be displayed for selected representative ANN, which correspond to the observed behavior of several test runs. Detailed explanation can be found in App. D.

4. Results

This chapter presents the results of the previously introduced modeling approaches. A large part covers the semi-empirical long-term emission modeling, which was also evaluated by the statistical methods presented in Sec. 3.5.2. Particular focus is given to the uncertainty impact of turbine aging. Results will be set in a wider context by comparing the results to the ANN benchmark method and by a discussion of the findings with respect to the fleet data.

4.1. Aging Quantification

By the use of different scenario cases, either incorporating the aging phenomena to long-term emission modeling or using a simplified engine model without consideration of aging, the impact of aging on respective emissions could be examined. Results will be presented separately by its phenomenon in the following.

4.1.1. NOx Emission Aging

As two discussed aging phenomena (air split and turbine outlet temperature drift) directly influence T_{flame} of the EV-burner, they also affect the NOx emissions prediction. Thus, the isolated incorporation of aging corrections for T_{flame} may quantify the impact of the discussed aging phenomena on NOx emissions. In order to do so, four different cases were examined for available long-term data.

Case $\mathbf{1_{NOx}}$: Both aging effects considered (turbine outlet temperature correction & air flow distribution adaption)

Case $\mathbf{2_{NOx}}$: One aging effect considered (turbine outlet temperature correction)

Case $\mathbf{3_{NOx}}$: One aging effect considered (air flow distribution adaption)

Case $\mathbf{4_{NOx}}$: No aging effects considered

Table 4.1.: Model validation on long-term operation data: RMSE for prediction of NOx emissions for examined engines and different cases (X_{NOx} optimized for case 1_{NOx})

RMSE	X_{NOx}	case 1_{NOx}	case 2_{NOx}	case 3_{NOx}	case 4_{NOx}	improvement
engine A	0.99	1.27	1.33	1.72	1.98	35%
engine B	0.00	1.84	2.64	3.37	3.97	53%
engine C	0.95	3.01	3.02	4.01	4.08	26%

When the NOx correlation was applied to long-term data, the incorporation of all aging phenomena (i.e. case 1_{NOx} scenario) yielded the best prediction performance for each of the investigated engines (Tab. 4.1). The parity plots for the case 1_{NOx} scenario in Fig. 4.1 show satisfying model performance over the investigated load range. The trend in NOx emission is reproduced within the accuracy associated with the CEMS.

A comparison between case 2_{NOx} and case 3_{NOx} allows for an evaluation of the two described aging phenomena against each other. It can be derived that incorporating the change in NOx emission by deteriorated turbine outlet temperature measurements (case 2_{NOx}) improved the accuracy of the prediction more than the sole integration of change of air flow distribution (case 3_{NOx}) for all investigated gas turbines.
This, in return, leads to the conclusion that the drift of turbine outlet temperature measurement has a higher impact on observed NOx emission progression over the combustor's lifetime for the investigated engines than the change in EV air flow distribution.

The model yielded different prediction accuracies for each engine (see Tab. 4.1). First, this is due to the different availability of commissioning data, which served as a training data set. Parameter identification is a major but inevitable source of inaccuracy, which relates to the differing commissioning data set for each engine. For example, engine B and C have worse relative RMSEs compared to engine A in the commissioning data. Additionally, a visual inspection of distribution of fitting data revealed, that the data sets lack an important commissioning run where SEV temperature varies for a constant EV temperature, even though more overall commissioning data points were available (Tab. 3.2). Generally, the commissioning procedures turned out to be disadvantageous for emission mappings, due to poor variations of driving emission parameters, even though providing a high absolute number of datapoints.

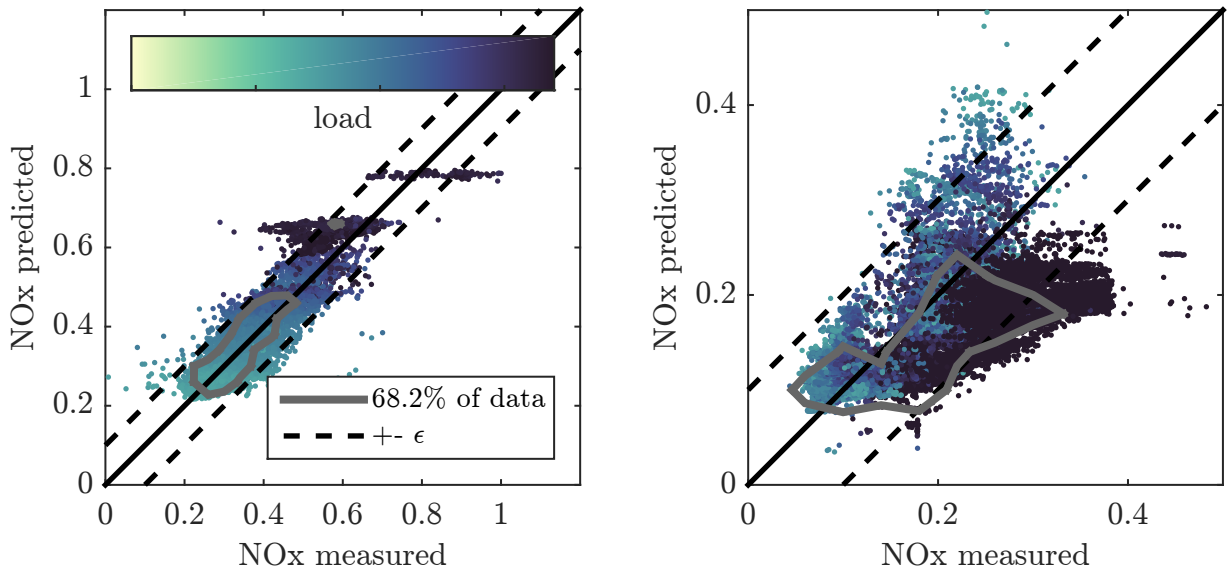

(a) Engine A

(b) Engine B

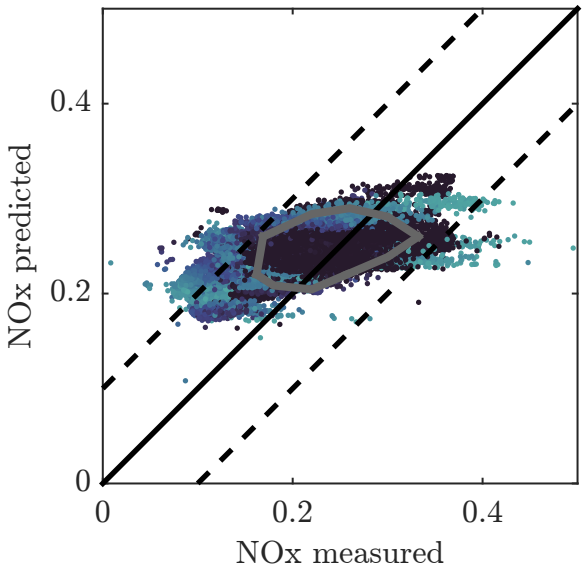

(c) Engine C

Figure 4.1.: Long-term performance of NOx prediction with aging incorporation (case 1_{NOx}) (only 20% of data are displayed). ϵ indicates the expected uncertainty of the measurement system. All scales are normalized to a reference value.
Figure reprinted from Lipperheide et al. [76, 80].

Second, the different optimum flow aging parameters represent engine-specific behavior, which may occur within the same gas turbine fleet because of assembly and production. Concerning gas turbine B, the aging of the flow coefficient had a greater impact on the change in emissions compared to engine A and C, as indicated by a lower

estimated parameter X. While engine A and C show only a slight share of flow coefficient decrease in the cooling air feed as X reaches towards one, engine B estimates a higher impact of feed air flow change by pressure drop.

Regarding engine A, its combustor flow coefficient obviously indicates faster and stronger aging than engine B & C (see Fig. 4.2), which would correspond to a higher aging parameter X (see Tab. 4.1) in case of comparable absolute aging of flow coefficient 3 according to Eq. 3.32. A closer look at the pressure drop measurement reveals that this apparent behavior is due to a single sensor fault. The pressure drop over the combustor is measured by two redundant differential pressure sensors between compressor outlet plenum and combustor exit. The parameter Δp_{EV} used in this study is the mean of both measurements. In the case of Engine A, the two measured pressure drops differed significantly, leading to different combustor flow coefficients when calculated separately.

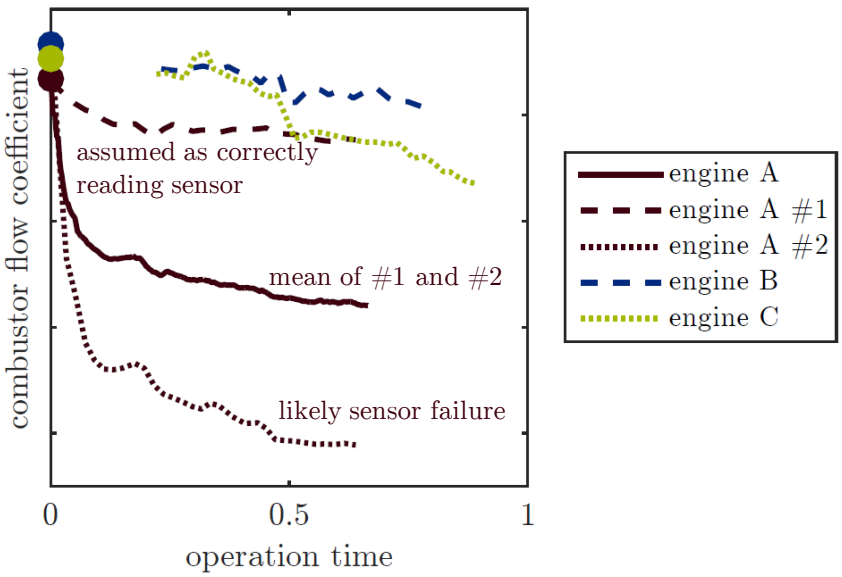

Figure 4.2.: Total combustor flow coefficients according to Eq. 3.29 for sensor fault detection of sensor # 2 in engine A. Redundant combustor flow coefficient based on pressure sensor reading # 1 for same engine A and engine B and C as comparison.
Figure reprinted from Lipperheide et al. [80].

A comparison among all flow coefficient evolutions in available fleet data reveals that sensor # 2 of engine A is completely out of the 'normal' degradation range (see Fig. 4.2) while sensor # 1 of the same engine A matches the behavior of engine B & C well. Thus, only sensor # 1 is regarded to be reliable. When using sensor # 1's pressure

measurement only for the above conducted investigation, the aging factor X_{NOx} would decrease to 0.97.

It is also worth noting, that an aging factor X_{NOx} in the range of $\approx 0.95 - 0.99$ still translates to a significant seal loss in valve 2, since the parallel architecture of the flow network, the absolute values of the valves and the definition of X_{NOx} favors high numerical X_{NOx} values.
However, optimized X_{NOx} may also include undesired effects. Since the flow network is underdetermined, the aging parameter had to be optimized during long-term operation, which made it prone to overcompensation of superimposed influences. Especially for engine B and C, estimations of X_{NOx} may be less reliable due to less frequent data for drift detection, a less prominent NOx progression in long-term operation and a partially correlated parameter identification data set. This might also explain the large difference in X_{NOx} values for engine B and C values which, however, does not have a great influence on overall NOx emission progression.

However, absolute residuals (depicted in Fig. 4.3) meander in all investigations. These meandering deviations are mainly caused by long periods of sole part load operation with a generally lower absolute NOx level. Increasing transient operation could also be a cause, which however could not be investigated with data sample resolution of five minutes. In addition, engine parameters for the aged engine may also be set in a range, which was originally not covered during commissioning and are thus outside of the validity of the previously established NOx-correlation. The reason of the prominent rise of residuals for engine B at approximately 0.5 of the operation time, similarly seen for engine C, could not be identified entirely by the available data. A manual and unreported re-adjustment of the temperature outlet measurement or a CEMS-calibration may be a cause for example. Expected secondary influences on NOx-formation like ambient temperature, fuel composition and relative humidity were investigated through partial residuals but have been found to be negligible.

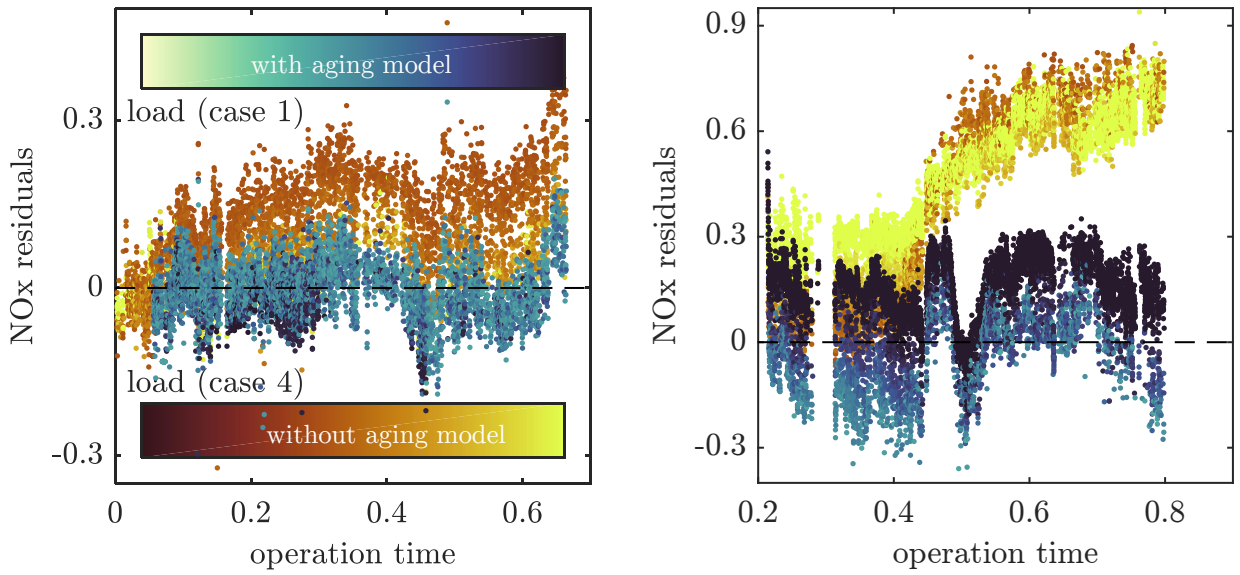

(a) Engine A

(b) Engine B

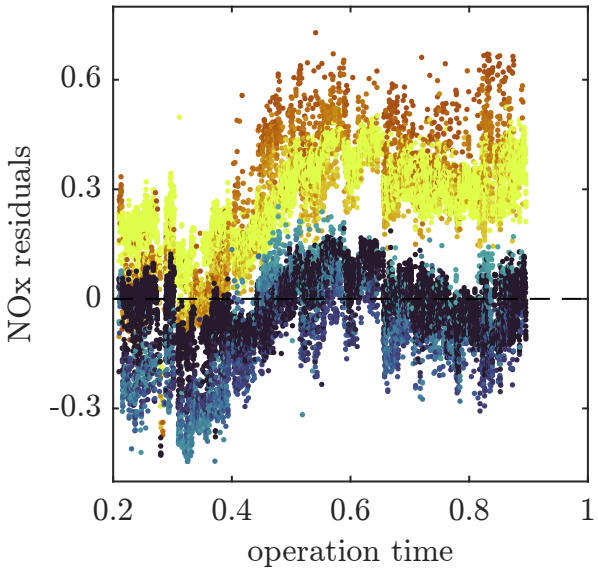

(c) Engine C

Figure 4.3.: Residuals of NOx prediction with aging incorporation (case 1_{NOx}) compared to standard prediction (case 4_{NOx}). Gray area indicates the 68.2% interval around mean value. All scales are normalized to a reference value.
Figure reprinted from Lipperheide et al. [76, 80].

4.1.2. CO Emission Aging

The combination of the CO model (Eq. 3.24) and the aging model for the combustor air distribution (Eq. 3.27) also allowed for a quantification of the aging influence on CO

emissions. In order to illustrate this influence, two cases are distinguished. Case 1_{CO} predicts CO emission over operation time when considering the evolution of cold and hot zones in the $T^{+}_{g,in}(t)$ temperature distribution. Case 2_{CO} only uses the average $T^{+}_{in,corr}(t)$ for all 24 burners during model identification and validation and therefore disregards aging of the temperature homogeneity.

Case 1_{CO}: Consideration of cold and hot zones in high pressure turbine outlet temperature

Case 2_{CO}: Mean high pressure turbine outlet temperature

Table 4.2.: Available long-term data and prediction model performance for different engines.

RMSE	X_{CO}	case 1_{CO}	case 2_{CO}	improvement	d
engine A	0.49	0.17	0.42	60 %	3
engine B	0.12	0.1	0.12	15%	3
engine C	0.31	0.08	0.2	58%	3

The parity plots (Fig.4.4) between the actual measured and the respective predicted CO emissions for case 1_{CO} display the best-achievable accuracy of each model. The comparison of the plots for case 1_{CO} vs. case 2_{CO} highlight the influence of aging on CO emission formation, which can be quantified by comparing the corresponding RMSE values (see Tab. 4.2).

Based on the metrics given in Tab. 4.2 and the residual distributions in Fig. 4.4, the best match between predicted and measured CO emission for all engines was obtained in case 1_{CO}, when aging models are incorporated.

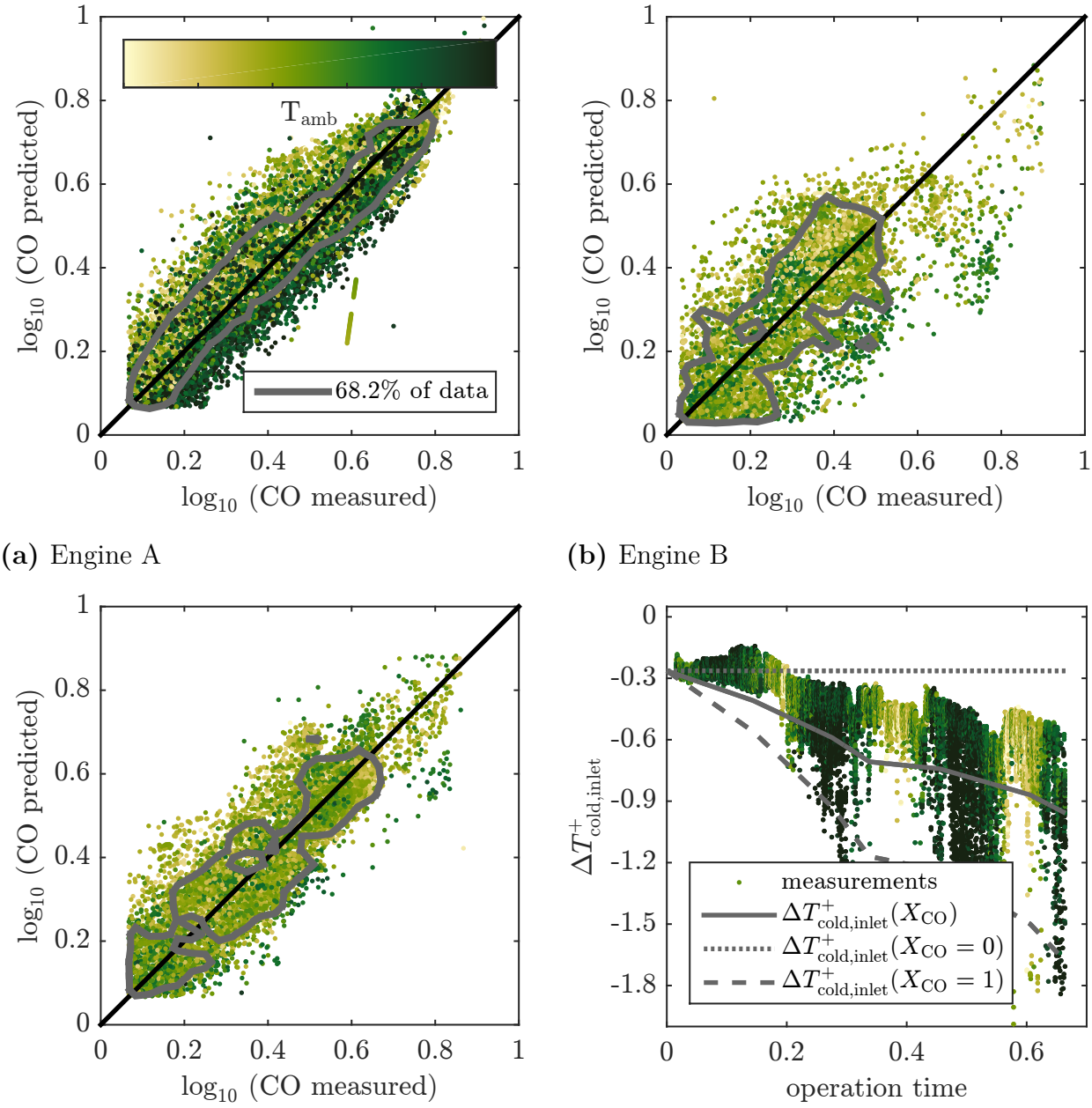

(a) Engine A **(b)** Engine B

(c) Engine C **(d)** Engine A

Figure 4.4.: Long-term performance of CO prediction with aging incorporation (case 1) and corresponding temperature deviation (only 20% of data are displayed[1]). All scales are normalized to a reference value.

However, the accuracy of the model and the impact of aging differs among the engines for several reasons. The RMSE of engine A was improved by 60% and the RMSE of engine C by 58% when incorporating aging. As engine B obviously ran more often at its nominal load than A and C, CO levels and thus their prediction error are generally lower. The aging effect was also less prominent (15%) for this specific engine, as illustrated

in the residual time series presented in Fig. 4.5,. Whereas engines A and C show a clear underprediction of CO emissions with increasing operation time ($\sim$ aging) in case 2_{CO} without modeling of aging effects, the residuals displayed for engine B are mostly overlayed to the ones that disregard aging phenomena. This is an indicator for a small CO aging effect, thus a negligible effect of actual cold gas break-ins at the high pressure turbine outlet.

As explained in Sec. 3.3.4.1, this small aging influence should also be expressed in the model by a very small aging factor X_{CO} in the range of zero. The method, however, calculated the factor X_{CO} to a non-zero value of 0.12. This adaption of the aging factor X_{CO} can be seen as an over-compensation, which does not reduce the prediction error introduced by aging significantly (see Tab. 4.2) but compensates for model inaccuracies in a non-physical way instead.

Fig. 4.5 also illustrates a secondary effect that leads to obvious residuals. In both cases (case 1_{CO} & case 2_{CO}), residuals appear to meander with seasonal changes in a way that CO emission is over-predicted in colder ambient conditions. For the case 2_{CO} scenario, this phenomenon is less evident, since seasonal influences are superimposed by aging (Fig. 4.4). The seasonal deviations can be explained by a change of the cooling air flow distribution that is not considered in the model. Low ambient temperatures induce changes in mass flow and thus pressure levels in the compressor stages, which then correlate with a lower pressure drop (see Fig. 4.5) in the cooling air flow system of the combustor. Provided that the geometry of the cooling channels is imposed by the installed hardware, this leads to a reduction of volumetric cooling flow and ultimately to a delayed quenching in the combustor. Thus, the time for CO oxidation is prolonged and real CO emissions decrease accordingly. This effect was clearly revealed by the results, but not quantified, since the measurement resolution and data basis was not sufficient for a desired semi-empirical approach.

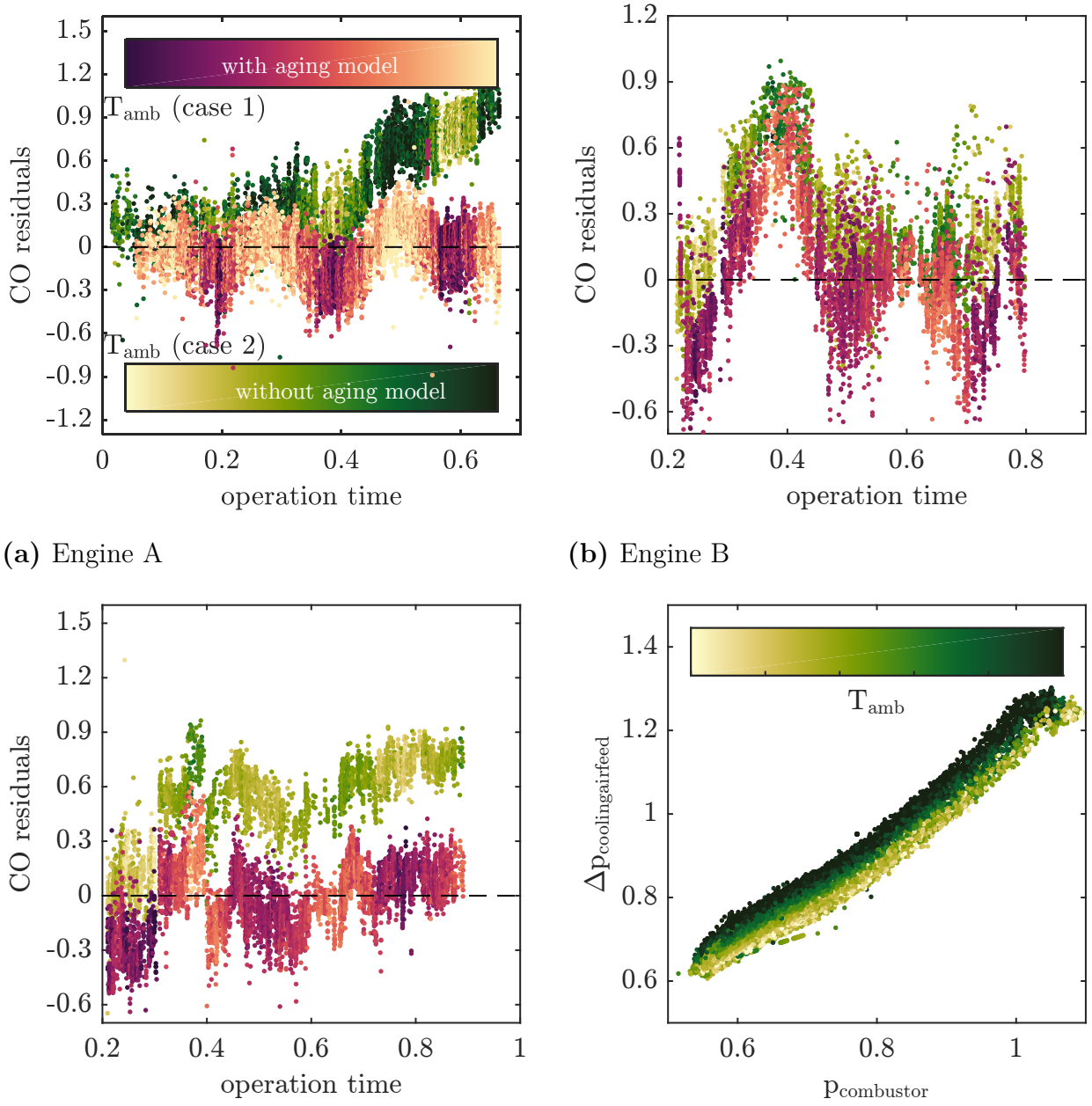

(a) Engine A

(b) Engine B

(c) Engine C

(d) Engine A

Figure 4.5.: CO residuals of prediction model over operation time and ambient temperature effect on cooling air flow (only 16.67% of data are displayed). All scales are normalized to a reference value.

4.2. Evaluation of Results

The evaluation compromises technical sources of errors in the emission measurement system as well as uncertainties introduced by the method itself, i.e. the hot gas assessment by the mapping approach and the general model structure.

4.2.1. Emission Measurement System

Besides all model-induced uncertainties in the variables, which are difficult to quantify, a second reliable emission measurement system during commissioning allowed for independent evaluation of the CEMS system (see Fig. 3.10d) and Fig. 3.13d)). It is worth noting, that the scattering in the CEMS system imposes an accuracy limit to the method and explains a great part of the scattering in the long-term prediction:
Concerning the NOx model, the major part of the remaining NOx residuals (see Fig. 4.1) lay within this range of accuracy of the legislative binding CEMS. In this particular case, the accuracy of the CEMS system thus imposes a limit to the maximum possible quality of the derived model. The CO scatter in long-term operation (see Fig. 4.4) can, however, not be explained solely by the uncertainty in the CEMS system. Although there is an inevitable scattering by the CEMS system (see Fig. 3.13d)) for CO measurements, its range is smaller than the actual residuals for long-term prediction, which is caused by the described T_{amb} influence and may also be affected by the five-minute averaging of the sampling.

4.2.2. Uncertainty Assessment of Turbine Aging

Despite the fact, that turbo set aging was not in the scope of this research, it might have had an influence on the results presented by model overcompensation, resulting in deviating aging factors (see chapter 3.3.4.3). While the influence of compressor aging on the emissions models could be shown to be negligible beforehand, turbine aging could neither be excluded in the model parameters, nor quantitatively evaluated due to the lack of determining measurements. Thus, an 'expert evaluation' had to be carried out to estimate the possible impact of the polytropic efficiency on hot gas temperature assessment and the determination of the aging factors accordingly: For an estimated loss in polytropic efficiency of 3% in high and low pressure turbine, the estimation of X_{NOx} would change from 0.99 to 0.92 to compensate the decrease of hot gas temperature by turbine aging for a representative high load point. Concerning the adaptable aging parameter X_{CO}, it would decrease from 0.5 to 0.44 for an hypothetical low load

point with considerably high CO emissions. At the same time, the estimated 3% loss of turbine efficiency would decrease the overall full load power of the GT power by about 6% (when assuming compressor power to $\approx 1/2$ of turbine power) and the SEV hot gas temperature by about 30 K for a given typical turbine outlet temperature. With the assumption of choked flow, a reduction of 30 K in turbine inlet temperature would result in a 0.3 bar pressure drop to preserve the constant volumetric flow at a given VIGV[2] position. Neither of these potentially remarkable changes can be detected from Fig. 4.6: The pressure at the low pressure turbine inlet remains constant for defined inlet guide vane positions. A power decrease can neither be detected in full load investigations (Fig. 4.6 b)) nor during start up of the combined cycle (Fig. 4.6 c)). Start up points even include GT-only operation (the lowest load points of each sequence), so that possible fluctuations from the steam cycle can be eliminated a-priori. The identification of constant power at EV-only operation over operation time also helps justifying the theory of the detected temperature-shift (see Fig. 3.16). The increase of temperature difference between $T_{\mathrm{HPT,out}}$ and $T_{\mathrm{LPT,out}}$ over operation time could also be caused theoretically by turbine aging: As EV-only operation is controlled by the $T_{\mathrm{HPT,out}}$ temperature, which is without firing the SEV directly proportional to the LPT inlet temperature, the $T_{\mathrm{LPT,out}}$ measurement would increase with lower LPT efficiency. This would, however, be accompanied by a drop in power output due to a significant reduction of the enthalpy difference over the second turbine, which could not be retrieved from data (see Fig. 4.6 c)).

It can thus be concluded, that the omission of turbo set aging was valid, since it had only negligible and non-detectable influences on the models presented.

[2] A given VIGV position also defines the turbine outlet temperature by the operation cycle as explained in Sec. 3.1.2.

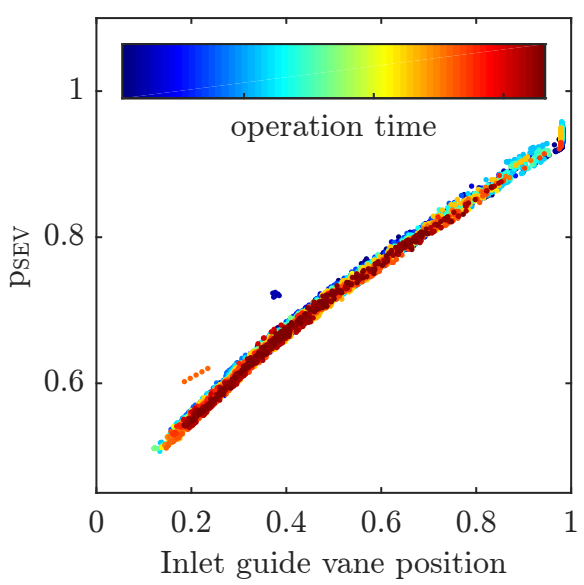

(a) SEV pressure over inlet guide vane position for ambient temperature range of 22-24°C

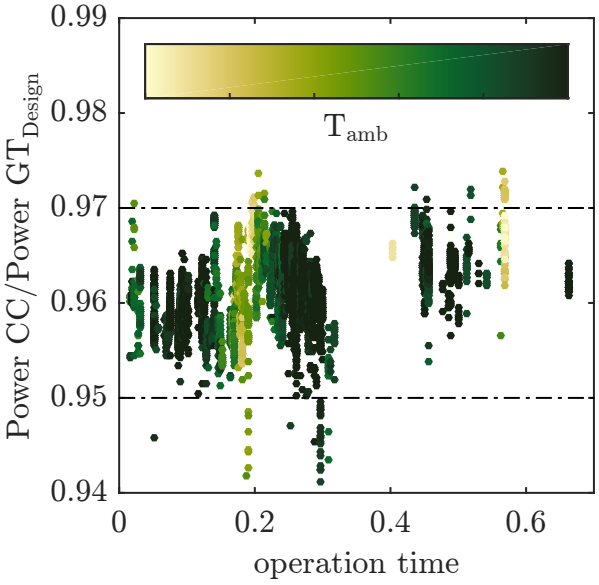

(b) Full load performance over lifetime

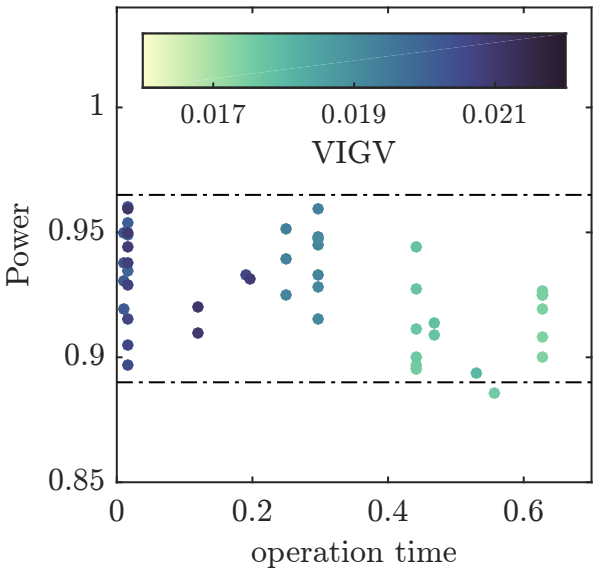

(c) Power during CC start in EV only operation (scatter caused by steam turbine ramp up)

Figure 4.6.: Investigations on turbo component aging influences. All scales are normalized to a reference value.

4.2.3. Uncertainty Analysis

Fig. 4.7 shows the uncertainty calculations superimposed to long-term performance of the respective emission prediction. For the NOx model, the uncertainty lay within the accuracy range introduced by the emission measurement system. CO prediction shows a larger uncertainty by nature, still in the range of the long-term model performance. As the model does not include the seasonal fluctuations evoked by the pressure change in the cooling air flow (see Fig. 4.4), a residual between theoretical uncertainty and actual prediction performance remained.

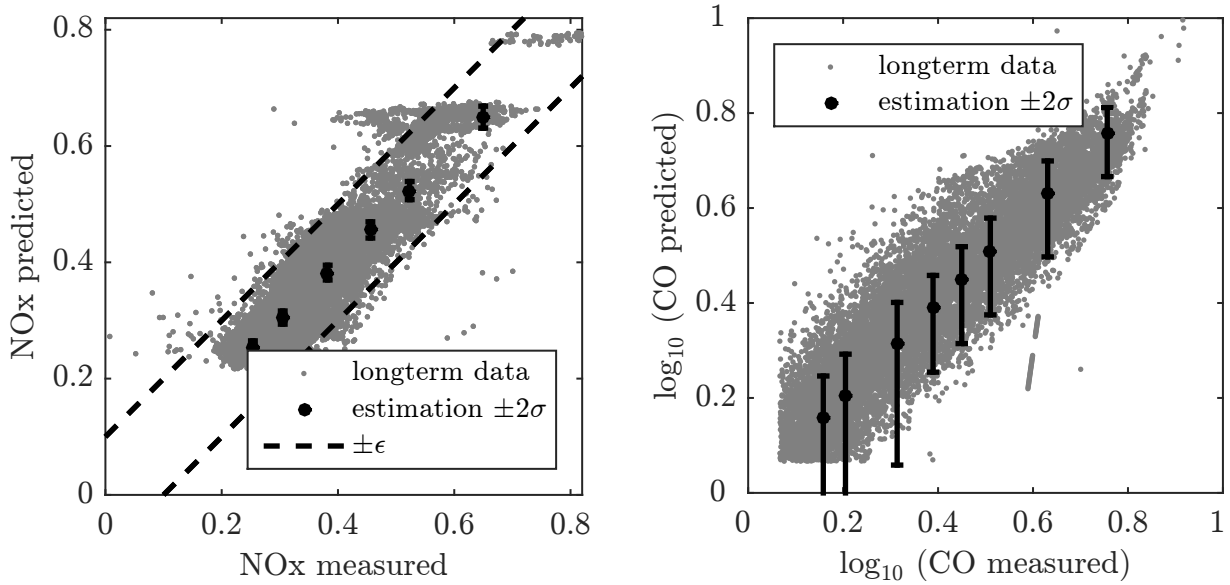

(a) NOx model **(b)** CO model

Figure 4.7.: Uncertainty evaluation for NOx and CO model. All scales are normalized to a reference value.

Nevertheless, uncertainty evaluation has proven that the model has sufficient accuracy for meaningful conclusions concerning the investigated aging-induced emission progression.

4.2.4. Sensitivity Analysis

Based on the above described uncertainty evaluation, the sensitivity analysis was performed by the calculation of Sobol Indices (see C.1.2) for selected full load (NOx) and low load points (CO). Tab. 4.3 shows the first-order Sobol indices calculated for sensitivity analysis.

Table 4.3.: Results of sensitivity analysis: Sobol Indices for input parameters at full load (NOx) at different engine settings and low load (CO).

		NOx model	NOx model	CO model
		full load	full load variation	low load
$T_{\mathrm{HPT,out}}$	measurement	0.0040	0.0373	0.0762
	shift	0.0357	0.3365	0.7086
	spread (min,max)			(0.1184,≈ 0)
$T_{\mathrm{LPT,out}}$		0.9227	0.6082	0.0154
Tk2		≈ 0	≈ 0	
VIGV		≈ 0	≈ 0	≈ 0
$\mathrm{m_{fuel,EV}}$		≈ 0	≈ 0	
Pk2		≈ 0	0.0086	
$\Delta \mathrm{p_{EV}}$		≈ 0	≈ 0	
$\mathrm{p_{SEV}}$		0.0325	0.0062	0.0156
$\mathrm{p_{amb}}$		0.0036	0.0024	≈ 0
$\mathrm{H_{amb}}$		≈ 0	≈ 0	≈ 0
$\mathrm{T_{amb}}$		≈ 0	≈ 0	
$\mathrm{C_{2+}}$				0.0478

Unsurprisingly, Sobol Indices[3] for temperature or aging-related measurements tended to be higher than those for pressures. That is due to the fact, that temperature measurements are generally more inaccurate and both phenomena (NOx and CO emissions) are mostly temperature-driven. Regarding the NOx model, the influence of the second combustor becomes evident. With the second combustor contributing the majority of NOx to the overall emissions at full load settings, the model is very sensitive to the $T_{\mathrm{LPT,out}}$ measurement. Thus, the aging-influenced parameters, such as temperature shift and ζ_{EV} have only negligible influence, since they affect only the EV combustor. As the sequential architecture allows for a variable fuel split between the two combustors, equivalent full load operating points exist with variations in the temperature settings. Depending on the fuel split, the importance of the $T_{\mathrm{LPT,out}}$ measurement decreases, since more power and thus NOx formation can be shifted towards the first combustor (see 4.3 NOx model (full load variation). The CO model reacts very sensitive to all parameters related to the $T_{\mathrm{HPT,out}}$ measurement, as the ignition delay is the driving force of the

[3]As explained in Sec. C.1.2, Sobol indices quantify the contribution of one parameter to the total output variance with 0=no contribution to 1=entire contribution

CO oxidation. $T_{\mathrm{HPT,out}}$ measurement, shift and spread contribute more than 90% to the first order variance of the model, making it the decisive input parameter.

4.3. Artificial Neural Network Performance, Evaluation and Comparison

Investigations of aging induced emission progression was also conducted with Artificial Neural Networks (ANN) for NOx and CO emission prediction. ANNs are proven to be generally capable of modeling emissions from given engine measurements, with worse RMSE (Tab. 4.4 & 4.5) than the semi-empirical models (Tab. 4.1 & 4.2) in all investigated data subsets of this study.

Table 4.4.: Fitting accuracy and longterm results from Artificial Neural Network for NOx prediction for engine A. Please refer to Sec. D for an explanation of the different cases.

	$\mathrm{rRMSE_{com}}$	$\mathrm{RMSE_{longterm}}$
raw	0.05	4.63
flame	0.09	2.04
flame aging	0.09	3.07
flame + amb	0.07	6.38

Table 4.5.: Fitting accuracy and longterm results from Artificial Neural Network for CO prediction

	$\mathrm{rRMSE_{com}}$	$\mathrm{RMSE_{longterm}}$
raw	0.03	0.49
flame	0.08	0.41

Results in Tab. 4.4 & 4.5 and Fig. 4.8 & 4.9 allow for some general observations: The accuracy in the training data (i.e. the commissioning data) set was better for all investigated cases (data subsets and emissions) than for the semi-empirical model (compare Tab. 4.4 & 4.5 vs. Tab. 3.3 & 3.4).

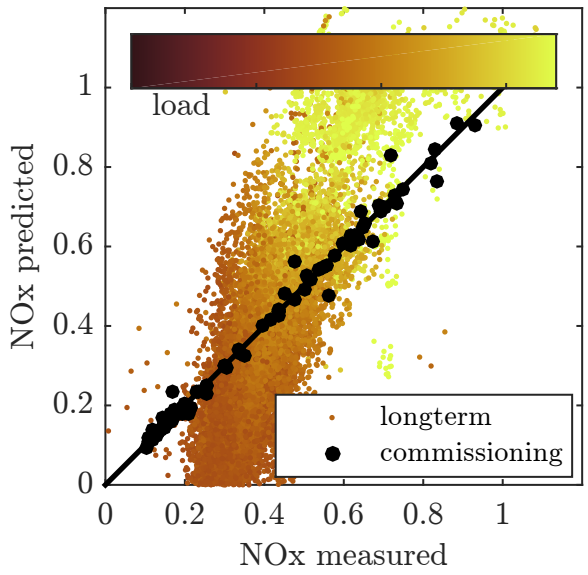

(a) NOx prediction by Neural Network with raw data as input without aging for engine A

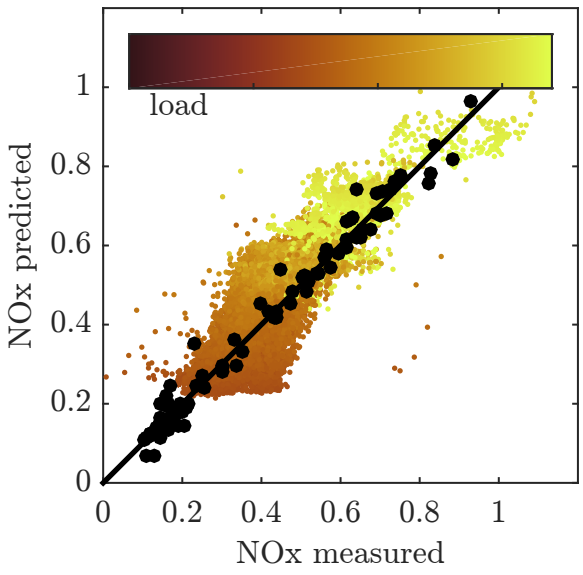

(b) NOx prediction by Neural Network with flame temperature as input without aging for engine A

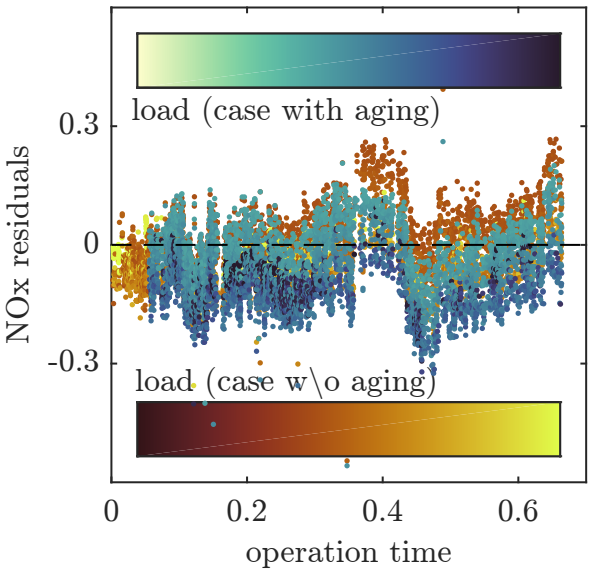

(c) NOx residuals by Neural Network over operation time with and without application of aging-correction for EV flame temperature for engine A

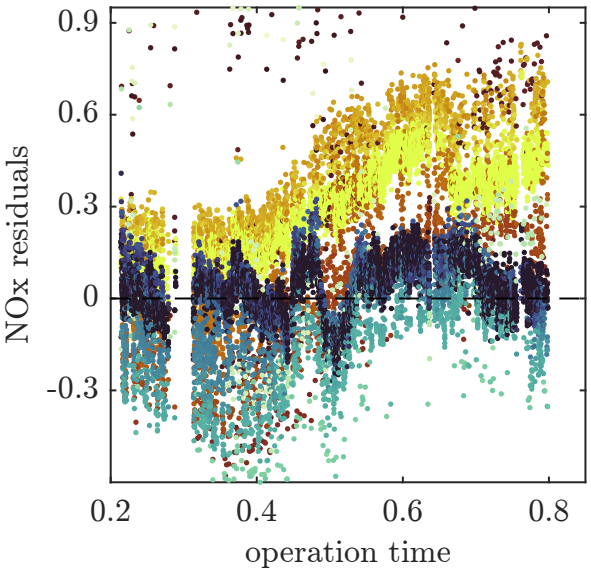

(d) NOx residuals by Neural Network over operation time with and without application of aging-correction for EV flame temperature for engine B

Figure 4.8.: Artificial Neural Networks applied to NOx emission prediction for engine A and B. Commissioning data used as training. Validation on long-term data. All scales are normalized to a reference value.
Figure reprinted from Lipperheide et al. [83].

As the error is of the same magnitude as the measurement accuracy, the severe problem of over-fitting may be present, despite a-priori determination of the neurons. Data subsets with more input parameters, such as ambient parameters or engine control parameters instead of the more comprehensive virtual hot gas temperatures, led to an even higher accuracy during training (indicated by the black dots for commissioning data in Fig. 4.8 & 4.9). Obviously, the higher number of neurons in combination with a wider data base also allowed for a more accurate fit.

When applied to long-term data, it can be seen that this gain in training accuracy adversely affected the actual ANN performance for long-term emission prediction. On the long-term data set, neural networks with worse training accuracy performed better. They obviously captured the general characteristics of the physics better and are less prone to overfitting than datasets with the given small number of datapoints but more parameters and neurons.

Moreover, the superior long-term performance in parameter sets with hot gas temperatures compared to the raw data sets is also another justification for the chosen calculation approach for hot gas temperatures by the mapping method (see Sec. 3.3.1). The long-term RMSE decreased significantly for the virtual data set without aging correction compared to the raw data set. For CO, prediction could be improved from 0.49 to 0.41 (-15%) in terms of RMSE and for NOx, the RMSE dropped from 4.54 to 2.04 (-56%). This improvement is also qualitatively visible in the parity plots for NOx (Fig. 4.8b) vs. Fig. 4.8a)) and CO (Fig. 4.9b) vs. Fig. 4.9a)).
Beside these general findings without consideration of the aging models, some results specific to NOx and CO prediction were obtained concerning the application of the previously defined aging models and are presented in the following paragraphs.

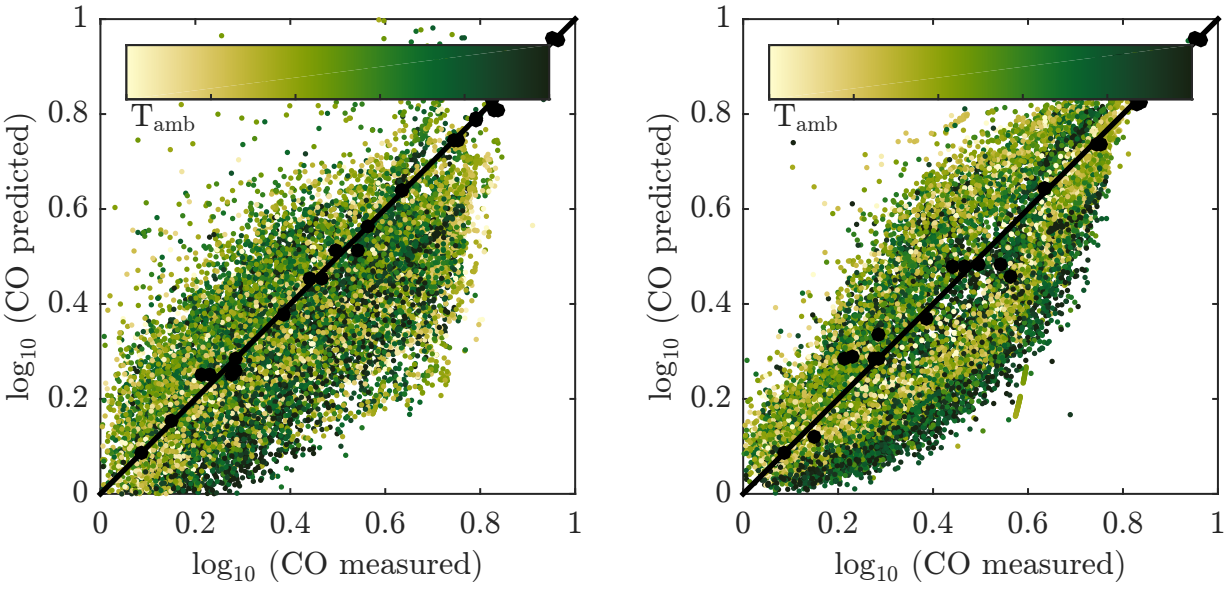

(a) CO prediction by Neural Network with raw data as only input

(b) CO prediction by Neural Network with flame temperatures as input

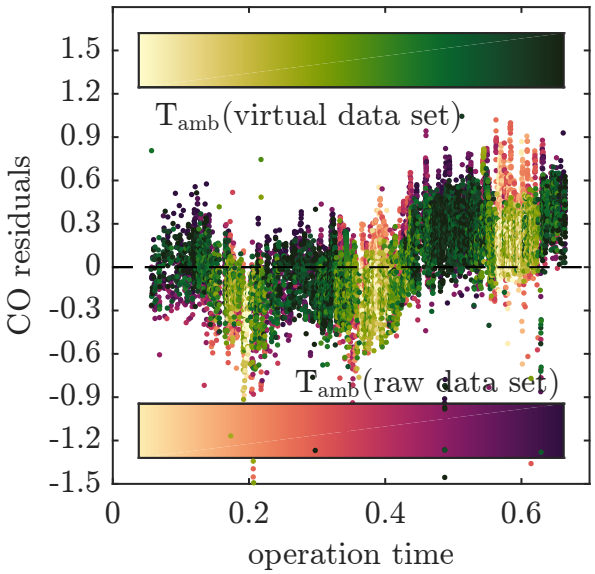

(c) CO residuals by Neural Network with flame temperatures as input compared to CO residuals by Neural Network with raw data input

Figure 4.9.: Artificial Neural Networks applied to CO emission prediction for engine A. Commissioning data used as training. Validation on long-term data. All scales are normalized to a reference value. Figure reprinted from Lipperheide et al. [83].

Unexpectedly, the long-term performance worsened from an RMSE of 2.04 ppm to 3.07 ppm when the aging model was used together with the ANN approach. A visual inspection of the residual plot in Fig. 4.8c) reveals the reason behind. Residuals show that the NOx increase with operating time observed in measured NOx emissions is appropriately captured and corrected by the aging model with, however, generally larger residuals: An initial discrepancy between prediction and measurements is kept throughout the operation time while the model without aging incorporation superimposes the initially negative residuals with the positive residuals at later operation times, thus leading to a seemingly better overall performance.
As engine B showed a stronger aging effect in the physically-based model (see Fig. 4.3), its aging performance was also tested in the framework of Neural Networks. Fig. 4.8 d) clearly shows a more distinguishable aging effect for the comparison between a ANN without and with flame correction, leading to a 23% reduction in terms of the RMSE.
In order to investigate the root cause of the initial mismatch of engine A, the data subset with flame temperatures and ambient conditions was tested. Fig. 4.10 shows that the initial mismatch disappeared when the data set was enriched by ambient parameters. However, the overall worsening of the prediction caused by the described overtraining superimposed the aging trend with a high scatter.

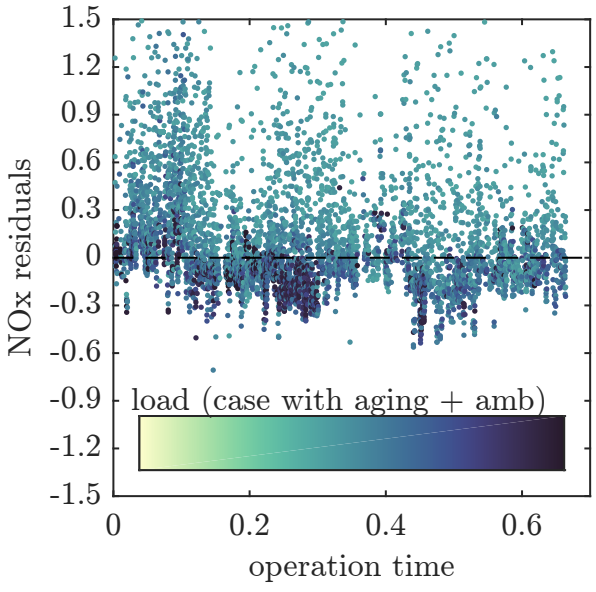

Figure 4.10.: NOx residuals by Neural Network over operation time with aging-correction for EV flame temperature and incorporation of ambient parameters for engine A.
Figure reprinted from Lipperheide et al. [83].

CO predictions improved slightly when the engine model was used (see Tab. 4.5), thereby reaching similar accuracy as the semi-empirical model, when no aging model was used (compare Fig. 4.9b) vs 4.9a) and Tab. 4.2). Yet, CO prediction shows a lenticular distribution (Fig. 4.9b)) with a deviating emission behavior for high operation times (Fig. 4.9c)). When investigating these residuals over operation time (Fig. 4.9 c), the CO emission aging causing this deviation in the scatter-plot is also evident.

4.4. Impact of Operation Mode on Aging

The aging parameter $T_{\mathrm{HPT,out}}$-drift shows a clear correlation with flexible operation for the investigated GT24/GT26 fleet data (see Fig. 4.11 a)). The fleet data reveals that gas turbine in flexible operation age faster. The scattering as visible in Fig. 4.11 was tested against other possible influence parameters as e.g. the average load level during operation, which showed no correlation. Also the operation time, indicated by the colorbar, is uncoupled from the correlation.

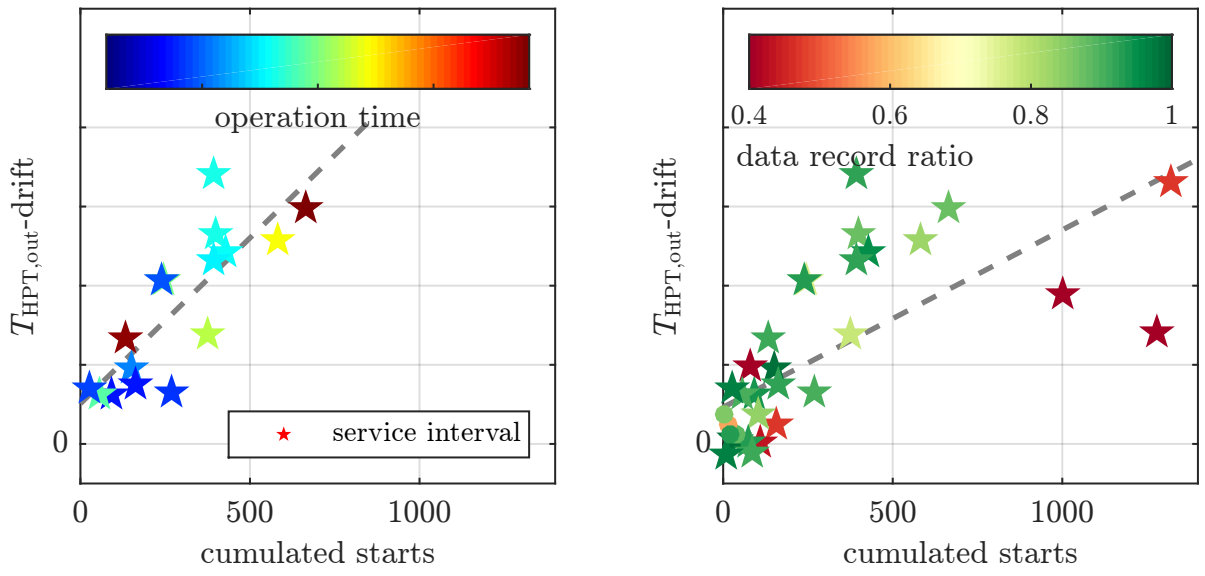

(a) Outliers (infrequent data, marginal aging, short time intervals) erased from data

(b) Entire dataset

Figure 4.11.: Aging phenomenon of HPT outlet measurement drift compared to engine starts per day of available data logging as measure of flexible gas turbine operation. Scales not shown due to confidentiality.

As a comparison, Fig. 4.11b) shows a similar result for the entire available data set with results from insufficient data sets. Even though the scatter is increased and outliers are present, the general trend is kept with a notable uncertainty in the high cyclic operation region (cumulated starts $\approx$ 1000+). The spread of data points around zero, especially the negative temperature drift, is physically not meaningful but caused by the inaccuracy of the drift detection when data becomes scarce. The engines and their inspection periods with highly cyclic operation would definitely enrich the investigation as they provide more variance in the operation regime but had to be handled as outliers due to their infrequent and thus unreliable data.

5. Conclusion & Outlook

The following chapter will conclude findings from this work in its two core areas. The first part mainly summarizes the novel modeling approach, which combines emission modeling with aging modeling for commercial long-term operation.
The conclusive part of this chapter embraces the initial motivation of this work and takes up the application of long-term emission modeling for APM (Asset Performance Management).

5.1. Long-term Emission Modeling

Encouraging results were obtained for NOx and CO emission prediction for a heavy duty gas turbine in commercial operation. Measurements from operation monitoring served as input to an engine model, by which virtual measurements, such as relevant temperatures, were created. The reconstruction of virtual temperatures by turbine mappings turned out to be a reliable method for hot gas temperature estimation in the combustor. By incorporating operation data into the engine model, these virtual measurements also relate to the actual engine condition. A reliable NOx correlation formed on training data uses these virtual and real measurements as input parameters and successfully allowed for detection of deterioration in the combustion process, by comparison of predicted and measured NOx emissions. Based on both measured parameters and virtual measurements from the same engine model, an analytic CO model was also identified on commissioning data of the investigated gas turbines.
Particular focus has been given to the influence of aging in long-term commercial operation, which emerges as a sensible contribution requiring appropriate consideration in the engine and emission models. In the course of this study, three main aging effects were identified and quantified. The NOx emission progression in the EV combustor is majorly caused by a drift in the temperature measurement, which is control variable. Furthermore, the NOx emission progression is also affected by a change in air distribution by decrease of pressure drop.

The phenomenon for deteriorating CO emission performance was identified as aging induced cold gas leakage and accordingly modeled. This leakage locally extends the ignition delay of the affected burners in the sequential combustor, and thus increases the CO emission level by reducing the time available for oxidation. This aging phenomenon was successfully modeled by grouping burners into cold and hot sections.
The physically based long-term modeling approaches for NOx and CO presented here augment the existing research on emission modeling, which often overlooked the ever increasing importance of long-term prediction skills.

In the framework of modeling, ANNs as a prominent representative of artificial intelligence in 'big data' were benchmarked against the physically-based modeling. It turned out, that ANNs were capable of dealing with the investigated cases, even though commissioning data is very small as a training set for ANNs. CO long-term prediction by ANN was in the order of the semi-empirical benchmark modeling for all tested data sets with varying level of design information. A clear aging trend could be detected by the model, which could, however, not be enriched by a dedicated aging model due to its structure. Still, a pure statistical approach with only raw input data was not able to detect and model NOx aging phenomena correctly. When an engine model with aging incorporation was added to the method, ANNs yielded acceptable results in the range of the physically-based method for NOx prediction. In this case, ANNs only replaced the NOx emission modeling but the physically-based engine model was still used for data pre-processing. This is in accordance to reported ANN applications in literature, where ANNs are used for fault detection in combination with detailed component-level degradation models for training [125, 126, 127]. Thus, ANNs offer a very good alternative to semi-empirical approaches for emission modeling if all required input parameters are available. ANNs could even outperform semi-empirical approaches when emission behavior is difficult to model with few global parameters due to highly non-linear flow and mixing behavior as, for example, in staged combustion.
Overall, it can be concluded, that an engine model based on OEM's detailed know-how is required, although ANNs have proven to successfully and efficiently master part of the modeling scope. In order to reach satisfactory accuracy of long-term emission modeling, at least a physically-based pre-processing step was necessary for ANNs.

5.2. Incorporation into APM

The long-term emission modeling can also be used as a precious tool in APMs. Its utilization in APM approaches, as discussed in the following, may promise to increase engine availability, reduce production losses and costs while maintaining legal emission compliance over full- and partload as well as operational flexibility to low loads.

5.2.1. Adaption of Commissioning Strategy

A major task of engine commissioning is the mapping of the NOx emissions at different load levels. These NOx mappings are a precious source of information for the engine's characteristic, especially in sequential combustion with myriad possibilities of engine set points.

With an analytic and reliable model, as available for NOx from Sec. 3.3.2, the number of needed measurements during commissioning can be reduced. The primary task of the measurements is the identification of the model parameters. The identified model then allows for an entire mapping for various load levels, which were initially not measured. Such a virtual commissioning approach is based on a design-of-experiment (DoE) method (see Appendix C.2), as performed here with an open-source toolbox developed by Joscha Reimer [128]. The three different set points ($VIGV$,$T_{\mathrm{HPT,out}}$ and $T_{\mathrm{LPT,out}}$), which unambiguously define the engine's operation, were the only input parameters to this DoE. Remaining parameters necessary for the NOx model, such as flame temperatures and pressures, were calculated accordingly from the simplified engine model. Fig. 5.1 shows a possible distribution of an optimized measurement strategy in comparison to the status quo. The design-of-experiment achieved to potentially reduce the number of measurements to only 30, compared to the 90 data points used for engine A (see Tab. 3.1), while maintaining a comparable quality criterion (see Tab. 5.1) as defined in Appendix C.2.

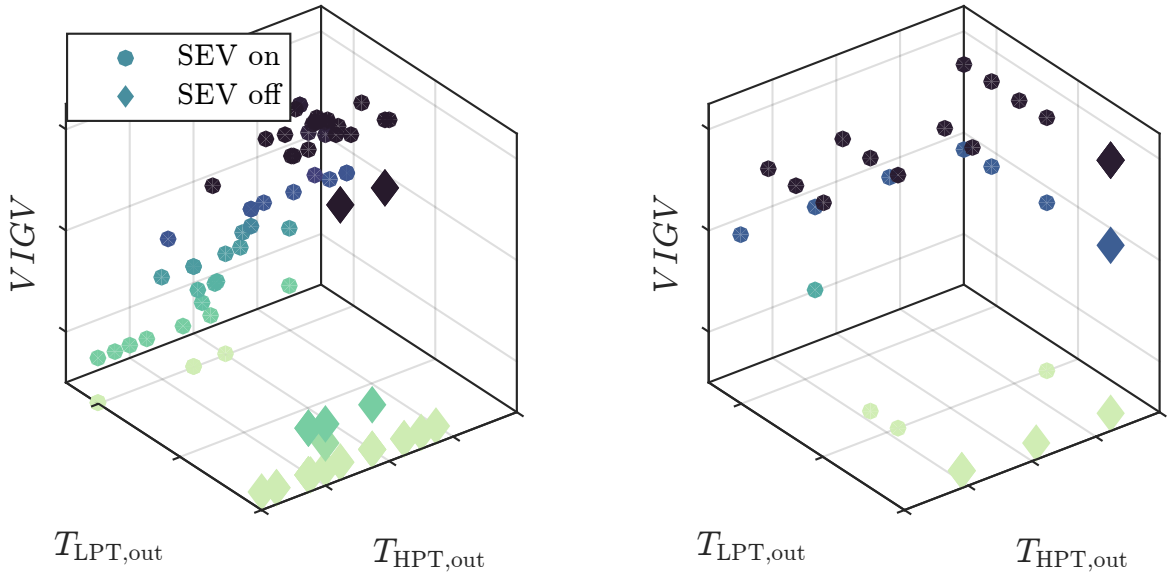

(a) Location of commissioning data points with respect to engine set points

(b) Optimized location of engine set points for virtual commissioning

Figure 5.1.: Necessary amount of commissioning measurements to cover NOx emission characteristics during commissioning of Engine A (a) and when DoE method is used (b). Load point with a turned off SEV do not relate to a defined $T_{\mathrm{LPT,out}}$ and are thus added at the lower end of the axis.

Table 5.1.: Quality criterion for existing commissioning strategy and DoE for different initial parameter estimations (0,±20 % deviation from 'true' parameters)

	-20%	0%	+20%
status quo	0.27	0.06	0.02
DoE	0.49	0.1	0.03

A virtual commissioning strategy for CO could not be performed. The DoE formulation of CO was in this case ill-conditioned. Without the consideration of ambient temperature, which is of course no control parameter, p_{SEV} and $T_{hg,SEV}$ do not vary independently from each other in the critical load level for CO emissions. However, with only $\approx$ 25 data points used for the parameter identification in the present study, there is less need for a reduction of measurements. Since the check of NOx emission compliance is only one task during commissioning, the adaption of the described DoE

strategy to the actual engine demands consideration of other relevant scopes, such as pulsation mappings, proof of guaranteed performance and start-up procedures.

5.2.2. Impact of Operation on Aging

The established link between an aging mechanism, as investigated in this work, and the operation regime provides the possibility for a more accurate planning of future maintenance timing and scope. This may eventually improve asset reliability, availability and maintenance cost. Concurrently, it can be used to optimize the business case for plant operators by properly accounting for lifetime and maintenance cost impacts when defining the target operation profile.

5.2.3. Avoidance of Manual Adjustments

Findings from this work can be used to recalculate optimum engine parameters for an aged engine. As a long-term goal, obtained optimum control parameters can be applied online to engine control during operation to meet emission limits over component lifetime while maintaining optimum engine performance with low maintenance costs. The effect depicted in Fig. 5.2 could thus be avoided. A frequent re-adjustment of turbine outlet temperatures opposite to the trend of measurement deviation (see Sec. 3.3.4.1) was manually performed by service teams during the service interval. The use of the detected and validated measurement deviation at the turbine outlet temperature measurement could instead correct the temperature set parameter online, recovering this aging phenomena by simple control interventions and thus ensuring a stable engine operation throughout lifetime.

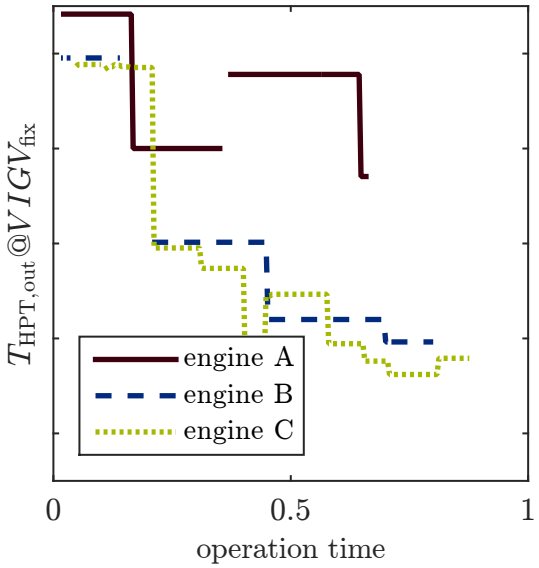

Figure 5.2.: re-adjustments of control parameter $T_{\mathrm{HPT,out}}$ or respective turbine inlet control temperature during operation time to maintain hot gas temperature and balance overheating caused by apparent temperature drift. Scales not shown due to confidentiality.

5.2.4. Adaptive Control Concept

If aging is unrecoverable, gas turbine operation can still balance its negative effects by an advanced control system, incorporating aging and emission models to a predictive higher-level control system. The temperature spread at the high pressure turbine outlet is for example such a non-recoverable aging phenomenon. With ongoing aging progression, low load levels get closer to the CO emission limit, which could, for example, be compensated on the expense of other performance or emission parameters.
Such adaptive re-adjustments of the operational concept clearly require an optimization by, at least, trial-and-error, which could be done virtually with the developed models. One could also think of a remote optimization system to automatically adjust the set points of the control concept, without touching the actual safety-relevant engine control. The aging and emission models developed here are valuable, but not the only, input functions to this optimization. It has to incorporate various further constraints such as combustion instabilities and lifetime reduction. In this context, special focus must also be given to the exact optimization target, which might differ by use case from, for example, maximum power output to efficiency to lifetime.
Aging and emission are thus a key component of a future optimization system. Its fi-

nal application, however, requires a thorough analysis and definition of the operator's specific targets and consideration of other aspects of gas turbine operation.

5.2.5. Monitoring, Diagnostics & Health

The most obvious application of aging-induced emission analysis and its modeling is monitoring and diagnostics during commercial long-term operation. The models were able to represent the engine behavior for several years of operation between major overhauls with an adequate accuracy when accounting for aging effects, reducing the prediction error of emission models significantly to about 54%(NOx) and 60%(CO).
The reliable description of NOx and CO emissions in aged combustors may eventually help to determine engine health parameters for commercial long-time gas turbine operation. Quantifying the influence of engine aging on emissions allows for an online evaluation of the engine state by emission monitoring solely and emerges as a meaningful indicator for a condition-based maintenance. Especially in combination with the fleet aging analytics, the validated emission models are a powerful tool for scenario calculations, where emission progression is predicted for different stages of aging, depending on the operation regime of the engine (Sec. 5.2.2).

5.3. Gas Turbine 4.0 in Asset Performance Management

Improvement potential by the findings of this work can be identified as examples of different levels of APM. Discussed concepts correspond to the initially presented APM scheme (see Fig. 2.1), which can now be enriched by application examples in Fig. 5.3.

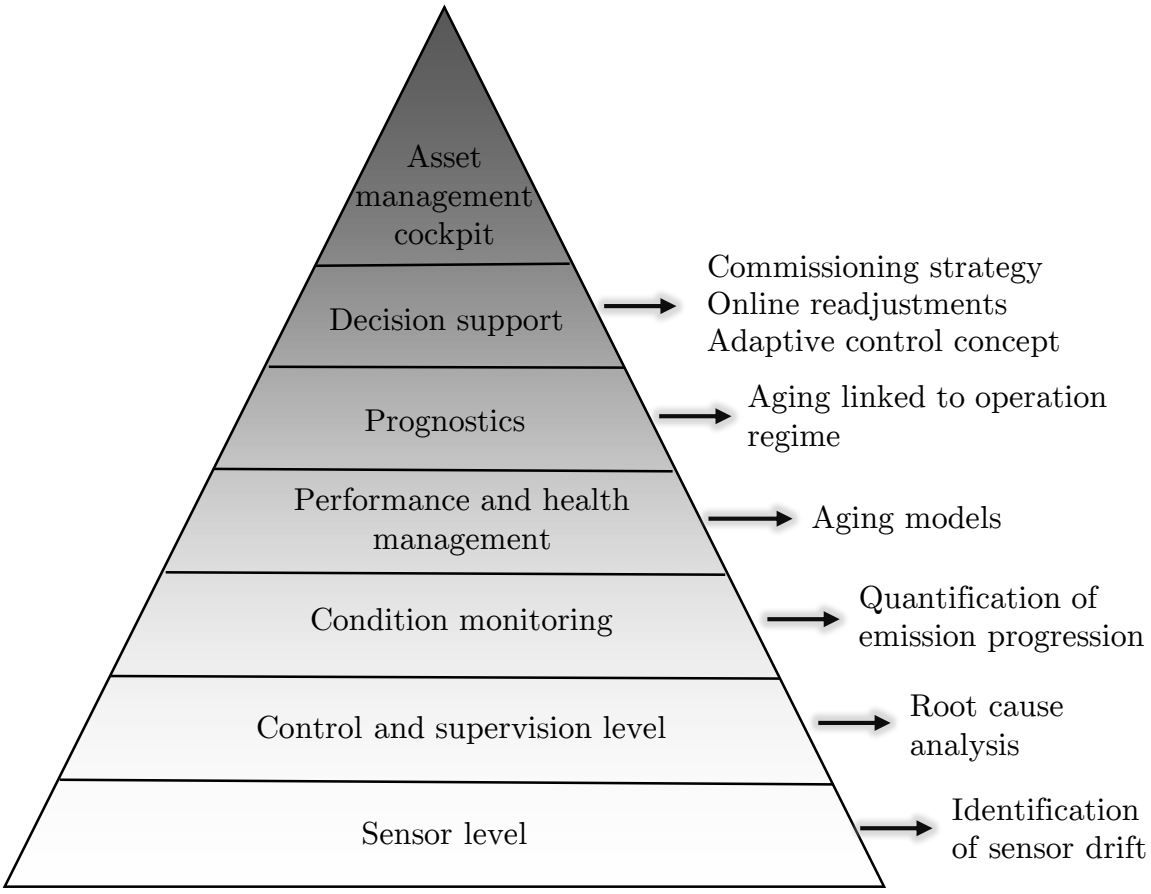

Figure 5.3.: Incorporation of discussed approaches into different APM levels as defined in [32]

By means of reliable emission and aging models, turbine outlet temperature measurements can be evaluated on the sensor level and be identified as the root cause for deviations on the control level. The validated and modeled aging phenomena can serve as an indicator for monitoring and diagnostics in performance and health management. Its extension to the fleet also allows for aging prognostics as a function of the operation regime. Examples for decision support in maintenance are the proposed adaption of commissioning strategy to save on costly commissioning measurements, the adaption of the control concept to aging and the recovery of aging phenomena. These approaches are bricks of the APM pyramid, building the foundation to a future possible Asset Management Cockpit to be applied by the gas turbine manufacturer (see Fig.2.1).
In the long-run, these approaches contribute to the integral goal of a digitally supported gas turbine 4.0. As mentioned in the introduction, the digitalization creating physical twins of physical assets is a key factor to economical success of machine fleets of all kinds. Especially for gas turbine use in the competitive power market environment, its ongoing optimization is essential, for which digital support offers a cost-effective possi-

bility compared to costly component development. In the framework of a gas turbine 4.0., emission-based digital approaches are just one aspect. In the long-term, a specific evolution of sensors overcoming limits of todays' measurement technology and an integration of design and manufacturing processes are imaginable. This ongoing combined effort could bring the gas turbine to the digital century, ensuring a continuous optimization of engine performance in the entire fleet, which could in return improve the digital 'gas turbine twin' by an ongoing data generation.

Appendix

A. Thermodynamical Modeling

Thermodynamical modeling is used for the calculation of humidity in the exhaust gas, as explained in the following.

A.1. Global O_2 Element Balance

The measured relative humidity (RH) at the intake is translated into the water saturation pressure for a given ambient temperature by:

$$x_{\mathrm{H_2O}} = \frac{p_{\mathrm{sat}}}{\frac{p_{\mathrm{amb}}}{RH} - p_{\mathrm{sat}}} \tag{A.1}$$

The saturation pressure p_{sat} for the given ambient temperature is calculated by an Antoine-like equation from [129]. The composition of dry air is simplified to 21% O_2 and 79%N_2, so that oxygen content of the humid air is calculated to $x_{\mathrm{O_2}} = (1 - x_{\mathrm{H_2O}}) \cdot 0.21$. The global air-to-fuel equivalence can be obtained from the measured oxygen content in the exhaust gas by:

$$\lambda = \frac{0.21}{0.21 - x_{\mathrm{O_2},exhaust}} \tag{A.2}$$

Combustion is assumed to be complete and with CH_4 only, so that the exhaust composition can be derived. Humidity is increased by $\frac{2 mol \mathrm{H_2O}}{1 mol fuel}$, $\frac{1 mol \mathrm{CO_2}}{1 mol fuel}$ is formed, $\frac{2 \cdot (\lambda - 1) mol \mathrm{O_2}}{1 mol fuel}$ and $\frac{2 \cdot (\lambda) \cdot \frac{0.79}{0.21} mol \mathrm{N_2}}{1 mol fuel}$ and $\frac{2 \cdot (\lambda) \cdot \frac{x_{\mathrm{H_2O}}}{x_{\mathrm{O_2}} mol \mathrm{O_2}}}{1 mol fuel}$ remain in the exhaust. Total moisture content is then calculated by the fraction of $x_{\mathrm{H_2O},exhaust} = \frac{2 + 2 \cdot (\lambda) \cdot \frac{x_{\mathrm{H_2O}}}{x_{\mathrm{O_2}} mol \mathrm{O_2}}}{1 mol fuel}$ to the total specific amount of exhaust gases.

B. Chemical Modeling

Chemical modeling uses detailed information of underlying elementary reaction mechanisms to investigate kinetics in any chemical reaction. In the framework of this work, special focus is given to pollutant formation.

B.1. Reaction Mechanism

Simple gross chemical equations are not sufficient when assessing chemical reactions beyond stochiometry and energy balances. The investigation of time-resolved reaction progress needs information of the underlying elementary reactions and their kinetics, as each of them could determine the overall speed of reaction. Those elementary equations for a certain chemical reaction (combustion of natural gas in this particular case) are then combined to a reaction mechanism. Two of the mechanisms available are used in the present study and are presented in the following.

B.1.1. Gri30

The Gri30 [130] is a complementary mechanism to model natural gas combustion, including NOx formation and reburn chemistry, which has been the industry standard for the last two decades [131]. The Gri30 is developed and under ongoing optimization at UC Berkeley. The latest version features a total of 53 species and 325 reactions, which are continuously tested against experimental data, such as ignition delays and species profile measurements.

B.1.2. Saudi Aramco Mechanism

Advances in measurement techonologies, such as shock tubes and laser diagnostics, improved the accuracy of measured kinetic coefficients and urged to re-develop reaction mechanisms. Among these, the Saudi Aramco Mechanism (AramcoMech) [106], developed at the National University of Ireland, Galway, is used in this work. Throughout

the development of the AramcoMech, special attention was given to the accurate assessment of varying fuels from C1-C4 and their influences on combustion kinetics. Still, NOx chemistry is not in the scope of this mechanism, so that Gri30 is used in this study, when referring to NOx kinetics.

B.2. Reactor Modeling

The elementary chemical reactions as defined in the reaction mechanism above have to be connected to a reactor model in order to allow for the simulation of species concentration, pressure and temperature and their progress over time. The model thus serves as a framework for the interaction between the defined elementary reactions of the reaction mechanism. As the focus of reactor modeling is rather on the chemical phenomena than on flow or corresponding mixing, the underlying only assume very basic flow states, such as a batch reactor, a mixed flow reactor and a plug flow reactor (see Fig. B.1). The flow states in return define the governing influences on a reaction, which is the available residence time at a certain species concentration and temperature.

B.2.1. Batch Reactor

The batch reactor has no in- or outflows and is characterized by a uniform composition inside at each timestep, thus a perfect mixing. The uniform composition at a certain time results from the progress of reaction, starting from the initial species concentration, and the initial temperature and pressure only. These parameters, however, change with time as reactants are continuously converted exo- or endothermically to products until equilibrium, so that the model has to be solved time-dependently with an adequate time resolution. A batch reactor model thus gives the concentration trends over time under the assumption of a perfectly mixed fluid, evolving from an initially set state.

B.2.2. Mixed Flow Reactor

The so-called mixed flow reactor similarly assumes a perfect and immediate mixing inside the reactor. In contrast to the batch reactor, a mixed flow reactor features in- and outflow. While the state of the reactants and their composition at the inflow is set, the outflow is assumed to correspond to the state of the species inside the reactor, which in return results from the total residence time inside the reactor at steady conditions. The residence time is yielded by the available reactor volume, the amount of incoming flow and the occurring temperature at reaction progress. Thus, the resulting outflow

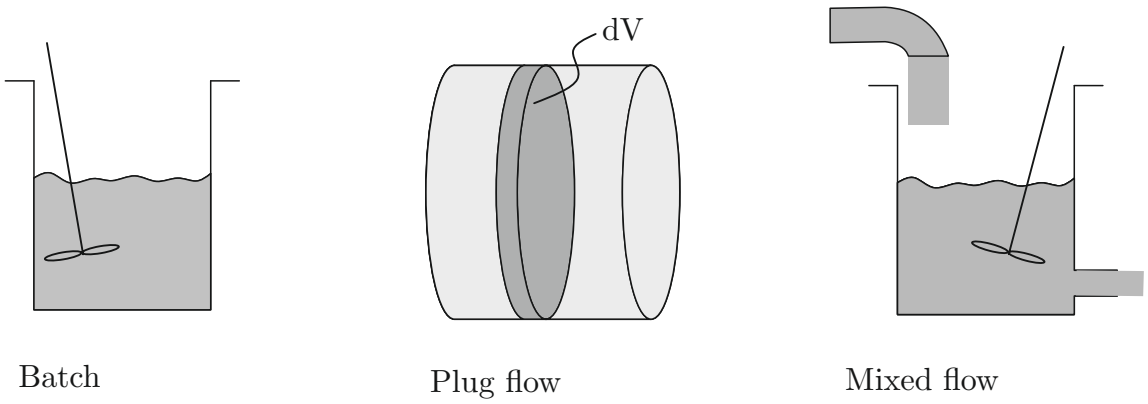

Figure B.1.: Basic chemical reactor model configurations

cannot be modeled time-dependent but reaches a steady state for the incoming flow composition and available reactor volume given.

B.2.3. Plug Flow Reactor

A plug flow reactor follows a hypothetical volume of reactants of an initial state through the reactor with an initial velocity. The considered volume is assumed to be perfectly mixed inside but with no interactions to its neighboring volumes. A comprehensive understanding of the plug flow reactor is thus a row of sequential batch reactors, each with an adequately small volume to model one time step of the reaction. Another realization of a plug flow is a single batch reactor moving along in space with each single time step. There, its velocity may change by a transition in density of the fluid (for example by temperature or non-equimolar reactions), which can also be accounted for by introducing the simple relation of velocity v, time t and distance travelled s for each batch reactor time step: $v = \frac{s}{t}$. The final product composition after the given traveling time or distance of the single batch reactor is thus at steady state as it evaluates the transient single batch reactor after the fixed traveling distance.

C. Mathematical Methods

Mathematical methods employed in this work are two statistical methods for very special applications. The polynomial chaos expansion can replace Monte-Carlo methods for uncertainty assessment with the advantage of less computational power and the presented design of experiment approach estimates the best data distribution for parameter identification of a known correlation.

C.1. Polynomial Chaos Expansion

The polynomial chaos expansion is able to assess uncertainty and sensitivity by creating a statistical metamodel of the actual model. The following chapter explains the basic approach and its application to the current work by the UQ Toolbox [113] for Matlab, which is used in this work.

C.1.1. Evaluation of Uncertainty

The polynomial chaos expansion of a computational model with output Y and function M of a random input vector with independent components X (described by a joint density probability function ρ) is defined as the sum of multivariate polynomials $\Psi_\alpha(X)$ and corresponding coefficients y_α.

$$Y = M(X) = \sum_{\alpha \in A} y_\alpha \Psi_\alpha(X) \tag{C.1}$$

The multivariate polynomials $\Psi_\alpha(X)$ are choosen to be orthonormal to a probability distribution $\rho(\xi)$.

$$\int \Psi_\alpha(\xi)\Psi_\beta(\xi)\rho(\xi)\mathrm{d}\xi = \delta_{j,k} \tag{C.2}$$

As for the probability distribution of uncertain input parameters there are different assumptions possible. A common approach is to assume a Gaussian distribution for uncertainty in the input parameters with:

$$\rho(\xi) = \frac{1}{\sqrt{2\pi}} \exp^{-\xi^2/2} \tag{C.3}$$

In the special case of a Gaussian as defined probability distribution, the polynomials must be of a Hermite Polynomial shape to fulfill orthonormality.

$$\Psi_\alpha(\xi) = \frac{H_{e_\alpha}(\xi)}{\sqrt{\alpha!}} \tag{C.4}$$

,with

$$H_{e_\alpha}(\xi) = (-1)^\alpha \cdot \exp(\xi^2) \cdot \frac{\mathrm{d}^\alpha}{\mathrm{d}x^\alpha} \exp(-\xi^2) \tag{C.5}$$

In order to identify the coefficients y_α the attribute of orthonormality is used. Equation C.1 is multiplied with Ψ_β which corresponds to a Galerkin Projection:

$$y_\alpha = \mathbb{E}\left[M(X) \cdot \Psi_\alpha(X)\right] \tag{C.6}$$

The computational intense analytic solution of the integral can be simplified by Gaussian Quadrature, using a finite formulation of the integral at N locations with weights $w^{(i)}$,

$$y_\alpha = \int M(\xi)\Psi_\alpha(\xi)\rho(\xi)\mathrm{d}\xi \approx \sum_{i=1}^{N} w^{(i)} M\left(\psi^{(i)}\right) \Psi_\alpha\left(\psi^{(i)}\right) \tag{C.7}$$

so that y_α of the PCE model are fully defined from $M\left(x^{(i)}\right)$ actual values from the real model.

When calculating the statistical moments, the above introduced PCE metamodel enables a direct assessment of the expectation value μ and variance σ from coeffecients y_α. The expectation value of the model M for normally distributed input parameters is defined and expressed in PCE as:

$$\mu(M) = \int M(\xi) \cdot \rho(\xi)\mathrm{d}\xi = \sum_\alpha y_\alpha \int \rho(\xi)\Psi_\alpha(\xi)\mathrm{d}\xi \tag{C.8}$$

Since the Hermite Polynom $\Psi_0 \equiv 1$ by definition, the expression $\int \rho(\xi)\Psi_\alpha(\xi)\mathrm{d}\xi$ is simplified

$$\int \Psi_\alpha(\xi)\rho(\xi)\mathrm{d}\xi = \int \Psi_\alpha(\xi)\Psi_0(\xi)\rho(\xi)\mathrm{d}\xi = \langle \Psi_\alpha, \Psi_0 \rangle = \delta_{\alpha,0} \tag{C.9}$$

so that the expectation value can directly be drawn from coefficient y_0:

$$\mu = \mathbb{E}\left[M(X)\right] = y_0 \tag{C.10}$$

Variance σ is defined as the expectation of the squared deviation of the variable $M(X)$ from its previously calculated mean $\mu(M)$. As the square of the polynomials introduces

the Kronecker symbol by the definition of the orthonormal basis in C.1, the variance is reduced to the sum of squared coefficients y_α:

$$\sigma = \mathbb{E}\left[(M(X) - \mu(M))^2\right] = \sum_{\alpha \in A, \alpha \neq 0} (y_\alpha)^2 \tag{C.11}$$

C.1.2. Variance-based Sensitivity Analysis

Additionally, PCE offers a possibility for fast computation in variance-based sensitivity analysis by first-order Sobol Indices. The Sobol Index S_v of input parameter X_i, determines the variance of output Y with X_i fixed at its 'real' value x_i^* :

$$S_v = \frac{Var[Y|X_i = x_i^*]}{Var[Y]} \tag{C.12}$$

Since the 'real' value x_i^* is not known, it is replaced by the expectation value of X_i:

$$S_v = \frac{Var[\mathbb{E}[Y|X_i]]}{Var[Y]} \tag{C.13}$$

This first-order Sobol Index can thus be interpreted as the contribution of X_i to the overall output variance or the change in variance if the investigated input parameter X_i was fixed. The Sobol decomposition itself is expressed by:

$$Y = f_0 + \sum_{i=1} f_i(x_i) + \sum_{i<j} f_{i,j}(x_i, x_j) + ..., \tag{C.14}$$

or in more general terms:

$$f(x) = f_0 + \sum_{\substack{v \subset \{1,...,g\} \\ v \neq \emptyset}} f_v\left(x_v\right) \tag{C.15}$$

by introducing $v := \{i_1, ..., i_k\} \in \{1, ..., g\}$ and the subvector x_v denoting components contained in v. A condition of the function is their orthogonality, thus:

$$\int_0^1 f_{i_1,i_2,...,i_s}\left(X_{i_1}, X_{i_2}, ..., X_{i_s}\right) dX_k = 0, \text{for k} = i_1, ..., i_s \tag{C.16}$$

The expectation value, which is defined as the integral over X, can then be calculated for the entire input parameter set:

$$f_0 = \mathbb{Y} \tag{C.17}$$

The calculation of conditional expectation values (with fixed input X_i, thus not subject to definition C.16) further leads to for the first two parameters X_i and X_j:

$$\begin{aligned} f_i\left(X_i\right) &= \mathbb{E}\left(Y|X_i\right) - f_0 \\ f_ij\left(X_i, X_j\right) &= \mathbb{E}\left(Y|X_i, X_j\right) - f_0 - f_i - f_j \end{aligned} \tag{C.18}$$

By this feature, variance is easily computable:

$$\int_0^1 f^2(X)dX - f_0^2 = \sum_{s=1}^{d} \sum_{i_1<...<i_s}^{d} \int f_{i_1,...,i_2}^2 dX_{i_1}, ..., dX_{i_s} \tag{C.19}$$

leading to

$$\mathrm{Var}(Y) = \sum_{i=1}^{d} V_i + \sum_{i<j}^{d} V_{ij} + ... + V_{12...d} \tag{C.20}$$

, where

$$\begin{aligned} V_i &= \mathrm{Var}_{X_i}\left(\mathbb{E}_{X_{\sim i}}\left(Y|X_i\right)\right) \\ V_{ij} &= \mathrm{Var}_{X_{ij}}\left(\mathbb{E}_{X_{\sim ij}}\left(Y|X_i, X_j\right)\right) - V_i - V_j \end{aligned} \tag{C.21}$$

Traditionally, Sobol Indices are also evaluated by computationally expensive Monte-Carlo-Methods. Instead, the PCE can be rearranged into summands of increasing order. Equation C.1 is reordered to:

$$M(X) = y_0 + \sum_{\substack{u\subset\{1,...,g\} \\ u\neq\emptyset}} \sum_{\alpha\in A_u} y_\alpha \Psi_\alpha(X) \tag{C.22}$$

with the truncation set A_u:

$$A_u = \{\alpha \in A : k \in u \Leftrightarrow \alpha_k \neq \emptyset, k = 1, ..., g\} \tag{C.23}$$

A comparison of equation C.22 and equation C.15 provides:

$$f_v\left(x_v\right) = \sum_{\alpha\in A_v} y_\alpha \Psi_\alpha(X) \tag{C.24}$$

Finally, the variance C.20 can be directly drawn from the coefficients of the PCE:

$$\mathrm{Var}[f_v\left(x_v\right)] = \sum_{\substack{v\subset\{1,...,g\} \\ v\neq\emptyset}} \left(y_\alpha\right)^2 \tag{C.25}$$

C.2. Design of Experiment

Design-of-Experiment (DoE) [128] approaches allow for an a-priori choice of variable variations in an experiment. DoE methods can, for example, optimally define the choice

of investigated experimental set-ups to cover a certain space of possible variations when no additional information of analytic relation between parameters exists. Moreover, the functional dependence of experimental variables is often already known by physical laws. Experiments are then only conducted to yield parameters, which adapt the known functional shape. In this case, model based design of experiments may identify the experiments with the highest amount of information in the first place, so that combinations of variables with less information on the overall function behavior can be waived from possibly costly experimental agendas. Mathematically, this model-based design of experiment can be expressed as a minimization of the variance in the identified parameters, which would in reality be derived from selected experimental runs. In the DoE method, equivalent simulations obviously replace the experimental runs.
Given an arbitrary model function with measurement points ω and a vector of n parameters in $\mathbb{R}^n$

$$f : \Omega \times \mathbb{R}^n \to \mathbb{R} \tag{C.26}$$

, the set $T_{\text{var}} := \{t_1, ..., t_m\} \subseteq \Omega$ is the potentially available set of all measurements. As a part of these, the subset $S \subseteq T_{\text{var}}$ contains the selected measurements only. The vector $(w_{\text{s}})_i$ denotes the location of these selected measurements with:

$$(w_{\text{s}})_i = \begin{cases} 1 & \text{if } t_{\text{i}} \in \text{S} \\ 0 & \text{else} \end{cases} \tag{C.27}$$

Optimal measurement points (and thus the definition of the subset S) are then selected by a minimization of the prediction error between 'true' and obtained model outputs. $F(p)$ are the model outputs of $f(t_i, p)$ for the set T_{var} and 'unknown' parameter vector p, while η are the functional values of a pre-defined true parameter set $\hat{p}$, which serves in this case as the non-existent actual experimental results. The deviation between 'true' outputs η and the $F(p)$, weighted by the expected output standard deviation with $\sum := diag\,(\sigma_1, ..., \sigma_m)$.

$$\min_{p \subseteq \mathbb{R}^n} \left\| \sum^{-1} (F(p) - \eta) \right\|_2^2 \tag{C.28}$$

The definition of 'true' parameter set can either be based on previous experimental findings or educated guesses, when no data exists. Apparently, an out-of-range choice of the 'true' parameters would influence the method's outcome. However, this guess is also an inevitable step to the mathematical process, when no previous knowledge on parameter magnitudes is available. The 'unknown' parameter vector p itself is identified at T_{var}. Given a linear approach for model $F(p)$

$$F(p) = Ap + b \tag{C.29}$$

, Equation C.28 becomes:

$$\min_{p \subseteq \mathbb{R}^n} \left\| \Sigma^{-1} \left(Ap + b - \eta \right) \right\|_2^2 \tag{C.30}$$

The resulting vector of parameters $p_{\mathrm{S}}^{\star}$ can then be understood as a realization of the normally distributed probability vector

$$P_{\mathrm{S}}^{\star} \sim N\left(\hat{p}, C_{\mathrm{S}}\right) \tag{C.31}$$

with covariance matrix

$$C_{\mathrm{S}} := \left(A^T \Sigma^{-1} W_{\mathrm{S}} \Sigma^{-1} A \right)^{-1} \tag{C.32}$$

around actual values equal to expectation value $\hat{p}$. In this notation, W_{S} is the diagonal matrix of weights w_{s}. The best accordance between expectation value $\hat{p}$ and obtained value $p_{\mathrm{S}}^{\star}$ would be reached with the smallest variance of $P_{\mathrm{S}}^{\star}$, i.e. the diagonal entries of matrix C_{S} being as small as possible. The normalized trace of matrix C_{S} is thus a common approach to quantify the quality criterion ϕ of the method and used in Sec. 5.2.1. The initial problem of minimizing experimental effort to obtain the best fitting parameters p is thus reduced to the following minimization problem:

$$\min_{w \subseteq \{0,1\}^{m_{\mathrm{var}}}} \phi\left(C(w)\right) \tag{C.33}$$

As the vector w is discrete between zero and one, the minimization problem can be solved by simply trying all possibilities, which sum up to 2^m. Clearly, this approach is not applicable with increasing length m of the vector. In this case, the discrete optimization problem is converted to a continuous one and solved accordingly with common solvers, setting an initial value for $p = p_0$, where optimization starts. Eventually, the continuous solution is re-transformed to the discrete states with heuristic methods, such as rounding. The method can be improved by a sequential approach, where the initial parameter is readjusted after each new measurement so that the influence of the initial guess p on the method is reduced. The same reduction of dependency on the initial boundary can also be reached by setting an additional limit to possible values for p, which is derived from already conducted method runs.

D. Artificial Neural Networks

Artificial Neural Networks (ANN) mimick the structure of a human brain in an abstract model. As human brains, ANN learn from experience, i.e. training data, by adapting their inherent parameters. ANN are used commonly used for pattern recognition in classification and clustering problems and for regression and statistical modeling of complex systems.

D.1. Neural Network Design

The ANN consists of multiple interconnected artificial neurons (Fig. D.1), holding information about the system. The artificial neuron itself is simplistic by nature, processing an input signal y_j from other nodes or neurons to an output signal y_k by weights w as a measure for each inputs significance and transfer or activation functions F with a threshold value Θ, which eventually defines the binary output of a neuron.

Mathematically, the input is processed by the weights:

$$s_\mathrm{u} = \sum_{j=a}^{b} \left(y_\mathrm{j} \cdot w_\mathrm{u,j}\right) + w_\mathrm{u,0} \tag{D.1}$$

, where $w_\mathrm{u,0}$ is called the bias, which allows the neuron to have an output in the case of zero input. The output is calculated by the transfer function:

$$y_\mathrm{u} = F\left(s_\mathrm{u}\right) \tag{D.2}$$

The inherent parameters weights and thresholds are adjusted during learning to minimize a defined error function for the problem.

D.1.1. Hidden Neurons

The design of neural networks can mainly be influenced by the number of neurons in the hidden layer, while the number of hidden layer is usually set to one for standard fitting problems [117]. According to Kruse et al. [132], the number of neurons should

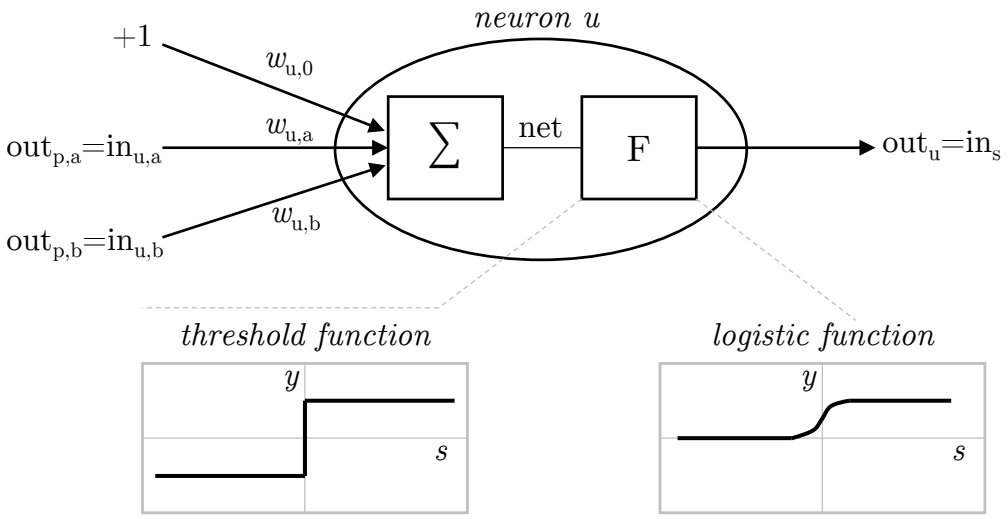

Figure D.1.: Schematic representation of an artificial neuron as in [117]

be high enough to cover all expected characteristics. However, exceeding this minimum necessary number increases the risk of overtraining. This behavior is comparable to a polynomial fit of a high order in the magnitude of grid points available, which would lead to a very accurate fit on the training data set, but also to an underestimation of the general trend in favor of modeling local deviations. Especially in neural network training with an unusually small number of data points, the choice of neurons is thus decisive for the success of the method.

D.2. Training Procedure

The progress of training can either be supervised, when known targets are present for training, or unsupervised, when underlying interrelationships in the data itself must be found. As ANN are used in this study for regression analysis, only the idea behind supervised learning will be described in the following. the goal of ANN supervised training is the minimization of the error e between its own predictions y_{ANN} and the targets o.

$$e = o - y \tag{D.3}$$

The adjustment of thresholds and weights in the neuron are then done according to the Delta-rule with learning rate η:

$$\begin{aligned} \Delta\Theta &= -\eta(o-y) \\ \Delta w_{\mathrm{u,j}} &= \eta(o-y)x_{\mathrm{u,j}} \end{aligned} \tag{D.4}$$

The Delta-rule thus simply shifts thresholds and weights in the direction of decreasing error: If the error is greater than zero, less neurons should be transmitted by the network. In this case, weights should decrease, while threshold are increased according to the Delta-rule (Eq. D.4) to reduce neuronal network output. For a simple case just a negotiation, where inputs are inverted, a graphical interpretation of the problem as in Kruse et al. [132] helps to understand the error minimization process by the Delta-rule. When extended to multilayer problems with input, hidden and output layer, this simple form of the delta rule fails to train ANNs, since the sequential route through different neuron layers cannot be considered.
Werbos [133] overcame this shortcoming by using differentiable transfer functions as for example the logistic function instead of simple jump functions with a threshold only and using a gradient-based description of the minimization process. With a differentiable formulation of the transfer function, the error function can be derivated with respect to the weights of a single neuron u: The total error is the sum of the error of each output neuron $v \in U_{\mathrm{out}}$

$$e = \sum_{v \in U_{\mathrm{out}}} e_{\mathrm{v}}. \tag{D.5}$$

Since the error only depends on the weights $\vec{w}_{\mathrm{u}}$ as a function of the input $\mathrm{net}_{\mathrm{u}} = \vec{w}_{\mathrm{u}} \cdot \vec{\mathrm{in}}_{\mathrm{u}}$, the gradient of the error yields:

$$\vec{\nabla}_{\vec{w}_{\mathrm{u}}} \cdot e = \frac{\partial e}{\partial \vec{w}_{\mathrm{u}}} = \frac{\partial e}{\delta \mathrm{net}_{\mathrm{u}}} \cdot \frac{\partial \mathrm{net}_{\mathrm{u}}}{\partial \vec{w}_{\mathrm{u}}} \tag{D.6}$$

With $\mathrm{net}_{\mathrm{u}} = \vec{w}_{\mathrm{u}} \cdot \mathrm{in}_{\mathrm{u}}$, the second factor yields:

$$\frac{\partial \mathrm{net}_{\mathrm{u}}}{\partial \vec{w}_{\mathrm{u}}} = \vec{\mathrm{in}}_{\mathrm{u}} \tag{D.7}$$

The first factor must consider the successor ('succ') neurons neurons $s = \mathrm{succ}(u)$ until the output layer v. With the definition of the total output error $e = \sum_{v \in U_{\mathrm{out}}} (o_{\mathrm{v}} - \mathrm{out}_{\mathrm{v}})^2$ the derivation can be expressed as

$$\frac{\partial e}{\partial \mathrm{net}_{\mathrm{u}}} = -2 \cdot \sum_{v \in U_{\mathrm{out}}} \sum_{s \in succ(u)} (o_{\mathrm{v}} - \mathrm{out}_{\mathrm{v}}) \frac{\partial \mathrm{out}_v}{\partial \mathrm{net}_{\mathrm{s}}} \cdot \frac{\partial \mathrm{net}_{\mathrm{s}}}{\partial \mathrm{net}_{\mathrm{u}}} = 2 \cdot \vartheta_{\mathrm{u}} \tag{D.8}$$

, where ϑ_{u} is chosen to abbreviate the term in the following. Rearrangements of the sums and the definition of net input as a function of the preceding p outputs from predecessor ('pred') neurons

$$\mathrm{net_s} = \vec{w}_\mathrm{s} \cdot \vec{\mathrm{in}}_\mathrm{s} = \left(\sum_{p \in \mathrm{pred(s)}} w_\mathrm{sp}\ \mathrm{out_p} \right) - \Theta_\mathrm{s} \tag{D.9}$$

yields a recursive calculation of ϑ_u:

$$\vartheta_\mathrm{u} = \left(\sum_{s \in \mathrm{succ(u)}} \vartheta_\mathrm{s}\ w_\mathrm{su} \right) \cdot \frac{\partial \mathrm{out_u}}{\partial \mathrm{net_u}} \tag{D.10}$$

A more detailed mathematical description of this backpropagation process can be found in Kruse et al. [132]. Accordingly to the above-described Delta-rule, weights are finally changed into the direction of decreasing errors for the backpropagation process:

$$\Delta \vec{w}_\mathrm{u} = -\frac{\eta}{2} \cdot \vec{\nabla}_{\vec{w}_\mathrm{u}} \cdot e = \eta \cdot \vartheta_\mathrm{u} \cdot \vec{\mathrm{in}}_\mathrm{u} \tag{D.11}$$

Bibliography

[1] OECD OCDE. *World Energy Outlook 2015*. OECD Publishing, 2015. ISBN 9789264243668.

[2] Christof Lechner and Jörg Seume, editors. *Stationäre Gasturbinen*. VDI-Buch. Springer, Berlin, 2. edition, 2010. ISBN 9783540927884.

[3] Felix Güthe, Jaan Hellat, and Peter Flohr. The Reheat Concept: The Proven Pathway to Ultralow Emissions and High Efficiency and Flexibility. *Journal of Engineering for Gas Turbines and Power*, (131), 2009. doi: 10.1115/1.2836613.

[4] Juergen Voss, Armin Staedtler, and Keramat Fakhari. Meeting the Middle East Energy Demand with Proven Gas Turbines. In *Power-Gen Middle East 2015*, October 4-6, 2015.

[5] Jacopo Bellelli. The Shale gas 'revolution' in the United States: Global implications, options for the EU.

[6] Shearman & Sterling LLP. The Duck Curve Revolution and Natural Gas. URL `http://www.shearman.com/en/newsinsights/publications/2016/05/energy-update-articles/the-duck-curve-revolution-and-natural-gas`.

[7] Rory Pasquariello. Bayonne Energy Center ready for expansion. *Hudson Reporter*, September 14, 2016. URL `http://www.hudsonreporter.com/view/full_story/27269618/article-Bayonne-Energy-Center-ready-for-expansion--Clearing-the-way-for-new-gas-turbines-?instance=latest_story`.

[8] I.G.C. Dryden. *The Efficient Use of Energy*. Elsevier Science, 2013. ISBN 9781483101576. URL `https://books.google.de/books?id=5N9bAwAAQBAJ`.

[9] V. Smil. *Natural Gas: Fuel for the 21st Century*. Wiley, 2015. ISBN 9781119012856. URL `https://books.google.de/books?id=WGQdCgAAQBAJ`.

[10] Rene Schleucher. Es läuft: Das neue Kraftwerk ist am Netz. *Westdeutsche Zeitung*, January 28, 2016. URL http://www.wz.de/lokales/duesseldorf/es-laeuft-das-neue-kraftwerk-ist-am-netz-1.2110370.

[11] Elias Tsoutsanis, Nader Meskin, Mohieddine Benammar, and Khashayar Khorasani. A dynamic prognosis scheme for flexible operation of gas turbines. *Applied Energy*, 164:686–701, 2016. ISSN 03062619. doi: 10.1016/j.apenergy.2015.11.104.

[12] P. Marx, M. Liebau, P. Curran, K. Hollinger, D. Therkorn, and C. Reyser. GT26 Operational experience under changing market condition V1.2. In *Power-Gen Europe 2014*.

[13] U.S. Environmental Protection Agency. Basic Information about NO2, . URL https://www.epa.gov/no2-pollution/basic-information-about-no2.

[14] U.S. Environmental Protection Agency. Ozone Basics, . URL https://www.epa.gov/ozone-pollution/ozone-basics.

[15] The National Institute for Occupational Safety and Health. NIOSH Pocket Guide to Chemical Hazards: Carbon Monoxide. URL https://www.cdc.gov/niosh/npg/npgd0105.html.

[16] Stanley T. Omaye. Metabolic modulation of carbon monoxide toxicity. *Toxicology*, 180(2):139–150, 2002.

[17] The World Bank. *World development indicators 2017*. Oxford University Press, USA, 2017.

[18] Bundesministerium für Justiz und Verbraucherschutz. Thirteenth Ordinance for implementing the German Federal Emission Control Act for large-scale combustion plants, gas turbines and combustion engine systems / Dreizehnte Verordnung zur Durchführung des Bundes-Immissionsschutzgesetzes (Verordnung über Großfeuerungs-, Gasturbinen- und Verbrennungsmotoranlagen - 13. BImSchV).

[19] European Union. Directive 2010/75/EU of the European Parliament and of the Council of 24th November 2010 on industrial emissions (integrated pollution prevention and control), 2010.

[20] European Union. Commission Implementing Decision (EU) 2017/302 of 15 February 2017 establishing best available techniques (BAT) conclusions, under Directive 2010/75/EU of the European Parliament and of the Council, for the intensive rearing of poultry or pigs (notified under document C(2017) 688) (Text with EEA relevance.). *Official Journal of the European Union*.

[21] Ministry of Environmental Protection. Emission Standard of Air Pollutants for Thermal Power Plants. URL http://www.zhb.gov.cn/gkml/hbb/qt/201109/t20110921_217526.htm.

[22] Environmental Protection Agency. Chapter I - Subchapter C - Part 60 - Subpart KKKK - Standards of Performance for Stationary Combustion Turbines. URL https://www.ecfr.gov/cgi-bin/text-idx?node=sp40.7.60.kkkk#se40.8.60_14320.

[23] Yolo-Solano Air Quality Management District. Rule 2.34, Stationary Gas Turbines.

[24] Arthur H. Lefebvre and Dilip R. Ballal. *Gas turbine combustion: Alternative fuels and emissions*. Taylor & Francis, Boca Raton, 3rd ed. edition, 2010. ISBN 9781420086041. URL http://site.ebrary.com/lib/academiccompletetitles/home.action.

[25] Tim C. Lieuwen and Vigor Yang. *Gas Turbine Emissions*. Cambridge University Press, Cambridge, 2013. ISBN 9781139015462. doi: 10.1017/CBO9781139015462.

[26] European Union. European Union (Large Combustion Plants) Regulations 2012, 2012.

[27] European Union. Directive 2015/2193/EU of the European Parliament and of the Council of 25th November 2015 on the limitation of emissions of certain pollutants into the air from medium combustion plants, 2015.

[28] Felix Güthe, Martin Gassner, Stefano Bernero, Thiemo Meeuwissen, and Torsten Wind. Chemical Kinetic Models for Enhancing Gas Turbine Flexibility: Model Validation and Application. In *ASME Turbo Expo 2016: Turbomachinery Technical Conference and Exposition*, page V04BT04A004, Monday 13 June 2016. doi: 10.1115/GT2016-57223.

[29] Allan J. Volponi. Gas turbine engine health management: Past, present, and future trends. *Journal of Engineering for Gas Turbines and Power*, 136(5): 051201, 2014.

[30] International Organization for Standardization. Asset management - Overview, principles and terminology (ISO 55000:2014), May 2017.

[31] Dan Miklovic. What is Asset Performance Management?, 2015. URL http://blog.lnsresearch.com/what-is-asset-performance-management.

[32] T. Álvarez Tejedor, R. Singh, and P. Pilidis. Advanced gas turbine asset and performance management. In *Modern Gas Turbine Systems*, pages 515–564. Elsevier, 2013. ISBN 9781845697280. doi: 10.1533/9780857096067.3.515.

[33] Accenture. 2016 Upstream Oil and Gas Digital Trends Survey, 2016. URL https://www.slideshare.net/accenture/the-accenture-and-microsoft-2016-upstream-oil-and-gas-digital-trends-survey.aspx.

[34] Binu Mathew. How Big Data is reducing costs and improving performance in the upstream industry. *World Oil*, 2016.

[35] BMT Smart. Fleet Performance Management should be saving (not costing) you money. URL https://www.bmtsmart.com/media/6111234/MA8622_BMT-SMART_ebook_FA.PDF.

[36] Peter Mantel. Is Fleet Performance Management saving or costing you money?, 2017. URL https://www.safety4sea.com/is-fleet-performance-management-saving-or-costing-your-money/.

[37] Michael Bailey. Qantas tech deal with GE tipped to save millions in fuel bills with smart app, 2016. URL http://www.afr.com/technology/apps/business/qantas-tech-deal-with-ge-tipped-to-save-millions-in-fuel-bills-with-smart-app-20161006-grw5kv.

[38] Mark Egan. How Big Data and the Industrial Internet Can Help Southwest Save $100 Million on Fuel, 2015. URL http://www.ge.com/reports/big-data-industrial-internet-can-help-southwest-save-100-million-fuel/.

[39] Naresh Sundaram Iyer. Systems and methods for provisioning a fleet of industrial assets as a computing-cloud, 2015. URL https://www.google.com/patents/US20150371190.

[40] J. L. Coullon and S. Wan. ASSET PERFORMANCE MANAGEMENT THE DIGITAL JOURNEY.

[41] General Electric Company. Predix Architecture and Services. URL https://www.predix.io/.

[42] Siemens and General Electric gear up for the internet of things. *The Economist*, 2016, 3.12.2016.

[43] Tim Miser. Ones & Zeros: How Digital Power Plants Are Leveraging Big Data and Analytics for Greater Reliability and Profit. *Power Engineering*, 2016.

[44] Akshay Patwal and Timot Veer. Digitalization: Redefining Power Generation Services - Power Engineering. *Power Engineering*, 23.8.2016.

[45] Accenture. Digital Transformation of Industries: Electricity Industry, 2016. URL https://www.accenture.com/t20170116T084450__w__/us-en/_acnmedia/Accenture/Conversion-Assets/WEF/PDF/Accenture-Electricity-Industry.pdf.

[46] Mohammadreza Tahan, Elias Tsoutsanis, Masdi Muhammad, and Z. A. Abdul Karim. Performance-based health monitoring, diagnostics and prognostics for condition-based maintenance of gas turbines: A review. *Applied Energy*, 198: 122–144, 2017. ISSN 03062619. doi: 10.1016/j.apenergy.2017.04.048.

[47] International Organization for Standardization. Gas turbines - procurement - Part 9: Reliability, availability, maintainability and safety, December 1999.

[48] GE Power. GT24/GT26 MXL2 TURBINE UPGRADE. URL https://www.gepower.com/services/gas-turbines/upgrades/gt24-gt26-mxl2.

[49] J. P. Immarigeon, W. Beres, P. Au, A. Fahr, and W. Wallace. Life cycle management strategies for aging engines, 2003.

[50] Cyrus B. Meher-Homji, M. Chaker, and H. Motiwalla. Gas turbine performance deterioration. In *Proceedings of the 30th Turbomachinery Symposium*, pages 17–20, 2001.

[51] S. Can Gulen, Patrick R. Griffin, and Sal Paolucci. Real-time on-line performance diagnostics of heavy-duty industrial gas turbines. In *ASME Turbo Expo 2000: Power for Land, Sea, and Air*, 2000.

[52] Ernst Schneider, Saba Demircioglu, Susana Franco, and Dirk Therkorn. Analysis of Compressor On-Line Washing to Optimize Gas Turbine Power Plant Performance. In *ASME Turbo Expo 2009: Power for Land, Sea, and Air*, pages 591–599, 2009. doi: 10.1115/GT2009-59356.

[53] Dirk Therkorn. Remote Monitoring and Diagnostic for Combined-Cycle Power Plants. In *ASME Turbo Expo 2005: Power for Land, Sea and Air*, 2005.

[54] O. A. Guo. Active turbine tip clearance control research. In *The 5th NASA GRC Propulsion Control and Diagnostics Workshop, Cleveland, Ohio, USA*, 2015.

[55] Y. G. Li and P. Nilkitsaranont. Gas turbine performance prognostic for condition-based maintenance. *Applied Energy*, 86(10):2152–2161, 2009. ISSN 03062619. doi: 10.1016/j.apenergy.2009.02.011.

[56] Christian Rudolf, Manfred Wirsum, Martin Gassner, Benjamin T. Zoller, and Stefano Bernero. Modelling of Gas Turbine NOx Emissions Based on Long-Term Operation Data. In *ASME Turbo Expo 2016: Turbomachinery Technical Conference and Exposition*, page V04BT04A006, Monday 13 June 2016. doi: 10.1115/GT2016-57252.

[57] Mohammed S. Syed, Kerry M. Dooley, Frantisek Madron, and F. Carl Knopf. Enhanced turbine monitoring using emissions measurements and data reconciliation. *Applied Energy*, 173:355–365, 2016. ISSN 03062619. doi: 10.1016/j.apenergy.2016.04.059.

[58] A. Andreini and B. Facchini. Gas Turbines Design and Off-Design Performance Analysis With Emissions Evaluation. *Journal of Engineering for Gas Turbines and Power*, 126(1):83, 2004. doi: 10.1115/1.1619427.

[59] T. Held, M. Mueller, S. Li, and H. Mongia. A data-driven model for NO(x), CO and UHC emissions for a dry low emissions gas turbine combustor. In *37th Joint Propulsion Conference and Exhibit*, 08 July 2001 - 11 July 2001. doi: 10.2514/6.2001-3425.

[60] N. Klarmann, B. Zoller, and T. Sattelmayer. Numerical Modeling of CO-Emissions for Gas Turbine Combustors Operating at Part-Load Conditions. In *Proceedings of Global Power and Propulsion Forum Shanghai*, pages 1–8, Shanghai, China, 2017.

[61] F. Xu, V. Nori, and J. Basani. CO Prediction for Aircraft Gas Turbine Combustors. In *ASME Turbo Expo 2013: Turbine Technical Conference and Exposition*, page V01AT04A013, 2013. doi: 10.1115/GT2013-94282.

[62] Douglas L. Allaire, Ian A. Waitz, and Karen E. Willcox. A Comparison of Two Methods for Predicting Emissions From Aircraft Gas Turbine Combustors. In *ASME Turbo Expo 2007: Power for Land, Sea, and Air*, pages 899–908, May 14–17, 2007. doi: 10.1115/GT2007-28346.

[63] P. Gokulakrishnan, C. C. Fuller, R. G. Joklik, and M. S. Klassen. Chemical Kinetic Modeling of Ignition and Emissions From Natural Gas and LNG Fueled Gas Turbines. In *ASME Turbo Expo 2012: Turbine Technical Conference and Exposition*, page 1383, Monday 11 June 2012. doi: 10.1115/GT2012-69902.

[64] Enis T. Turgut. Effects of Ambient Air Temperature on Gaseous Emissions of Turbofan Engines. *Journal of Propulsion and Power*, 32(3):713–725, 2016. doi: 10.2514/1.B35916.

[65] W. S.Y. Hung. Carbon monoxide emissions from gas turbines as influenced by ambient temperature and turbine load. *Journal of Engineering for Gas Turbines and Power*, 115(3):588–593, 1993.

[66] Warren G. Lamont, Mario Roa, and Robert P. Lucht. Application of Artificial Neural Networks for the Prediction of Pollutant Emissions and Outlet Temperature in a Fuel-Staged Gas Turbine Combustion Rig. In *ASME Turbo Expo 2014: Turbine Technical Conference and Exposition*, page V04AT04A002, Monday 16 June 2014. doi: 10.1115/GT2014-25030.

[67] Allen M. Danis, Byron A. Pritchard, and Hukam C. Mongia. Empirical and semi-empirical correlation of emissions data from modern turbopropulsion gas turbine engines. In *ASME 1996 International Gas Turbine and Aeroengine Congress and Exhibition*, pages V003T06A016–V003T06A016, 1996.

[68] Francis Bainier, Pascal Alas, Florian Morin, and Tony Pillay. Two Years of Improvement and Experience in PEMS for Gas Turbines. In *ASME Turbo Expo 2016: Turbomachinery Technical Conference and Exposition*, page V009T24A005, Monday 13 June 2016. doi: 10.1115/GT2016-56138.

[69] Brian Swanson. A Cost Effective Advanced Emissions Monitoring Solution for Gas Turbines: Statistical Hybrid Predictive System That Accurately Measures

Nitrogen Oxides, Carbon Monoxide, Sulfur Dioxide, Hydrocarbon and Carbon Dioxide Mass Emission Rates. In *ASME Turbo Expo 2008: Power for Land, Sea, and Air*, pages 267–276, June 9–13, 2008. doi: 10.1115/GT2008-50401.

[70] Eugene Simon, Jessica Palmer, and Brian Swanson. Type Models Implemented as Statistical Hybrid Emission Monitors for like-kind Gas Turbines. In *25th annual CEM EPRI Utility Continouous Emissions Monitoring User Group Meeting*, 2016.

[71] Stephen P. Lukachko and Ian A. Waitz. Effects of engine aging on aircraft NOx emissions. In *ASME International Gas Turbine & Aeroengine Congress & Exhibition*, 1997.

[72] L. E. Bakken and L. Skogly. Parametric Modeling of Exhaust Gas Emission From Natural Gas Fired Gas Turbines. *Journal of Engineering for Gas Turbines and Power*, 118(3):553, 1996. doi: 10.1115/1.2816683.

[73] Thomas Palmé, Francois Liard, and Dan Cameron. Hybrid Modeling of Heavy Duty Gas Turbines for On-Line Performance Monitoring. In *ASME Turbo Expo 2014: Turbine Technical Conference and Exposition*, page V006T06A011, 2014. doi: 10.1115/GT2014-26015.

[74] Christian Rudolf, Manfred Wirsum, Martin Gassner, and Stefano Bernero. Analysis of Long-Term Gas Turbine Operation With a Model-Based Data Reconciliation Technique. In *ASME Turbo Expo 2015: Turbine Technical Conference and Exposition*, page V006T05A008, 2015. doi: 10.1115/GT2015-42497.

[75] Dirk Therkorn, Martin Gassner, Vincent Lonneux, Mengbin Zhang, and Stefano Bernero. CCPP Operational Flexibility Extension Below 30% Load Using Reheat Burner Switch-Off Concept. In *ASME Turbo Expo 2015: Turbine Technical Conference and Exposition*, page V003T20A007, 2015. doi: 10.1115/GT2015-42446.

[76] Moritz Lipperheide, Frank Weidner, Manfred Wirsum, Martin Gassner, and Stefano Bernero. Long-Term NOx Emission Behavior of Heavy Duty Gas Turbines: An Approach for Model-Based Monitoring and Diagnostics. In *Volume 6: Ceramics; Controls, Diagnostics and Instrumentation; Education; Manufacturing Materials and Metallurgy*, page V006T05A001. ASME, 2017. ISBN 978-0-7918-5091-6. doi: 10.1115/GT2017-63181.

[77] Moritz Lipperheide, Frank Weidner, Manfred Wirsum, Martin Gassner, and Stefano Bernero. Langzeitanalyse von Emissionen und Brennkammerpulsationen zur Betriebsüberwachung und -Optimierung. In *Tagungsband*. Wissenschaftliche Koordinierungsstelle AG Turbo, 2016.

[78] Moritz Lipperheide, Frank Stephan Weidner, Manfred Christian Wirsum, Martin Gassner, and Stefano Bernero. Gasturbine 4.0. *GWF / Gas, Erdgas*, 2017(9): 52–57, 2017. ISSN 0016-4909. URL http://publications.rwth-aachen.de/record/699416.

[79] Moritz Lipperheide, Frank Weidner, Manfred Wirsum, Martin Gassner, and Stefano Bernero. Alterungsinduzierte Emissionsprogression in Hochleistungsgasturbinen (Typ GT24/GT26). In Michael Beckmann and Antonio Hurtado, editors, *Kraftwerkstechnik 2017*, Kraftwerkstechnik. SAXONIA, Freiberg, Sachs, 2017. ISBN 9783934409798.

[80] Moritz Lipperheide, Frank Weidner, Manfred Wirsum, Martin Gassner, and Stefano Bernero. Long-term NOx Emission Behavior of Heavy Duty Gas Turbines: An Approach For Model-based Monitoring and Diagnostics. *Journal of Engineering for Gas Turbines and Power*, 2018. doi: 10.1115/1.4040009.

[81] Moritz Lipperheide, Frank Stephan Weidner, Martin Gassner, Stefano Bernero, and Manfred Christian Wirsum. Impact of Gas Turbine Cyclic Operation on Engine Aging - An Investigation of the GT24/GT26 Fleet. In *[Global Power and Propulsion Forum, GPPF, 2018-01-10 - 2018-01-12, Zurich, Switzerland]*, pages GPPS–2018–0031, 1–5, 2018. doi: 10.18154/RWTH-2018-00539. URL http://publications.rwth-aachen.de/record/712525RWTH.

[82] Moritz Lipperheide, Martin Gassner, Frank Weidner, Stefano Bernero, and Manfred Wirsum. Long-term carbon monoxide emission behavior of heavy-duty gas turbines: An approach for model-based monitoring and diagnostics. *International Journal of Spray and Combustion Dynamics*, page 1756827718791921, 2018. doi: 10.1177/1756827718791921. URL https://doi.org/10.1177/1756827718791921.

[83] Moritz Lipperheide, Thomas Bexten, Manfred Wirsum, Martin Gassner, and Stefano Bernero. A Comparative Study of Data and Physically Based Gas Turbine Modeling for Long-Term Monitoring Scenarios: Part II — Emission Prediction Utilizing Different Levels of Design Information. In *Volume 6:*

Ceramics; Controls, Diagnostics, and Instrumentation; Education; Manufacturing Materials and Metallurgy, page V006T05A024. ASME, 2018. ISBN 978-0-7918-5112-8. doi: 10.1115/GT2018-76650.

[84] K. D. Döbbeling, E. P. Gutmark, C.O.D. Paschereit, and W. Weisenstein. Brenner, 2000. URL `https://encrypted.google.com/patents/EP1002992A1?cl=ja`.

[85] Martin Zajadatz, Rudolf Lachner, Stefano Bernero, Christian Motz, and Peter Flohr. Development and Design of Alstom's Staged Fuel Gas Injection EV Burner for NOx Reduction. In *ASME Turbo Expo 2007: Power for Land, Sea, and Air*, pages 559–567, 2007. doi: 10.1115/GT2007-27730.

[86] Klaus Döbbeling, Jaan Hellat, and Hans Koch. 25 Years of BBC/ABB/Alstom Lean Premix Combustion Technologies. pages 201–213. doi: 10.1115/GT2005-68269.

[87] Adnan Eroglu, Peter Flohr, Philipp Brunner, and Jaan Hellat. Combustor Design for Low Emissions and Long Lifetime Requirements. In *ASME Turbo Expo 2009: Power for Land, Sea, and Air*, pages 435–444, 2009. doi: 10.1115/GT2009-59540.

[88] M. N. Poyyapakkam, A. Eroglu, R. Carroni, G. J. Kelsall, and J. X. Chen. Methods of reducing emissions for a sequential combustion gas turbine and combustor for a gas turbine, 2010. URL `https://www.google.com/patents/US20100077720`.

[89] A. Ciani, A. Eroglu, F. Güthe, and B. Paikert. Full-Scale Atmospheric Tests of Sequential Combustion. In *ASME Turbo Expo 2010: Power for Land, Sea, and Air*, pages 759–768, 2010. doi: 10.1115/GT2010-22891.

[90] International Organization for Standardization. Condition monitoring and diagnostics of machines - General guidelines, June 2017.

[91] J. Warnatz, U. Maas, and R. W. Dibble. *Combustion: Physical and Chemical Fundamentals, Modelling and Simulation, Experiments, Pollutant Formation.* Springer, 2001. ISBN 9783540677512. URL `https://books.google.de/books?id=hldApAvyZf4C`.

[92] Irvin Glassman and Richard A. Yetter. Combustion, Fourth Edition.

[93] C. P. Fenimore. Formation of nitric oxide in premixed hydrocarbon flames. In *Symposium (International) on Combustion*, volume 13, pages 373–380, 1971.

[94] Joseph W. Bozzelli and Anthony M. Dean. O+ NNH: A possible new route for NOx formation in flames. *International Journal of Chemical Kinetics*, 27(11): 1097–1109, 1995.

[95] A. A. Konnov, G. Colson, and J. de Ruyck. The new route forming NO via NNH. *Combustion and Flame*, 121(3):548–550, 2000. ISSN 00102180.

[96] Andrés Colorado and Vincent McDonell. Reactor Network Analysis to Assess Fuel Composition Effects on NOx Emissions From a Recuperated Gas Turbine. In *Volume 4B: Combustion, Fuels and Emissions*, page V04BT04A030. ASME, 2014. ISBN 978-0-7918-4569-1. doi: 10.1115/GT2014-26361.

[97] Sebastian Göke. *Ultra wet combustion*. PhD thesis, Technische Universität Berlin, 2012.

[98] Fernando Biagioli and Felix Güthe. Effect of pressure and fuel–air unmixedness on NOx emissions from industrial gas turbine burners. *Combustion and Flame*, 151(1-2):274–288, 2007. ISSN 00102180. doi: 10.1016/j.combustflame.2007.04.007.

[99] W. C. Gardiner. *Gas-Phase Combustion Chemistry*. Springer New York, New York, NY, 2000. ISBN 978-1-4612-7088-1. doi: 10.1007/978-1-4612-1310-9.

[100] Sanjay M. Correa. A Review of NOx Formation Under Gas-Turbine Combustion Conditions. *Combustion Science and Technology*, 87(1-6):329–362, 1993. ISSN 0010-2202. doi: 10.1080/00102209208947221.

[101] Craig T. Bowman. Kinetics of pollutant formation and destruction in combustion. *Progress in energy and combustion science*, 1(1):33–45, 1975.

[102] A. A. Westenberg. Kinetics of NO and CO in Lean, Premixed Hydrocarbon-Air Flames. *Combustion Science and Technology*, 4(1):59–64, 1971. ISSN 0010-2202. doi: 10.1080/00102207108952472.

[103] Stephen R. Turns et al. *An introduction to combustion*, volume 287. McGraw-hill New York, 1996.

[104] Irvin Glassman, Richard A. Yetter, and Nick G. Glumac. *Combustion*. Academic press, 2014.

[105] C. S. Connors, J. C. Barnes, and A. M. Mellor. Semiempirical predictions and correlations of CO emissions from utility combustion turbines. *Journal of Propulsion and Power*, 12(5):926–932, 1996. doi: 10.2514/3.24124.

[106] Wayne K. Metcalfe, Sinéad M. Burke, Syed S. Ahmed, and Henry J. Curran. A hierarchical and comparative kinetic modeling study of C1- C2 hydrocarbon and oxygenated fuels. *International Journal of Chemical Kinetics*, 45(10):638–675, 2013.

[107] Emile Webster. Drift in type k bare-wire thermocouples from different manufacturers. *International Journal of Thermophysics*, 38, 05 2017. doi: 10.1007/s10765-017-2210-1.

[108] Hans-Georg Münzberg and Joachim T. Kurzke. *Gasturbinen: Betriebsverhalten u. Optimierung*. Hochschultext. Springer, Berlin, 1977. ISBN 3540080325.

[109] Ebi A. Ogiriki, Yiguang G. Li, Theoklis Nikolaidis, ThankGod E. Isaiah, and Gowon Sule. Effect of Fouling, Thermal Barrier Coating Degradation and Film Cooling Holes Blockage on Gas Turbine Engine Creep Life. *Procedia CIRP*, 38: 228–233, 2015. ISSN 22128271. doi: 10.1016/j.procir.2015.07.017.

[110] Rainer Kurz, Klaus Brun, and Meron Wollie. Degradation Effects on Industrial Gas Turbines. *Journal of Engineering for Gas Turbines and Power*, 131(6): 062401, 2009. doi: 10.1115/1.3097135.

[111] Rainer Kurz and Klaus Brun. Degradation in Gas Turbine Systems. In *ASME Turbo Expo 2000: Power for Land, Sea, and Air*, page V002T03A003, 2000. doi: 10.1115/2000-GT-0345.

[112] Norbert Wiener. The homogeneous chaos. *American Journal of Mathematics*, 60 (4):897–936, 1938.

[113] Stefano Marelli and Bruno Sudret. UQLab User Manual– Polynomial Chaos Expansions.

[114] Stefano Marelli, Carlos Lamas, and Bruno Sudret. UQLab User Manual - Sensitivity analysis.

[115] Emerson Process Management. Rousemount 3051 Pressure Transmitter, Catalog 2008-2009.

[116] Vaisala. Vaisala Combined Pressure, Humidity and Temperature Transmitter PTU300, 2008.

[117] Magnus Fast. *Artificial neural networks for gas turbine monitoring.* Doctoral Thesis, Division of Thermal Power Engineering, Department of Energy Sciences, Faculty of Engineering, Lund University.

[118] M. Fast, M. Assadi, and S. De. Development and multi-utility of an ANN model for an industrial gas turbine. *Applied Energy*, 86(1):9–17, 2009. ISSN 03062619. doi: 10.1016/j.apenergy.2008.03.018.

[119] M. Fast and T. Palmé. Application of artificial neural networks to the condition monitoring and diagnosis of a combined heat and power plant. *Energy*, 35(2): 1114–1120, 2010. ISSN 03605442. doi: 10.1016/j.energy.2009.06.005.

[120] Mohsen Assadi Magnus Fast and Sudipta De. Condition Based Maintenance of Gas Turbines Using Simulation Data and Artificial Neural Network: A Demonstration of Feasibility.

[121] Thomas Palmé, Peter Breuhaus, Mohsen Assadi, Albert Klein, and Minkyo Kim. New Alstom Monitoring Tools Leveraging Artificial Neural Network Technologies. In *ASME Turbo Expo 2011: Turbine Technical Conference and Exposition*, pages 281–292, 2011. doi: 10.1115/GT2011-45990.

[122] Thomas Palmé, Magnus Fast, and Marcus Thern. Gas turbine sensor validation through classification with artificial neural networks. *Applied Energy*, 88(11): 3898–3904, 2011. ISSN 03062619. doi: 10.1016/j.apenergy.2011.03.047.

[123] Magnus Fast, Thomas Palme, and Magnus Genrup. A Novel Approach for Gas Turbine Condition Monitoring Combining CUSUM Technique and Artificial Neural Network. In *Volume 1: Aircraft Engine; Ceramics; Coal, Biomass and Alternative Fuels; Controls, Diagnostics and Instrumentation; Education; Electric Power; Awards and Honors*, pages 567–574. ASME, 2009. ISBN 978-0-7918-4882-1. doi: 10.1115/GT2009-59402.

[124] Neural Network Toolbox, 2015. URL `https://de.mathworks.com/help/nnet/`.

[125] W. Chine, A. Mellit, V. Lughi, A. Malek, G. Sulligoi, and A. Massi Pavan. A novel fault diagnosis technique for photovoltaic systems based on artificial neural networks. *Renewable Energy*, 90:501–512, 2016. ISSN 09601481. doi: 10.1016/j.renene.2016.01.036.

[126] Fangming Ye, Zhaobo Zhang, K. Chakrabarty, and Xinli Gu. Board-Level Functional Fault Diagnosis Using Artificial Neural Networks, Support-Vector Machines, and Weighted-Majority Voting. *IEEE Transactions on Computer-Aided Design of Integrated Circuits and Systems*, 32(5):723–736, 2013. ISSN 0278-0070. doi: 10.1109/TCAD.2012.2234827.

[127] Krzysztof Patan. *Artificial Neural Networks for the Modelling and Fault Diagnosis of Technical Processes*, volume 377 of *Lecture Notes in Control and Information Sciences*. Springer Berlin Heidelberg, Berlin, Heidelberg, 2008. ISBN 978-3-540-79871-2. doi: 10.1007/978-3-540-79872-9.

[128] Joscha Reimer. Die Experimental Design Toolbox zur optimalen Versuchsplanung.

[129] Vaisala. Humidity Conversion Formulas: Calculation formular for humidity, 2013.

[130] Gregory P. Smith, David M. Golden, Michael Frenklach, Nigel W. Moriarty, Boris Eiteneer, Mikhail Goldenberg, C. Thomas Bowman, Ronald K. Hanson, Soonho Song, William C. Gardiner, Jr., Vitali V. Lissianski, Zhiwei Qin. GRI-MECH 3.0. URL `http://www.me.berkeley.edu/gri_mech/`.

[131] G. P. Smith, Y. Tao, H. Wang. Foundational Fuel Chemistry Model Version 1.0 (FFCM-1), 2016. URL `http://nanoenergy.stanford.edu/ffcm1`.

[132] Rudolf J. Kruse, Christian Borgelt, Frank Klawonn, Christian Moewes, Georg Ruß, and Matthias Steinbrecher. *Computational Intelligence: Eine methodische Einführung in Künstliche Neuronale Netze, Evolutionäre Algorithmen, Fuzzy-Systeme und Bayes-Netze*. Studium. Vieweg + Teubner, Wiesbaden, 2012. ISBN 978-3-8348-8299-8. doi: 10.1007/978-3-8348-8299-8. URL `http://dx.doi.org/10.1007/978-3-8348-8299-8`.

[133] Paul John Werbos. Beyond regression: New tools for prediction and analysis in the behavioral sciences. *Doctoral Dissertation, Applied Mathematics, Harvard University, MA*, 1974.

Index